Tuning in to the feedback bassline: revealing the operation of AGNs in galaxy clusters with high-resolution radio observations

Timmerman, R.

Tuning in to the Feedback Bassline

Revealing the operation of AGNs in galaxy clusters with high-resolution radio observations

Proefschrift

ter verkrijging van
de graad van doctor aan de Universiteit Leiden,
op gezag van rector magnificus prof.dr.ir. H. Bijl,
volgens besluit van het college voor promoties
te verdedigen op woensdag 22 november 2023
klokke 12:30 uur
door

Roland Timmerman

geboren te Meppel, Nederland
in 1996

Promotor:	Prof. dr. H. J. A. Röttgering
Co-promotor	Dr. R. J. van Weeren

Promotiecommissie:

Prof. dr. I. A. G. Snellen	
Prof. dr. K. H. Kuijken	
Prof. dr. A. C. Edge	(Durham University)
Prof. dr. B. R. McNamara	(University of Waterloo)
Dr. L. K. Morabito	(Durham University)
Dr. A. Simionescu	(SRON, Leiden)

ISBN: 978-94-6419-963-5

The front cover is an illustration of the radio galaxy Hercules A based on the LOFAR-VLBI map included in this thesis (Chapter 3). In addition, a black hole's accretion disk is displayed in the center of the image. The rear cover shows the layout of the LOw Frequency ARray, a key instrument in this thesis.

Front cover illustrated by Rick Bex
Rear cover illustrated by the author

Contents

1

Introduction

Immediately following the Big Bang, matter in the Universe was distributed very uniformly. However, gravitational interaction caused minor overdensities that slowly attract surrounding matter to further increase in density. For the first 380,000 years, the baryonic matter in the Universe was in an ionized state due to its high temperature. This caused matter to be tightly coupled to photons, which counteract the gravitational clustering of matter. Only dark matter, which does not couple to photons, was able to immediately initiate gravitational collapse. As the Universe expanded and cooled down, baryonic matter started to recombine into neutral atoms, causing it to decouple from photons. An imprint of the density of baryonic matter at this time remains visible as the Cosmic Microwave Background (CMB, Planck Collaboration 2020). As matter gravitationally collapses, it forms denser "walls" of matter encompassing large voids in the Universe. Where these walls meet, they in turn collapse into narrow filaments. Finally, at the intersections of filaments, we see the formation of very dense nodes. This distribution of matter in the Universe is referred to as the "Cosmic Web". Within the Cosmic Web, the first stars and galaxies were able to form. At the nodes of the Cosmic Web, these galaxies grouped together to form large clusters of galaxies (see Figure 1.1), which are the most massive gravitationally bound structures in the Universe with masses on the order of $10^{14} - 10^{15}$ solar masses (e.g., Peebles & Yu 1970; Press & Schechter 1974).

Galaxies and galaxy clusters are one of the main topics of current astronomical research. These objects undergo major changes from their initial formation to the present day, experience strong interactions with other galaxies and galaxy clusters, and feature complex interactions between their different components. This leaves major questions as to how exactly these objects form and evolve throughout cosmic time.

1.1 Galaxy clusters

The galaxy clusters we observe today have formed hierarchically through the mergers of smaller galaxy clusters to create more massive galaxy clusters. Merger events are some of the most energetic events in the Universe (e.g., Markevitch et al. 1999),

Figure 1.1: The galaxy cluster eMACS J1823.1+7822 as captured by the Hubble Space Telescope. Image credit: ESA/Hubble & NASA, H. Ebeling

and have considerable impact on the individual components of the galaxy cluster. As such, we typically classify galaxy clusters based on their dynamical state: relaxed clusters and recent mergers.

Unlike what their name suggests, galaxies comprise only about 10% of the total baryonic mass in galaxy clusters (e.g. Chiu et al. 2018). The vast majority of the mass is part of the extremely hot ionized gas known as the intracluster medium (ICM). Due to its temperature of around 10^{7-8} K, the ICM produces strong thermal bremsstrahlung, which is observed as bright radiation in the X-ray regime (e.g., Gursky et al. 1971; Forman et al. 1972), as shown in Figure 1.2. The emission of this radiation comes at the cost of the internal energy of the ICM, resulting in a cooling effect. As the ICM cools down in its central regions, where the cooling effect is the strongest, it is drawn to the center of the cluster by gravity. There, it compresses in order to retain the internal pressure required to support its own weight. This in practice means that the emission of X-ray radiation causes the ICM to sink down the gravitational well in what is known as a *cooling flow* (e.g., Fabian 1994). At the core of the cluster, we commonly find a massive central galaxy which dominates the local region and can be easily identified as it is often the brightest cluster galaxy (BCG). When the cooling flow reaches the center of the cluster, it accretes onto the BCG. In this central galaxy, the cooled ICM gives rise to star-formation and fuels the supermassive black hole (SMBH) located in the core of the galaxy.

Although being a physically sound model, a number of observations indicate that the previously described cooling process does not actually take place as described. First of all, by comparing the X-ray brightness of the ICM with the internal energy of this medium, one can predict how long it takes for the ICM to fully cool down. For relaxed clusters, this is typically less than the Hubble time within approximately 100 kpc, and further decreases to less than a Gyr within approximately 10 kpc (Voigt & Fabian 2004). Based on this estimate, the ICM is expected to cool down on such short time scales that it should no longer remain present in modern-day galaxy clusters.

Additionally, the X-ray luminosity of a typical galaxy cluster suggests that the cooling flow should deposit up to 1000 $M_\odot$ of ICM per year onto the central BCG (e.g., Edge et al. 1992). However, the high star-formation rates which would be enabled by such a cooling flow are in general not observed (e.g., Fabian et al. 1982; McNamara & O'Connell 1989; Kaastra et al. 2001; Peterson et al. 2003; Peterson & Fabian 2006). This further suggests that the predicted cooling flows are prevented by a process which compensates for the ICM's radiative cooling.

We now understand that the SMBH in the central BCG plays a key role in the galaxy cluster. As the SMBH is fed by the surrounding cold gas, part of the energy involved in this process is released back into the environment, resulting in a strong feedback process. This feedback re-energizes the ICM, thereby preventing the ICM from rapidly cooling down and forming stars (e.g., McNamara & Nulsen 2007; Fabian 2012; Gitti et al. 2012a).

In addition to their galactic overdensity and the bright X-ray emission produced by their ICM, galaxy clusters can be recognized through the interaction of their hot ICM with the CMB, known as the Sunyaev-Zel'dovich (SZ, Sunyaev & Zeldovich

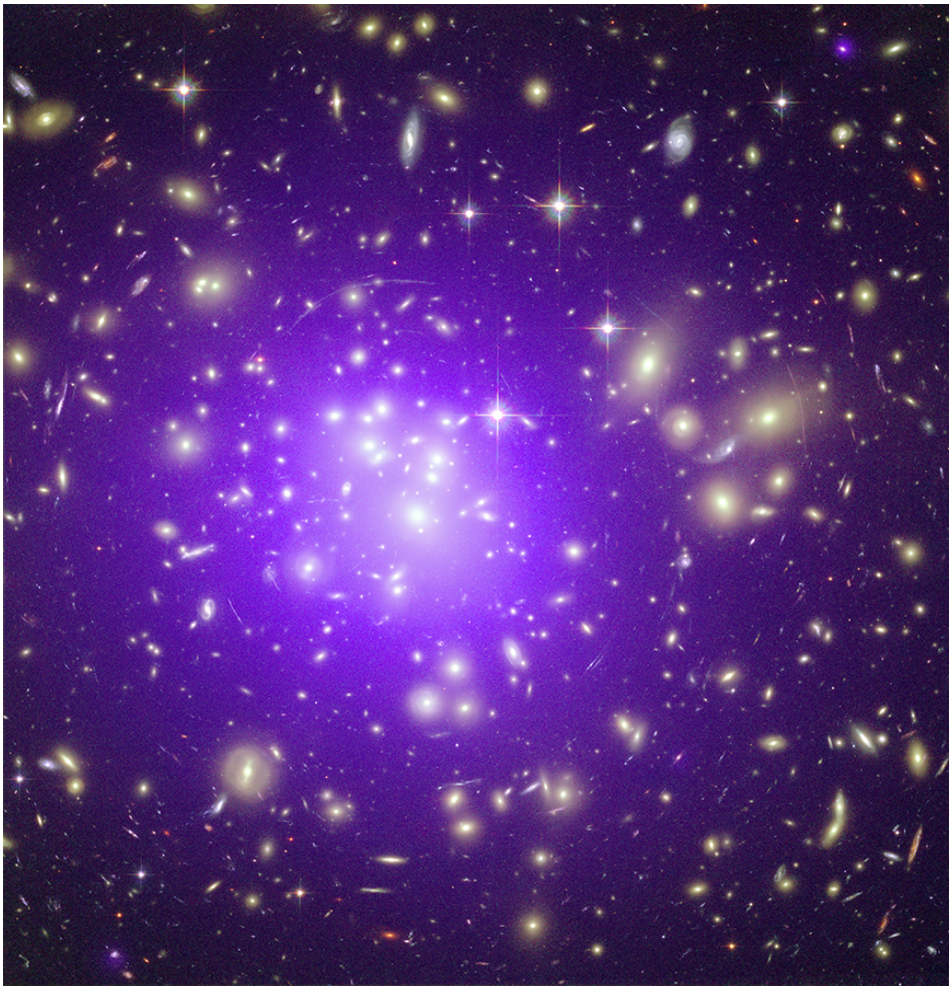

Figure 1.2: Composite image of the Abell 1689 galaxy cluster showing both the galactic population of the cluster (yellow) as well as the intracluster medium (purple). Image credit: X-ray: NASA/CXC/MIT/Peng et al. (2009); Optical: NASA/STScI.

1970) effect. As low-energy CMB photons collide with the high-energy cosmic rays of the ICM, they are scattered up to higher energies. At the typical wavelengths at which the CMB is observed, this leaves behind a "shadow" created by the galaxy cluster, allowing these clusters to be detected up to the proto-cluster regime (e.g., Overzier 2016). Unlike X-ray observations, which are most sensitive to nearby galaxy clusters, the shadow in the CMB created by the SZ effect is largely redshift-independent. This makes SZ observations very valuable for the detection of distant galaxy clusters.

1.2 Active galactic nuclei

At the core of practically all galaxies, a SMBH can be found (e.g., Kormendy & Gebhardt 2001; Merritt & Farrarese 2001; Häring & Rix 2004). These SMBHs can be fed with cold gas from within the galaxy. This creates what is known as an active galactic nucleus (AGN, e.g., Fabian 1999). As the gas is captured by the gravitational pull of the black hole, the combination of its angular momentum and the black hole's spin compresses it into an accretion disk surrounding the black hole. The infalling material releases a large fraction (up to ∼10%) of its rest-mass energy in this process, which makes AGNs some of the most luminous objects in the Universe.

AGNs have been empirically classified into several categories, depending on their observed features. These features probe different physical properties. In addition, the angle with which we observe the black hole and its accretion disk can play a critical role in obscuring and revealing particular components (e.g., Antonuci 1993; Urry & Padovani 1995; Netzer 2015).

For some AGN we have a direct view of the extremely hot and high-velocity gas of the accretion disk near the black hole. In optical observations, such systems show high luminosities and broad emission lines, and are classified as Type 1 AGNs. On the contrary, if we are viewing the AGN from the side, the dusty torus obscures the inner region near the SMBH, causing us to only observe the slowly-moving gas towards the outer regions of the accretion disk. These systems show relatively narrow emission lines, and are classified as Type 2 AGNs (e.g., Khachikian & Weedman 1974).

Depending on the ratio between the radio flux and the optical flux, AGN can also be classified into the radio-loud of radio-quiet categories (Kellerman et al. 1989). Radio-loud AGNs feature jetted outflows, which are ejected from the inner region of the black hole along the spin axis of the black hole up to relativistic speeds. An example of this is shown in Figure 1.3. These jetted outflows can escape the host galaxy of the AGN and propagate into intergalactic space. Depending on the morphology of these outflows, these can be classified as either a type 1 or a type 2 within the Fanaroff-Riley scheme (Fanaroff & Riley 1974). A Fanaroff-Riley Type 1 (or FR-I) typically shows bright jets near the AGN, which slowly diffuse away as they propagate away from the core of the AGN. On the other hand, a Fanaroff-Riley Type 2 (or FR-II) source has jets which terminate in hot spots on opposite sides of the AGN, typically surrounded by radio lobes.

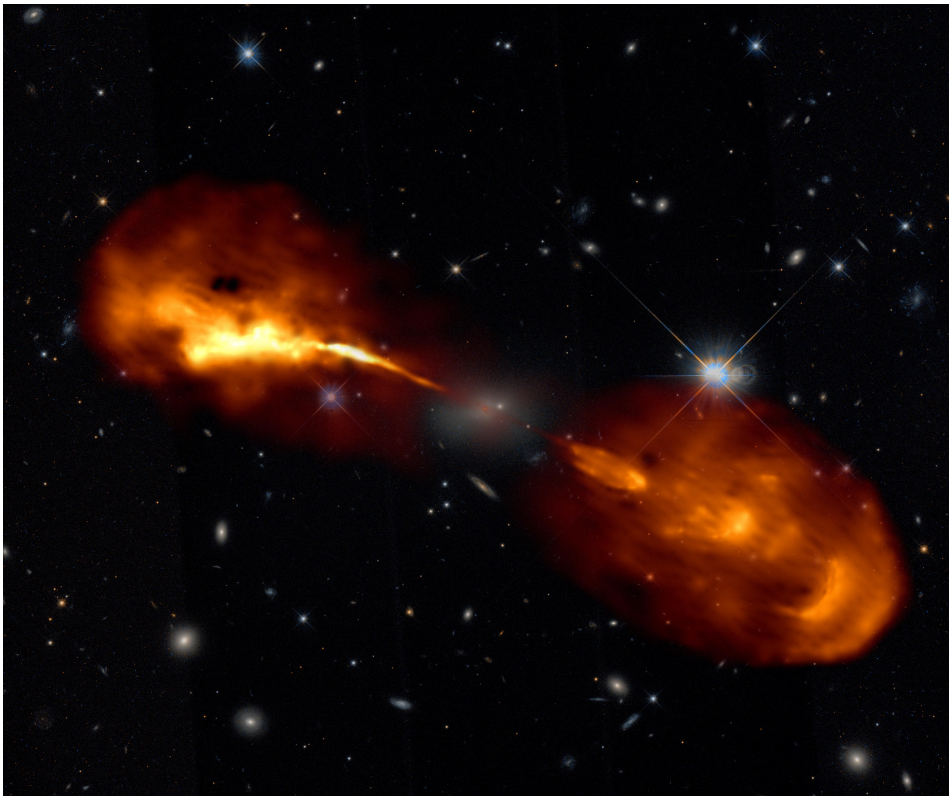

Figure 1.3: Composite image of Hercules A. The high-resolution 144 MHz radio image is shown in orange, and reveals two relativistic jets shooting away in opposite directions from the central supermassive black hole. Image credit: R. Timmerman/LOFAR, Hubble Space Telescope.

At the extremely luminous end, we find quasi-stellar objects (QSOs) or quasars, which can feature bolometric luminosities up to 10^{47} erg/s, and are most commonly found at relatively high redshifts of $z \approx 2$. Their brightness allows these objects to be detected at very large distances, making these objects valuable probes into the Early Universe.

1.3 Feedback

Many processes related to galaxies, stellar populations and compact objects result in feedback cycles. These cycles are critical to understand as they play a major role in the formation and evolution of many different types of objects. Two of the main forms of feedback in galaxies are supernovae feedback (e.g., Dale 2015) and AGN feedback (e.g., Brüggen & Kaiser 2002; McNamara & Nulsen 2007; Fabian 2012)

Supernovae feedback primarily occurs in star-forming regions. As gas clouds collapse under their self-gravity, stars of different masses form. The more massive stars have relatively short lifetimes and terminate as supernovae. These supernova explosions release large amounts of energy into the surrounding gas, produce shock waves and supply metals to their environment. This impacts the formation of new stars, by simultaneously disrupting gas which would have otherwise formed new stars and affecting the chemical composition of new stars.

Similarly, active galactic nuclei can also become part of the feedback cycle. An AGN has two main modes of feedback: radiative and mechanical feedback. Radiative feedback (also known as quasar-mode feedback, Croton et al. 2006) occurs due to the intense luminosity of the accretion disk. Due to the extreme temperature generated within the accretion disk, strong emission across practically all of the electromagnetic spectrum is released. This emission is so intense that its radiation pressure can expel the gas from the environment of the AGN and even large parts of the host galaxy. Not only can this restrict the inflow of new gas to the AGN, it can also limit the star-formation rate in the galaxy.

Secondly, mechanical (or radio-mode) feedback occurs as the matter falling towards the AGN is accelerated by the magnetic field of the black hole along its spin axis up to relativistic speeds, creating two jets of magnetized plasma travelling in opposite directions away from the AGN, as shown in Figure 1.4. Despite only constituting a fraction of the infalling matter, these jets can carry away a significant fraction of the available energy. In galaxy clusters, these typically escape the host galaxy and travel into the cluster environment. Here, they eventually slow down and end up producing large radio lobes (Bridle & Perley 1984). These radio lobes inflate against the external pressure of the ICM, producing bubbles or cavities within the ICM (e.g., Böhringer et al. 1993; Carilli et al. 1994). This way, the AGN is able to return energy to the cooling ICM, which initially fed the AGN, thereby preventing it from cooling down at its maximum rate. In turn, this reduces the star-formation rate of the central galaxies within the cluster. Unlike radiative feedback, which typically continues to grow in intensity as the AGN is fueled by more infalling matter, mechanical feedback is generally thought to level off at a

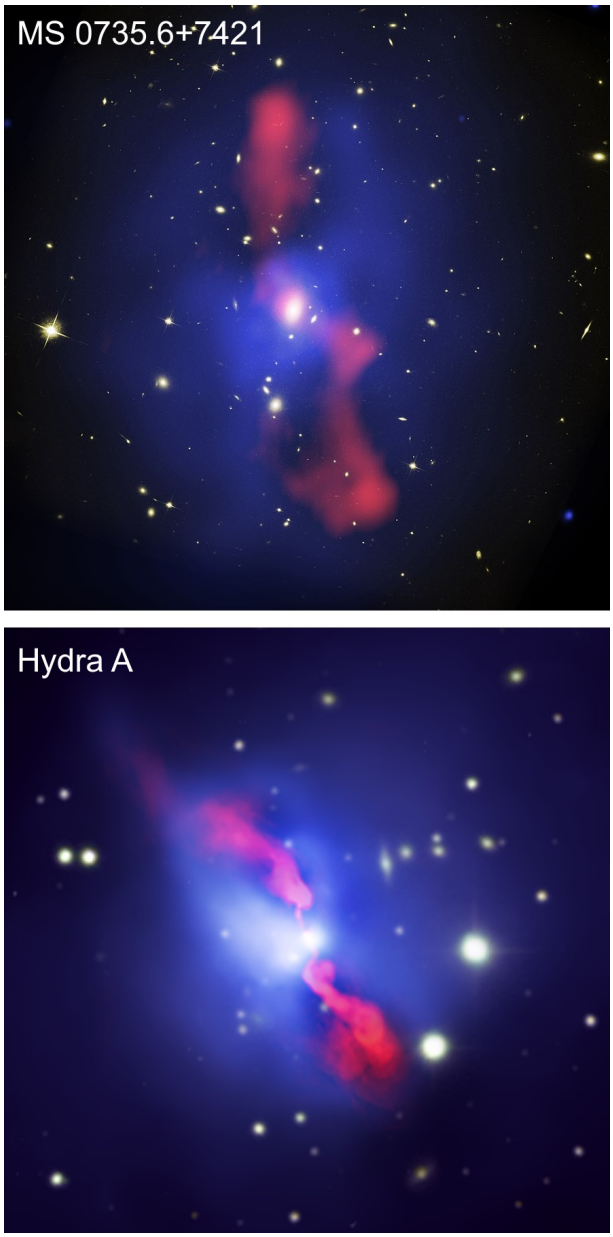

Figure 1.4: AGN feedback in the Hydra A and MS 0735.6+7421 galaxy clusters. The radio lobes, as observed at radio wavelengths, are shown in red. The ICM, observed at X-ray wavelengths, is shown in blue. Image credit for Hydra A: NASA/NSF/NRAO/CXC/VLA/Canada-France-Hawaii-Telescope/DSS/U.Waterloo/C.Kirkpatrick et al. Image credit for MS 0735.6+7421: NASA/ESA/CXC/STScI/NRAO/Univ. Waterloo/Ohio Univ./McNamara et al. (2009)

few percent of the Eddington rate (Russell et al. 2013), thereby allowing AGNs to produce feedback through both modes at different intensities. This provides a valuable opportunity to study not only the evolution of the ICM and the galaxies within the ICM, but also the growth of the SMBH powering the AGN.

Through the interaction between the radio lobes and the ICM, the average power injected by radio-mode AGN feedback into the cluster environment can be measured (e.g., Bîrzan et al. 2004; Rafferty et al. 2006; McNamara & Nulsen 2012). The total energy injected by the AGN can be estimated as the work required to inflate the radio lobes up to their current volume against the external pressure of the ICM plus the internal energy of the radio lobes. Assuming the radio lobes are composed of a relativistic gas, they will have an adiabatic index of $\gamma = 4/3$, and therefore we obtain

$$E_{\rm cav} = E_{\rm internal} + W = \frac{1}{\gamma - 1} pV + pV = 4pV. \tag{1.1}$$

By dividing this total energy output by the estimated age of the radio lobes, the average energy output of the AGN can be calculated. The age estimate is generally relatively uncertain and requires an assumption for the dynamics of the radio lobe. As the radio lobes are less dense than the surrounding ICM, they will buoyantly rise away from the center of the cluster. By assuming this dominated the motion or the radio lobe, the distance between the lobe and the AGN can be converted to an age estimate. An alternative is the assumption that the lobe travels at the speed of sound through the ICM, allowing for a similar conversion between distance and age. Typically, these estimates agree relatively well.

The feedback process is generally most reliably studied in relaxed clusters, as the cooling and heating processes can be assumed to be roughly in a steady state. We often observe the central ICM in a relaxed cluster to cool down, albeit not as rapidly as predicted. Nevertheless, this produces a cool-core region surrounding the BCG (e.g., Kaastra et al. 2001; Peterson et al. 2003). These cool cores generally do not survive merger events, making them an excellent indicator for relaxed galaxy clusters.

Current observations suggest that AGNs in galaxy clusters underwent a shift from operating primarily in quasar-mode in the Early Universe to operating primarily in radio-mode at the present day (Hlavacek-Larrondo et al. 2013). Currently, two scenarios would be consistent with this trend. Either the population of quasars increases in brightness towards higher redshifts, leading to sources being more likely to be detected at these higher redshifts, or there is an increase in the fraction of SMBHs which are active as quasars compared to the present day. The first scenario more naturally fits the data that AGNs produce more quasar-mode feedback towards high redshifts, but the lack of detection of quasar-mode feedback in some nearby clusters even with very deep X-ray observations leans more towards the second scenario. The evolution of AGN feedback over cosmic time would not only be a valuable probe to help constrain the environmental conditions of the AGNs in galaxy clusters, but it would also form a key constraint in models of the formation and evolution of galaxy clusters.

1.4 Observational instruments

Two parts of the electromagnetic spectrum are of particular interest for studies of active galactic nuclei and galaxy clusters: the radio and X-ray regimes. The immediate environment of the black hole is bright across practically the entire electromagnetic spectrum, including the radio and X-ray regimes. However, in addition to this, radio observations also provide an excellent view of the relativistic jets as they propagate into the cluster environment. The charged particles within these jets interact with the present magnetic field to produce synchrotron emission. This type of emission can generally be described using a power-law function within the radio regime, with the lower frequencies featuring higher intensities. Towards the high-frequency end of the radio spectrum, synchrotron emission typically cuts off due to aging. As the high-energy electrons produce high-frequency radio waves, they rapidly lose energy, causing these electrons to shift down to lower energies and therefore also lower frequencies.

Meanwhile, X-ray observations can be used to reveal the ICM. Due to its extremely high temperature, the ionized particles within the ICM produce thermal bremsstrahlung in the X-ray regime. Within the diffuse emission of the ICM, the cavities produced by AGN activity can also be detected. Furthermore, the spectrum of the X-ray emission can be used to constrain the physical properties of the ICM, such as the temperature and internal pressure.

1.4.1 Very Large Array

For the high-frequency radio observations used in this thesis, we rely on observations taken with the Very Large Array (VLA). This observatory was built near Socorro, New Mexico and is currently operated by the National Radio Astronomy Observatory (NRAO), Although commissioned in 1980, it has since been upgraded in 2012 to remain at the frontier of radio astronomy to date. This upgrade primarily focused on updating the receivers to improve the sensitivity and bandwidth coverage.

The VLA consists of 27 antennas with 25-meter fully steerable dishes divided over three arms in a Y-shape, as shown in Figure 1.5. To be able to perform both low- and high-resolution observations, these antennas are positioned on rails and can be placed in one of four configurations. The A-configuration, which is intended for the highest resolution imaging, the VLA has baseline lengths between 0.68 km and 36.4 km. In this configuration, the VLA offers an angular resolution of just over an arcsecond at 1.5 GHz (L band) and less than 0.05 arcseconds at 45 GHz (Q band). The array shrinks by roughly a factor of three each step from the A-configuration to the D-configuration, where it finally has baselines lengths between 35 m and 1.03 km. The VLA's set of 10 receivers offers a continuous frequency coverage from 1 to 50 GHz, with additional bands around 350 MHz (P band) and 74 MHz (4 band).

Figure 1.5: The Very Large Array in New Mexico, USA, shown in A-configuration. In the foreground, the antenna on position W08 is visible, with the Northern arm located in the background.

1.4.2 LOFAR

Towards the low-frequency radio regime, the LOw Frequency ARray (LOFAR, Van Haarlem et al. 2013) is the telescope offering the highest angular resolution. LOFAR contains two sets of antennas: the low-band antennas (LBA), which operate between 10 and 90 MHz, and the high-band antennas (HBA), which operate between 110 and 240 MHz. Instead of having movable dishes, LOFAR is divided up into stations which each contain multiple antennas. These antennas can be pointed to any position on the sky through electronics. After a direction has been selected, the difference in signal path length between all the individual dipoles of a station is calculated and corrected for. By summing up the signal accounting for this difference (also known as *beam-forming*), the signal from the selected direction is amplified, while signals from other directions are suppressed. As the pointing of the telescope is mainly performed digitally, LOFAR is able to observe multiple directions simultaneously, limited mainly by computational resources.

Although the core of LOFAR is located in the Netherlands, LOFAR also has stations located in other countries throughout Europe. This gives LOFAR a rare combination of very short baselines (down to 68 meters), and very long baselines (up to ∼1890 km). At the core, a cluster of six stations forms the "superterp" (see Figure 1.6). This is surrounded by the remaining core stations at slightly larger distances. For the core stations, the HBA tiles are split up into two separate substations. Further from the superterp, but still located in the Netherlands, LOFAR has additional remote stations, which use a combined station design. Finally, the international stations are larger versions of the Dutch stations, and are distributed across Europe.

Processing and analysing LOFAR observations provides several significant challenges. First, LOFAR observations are sensitive to large areas of the sky instanta-

Figure 1.6: The core of the LOw Frequency ARray (LOFAR), known as the "superterp". The LBA stations are the more "randomly" distributed wire dipoles, whereas the HBA stations are the gridded sets of dark grey boxes. Image credit: LOFAR.

neously. Therefore, it is difficult to isolate the emission from one radio source. For calibration and deconvolution, this requires imaging large fields, which is computationally expensive (Sweijen et al. 2022). Additionally, the data volumes which are produced by LOFAR observations are very challenging. A standard 8-hour observation produces around 4 terabytes of compressed data, or 14 terabytes of uncompressed data. This puts considerable hardware constraints on any computing cluster which is used for LOFAR data processing, and can make it difficult to work on large numbers of observations. Another challenge is that the remote and international stations operate on independent clocks due to their physical separation. This can introduce errors if these clocks drift relative to each other. To correct for this, careful calibration must take place. Fortunately, the LOFAR 2.0 upgrade is planned to place all remote stations on the same physical clock, largely resolving this problem for these stations. Finally, at the low radio frequencies where LOFAR observes, the Earth's ionosphere typically dominates the perturbation of the wavefront through the atmosphere (Intema et al. 2009; Mevius et al. 2016). Problematically, the ionosphere introduces phase errors which scale non-linearly with frequency. Generally, the first order effect is most significant. This is known to cause dispersive delays, which scale inversely with frequency. However, for the longest HBA baseline or generally in the LBA regime, the second order can not be neglected. Especially during high solar activity, the second order term can grow to be very significant. This can be recognized as Faraday rotation, and scales as inverse frequency squared (Sotomayor-Beltran et al. 2013). On top of that, these effects are strongly direction dependent, and can vary significantly across the field of view (Albert et al. 2020). Therefore, a single calibration solution

which corrects for ionospheric perturbations across the entire field of view does not exist in general. This can be resolved by obtaining independent calibration solutions for multiple directions within the field and interpolating these. However, this is again a computationally demanding strategy.

All of the aforementioned challenges are intensified by the inclusion of LOFAR's international stations. These stations increase the angular resolution of LOFAR by a factor of around 20. With the HBA, this means that the angular resolution decreases from 6 arcseconds for the Dutch array to 0.3 arcseconds for the international array. To image the same field of view with the international stations requires roughly 400 times as many pixels. The increased angular resolution also results in decreased surface brightness sensitivity. After all, the same flux density will be distributed over far more individual resolution elements. Despite the added sensitivity gained by including the international stations, the resolution increase still causes a surface brightness sensitivity decrease of around a factor of 300. Additionally, the calibration models used to perform the calibration of the international stations must meet far higher fidelity standards than those used for the Dutch array. To calibrate the long baselines provided by the international stations, it is also required to have signal on corresponding angular scales. As it turns out, not many sources are simultaneously compact and bright at low frequencies. Finally, the phase errors due to the ionosphere increase with baseline length, which makes the international stations considerably more difficult to calibrate.

As wide-field imaging with the international stations is very computationally expensive, we are unable to perform calibration using the entire field of view, as we would do with the Dutch stations. Instead, the calibration strategy developed by Morabito et al. (2022) is based on imaging single targets, also known as "post stamp" imaging. By phasing up the core stations, averaging the data and applying a lower limit to the baseline lengths used during calibration, it is possible to reduce the interference from unrelated radio sources near the target of interest. The Long Baseline Calibrator Survey (LBCS, Jackson et al. 2016, 2022) provides a valuable catalog of bright and compact radio sources which can provide the signal on the long baselines to perform the calibration. Taking advantage of LOFAR's wide field, it is generally possible to find one of these calibrator sources within the field of view. This is particularly advantageous, as it allows for calibration solutions derived on the "in-field" calibrator to be applied to the target source without any temporal interpolation. Due to the non-linear nature of ionospheric phase errors, the fringe-fitting technique commonly used in VLBI is not applicable to LOFAR observations. Instead, we have to resort to a straight-forward phase solve in small bins of time and frequency, with only smoothing along the frequency axis to enhance the signal-to-noise ratio (Van Weeren et al. 2021).

The calibration of the Dutch part of the array is currently a solved problem (Van Weeren et al. 2016; Williams et al. 2016; de Gasperin et al. 2019), enabling the LOFAR Two-Metre Sky Survey (LoTSS, Shimwell et al. 2017, 2019). This survey aims to observe the entire Northern hemisphere using the Dutch LOFAR stations to provide a 144 MHz radio map with an angular resolution of 6 arcseconds. The current latest public data release (DR2, Shimwell et al. 2022) covers 27% of the Northern sky, reaching a depth of 83 µJy/beam. In addition to the images, a radio

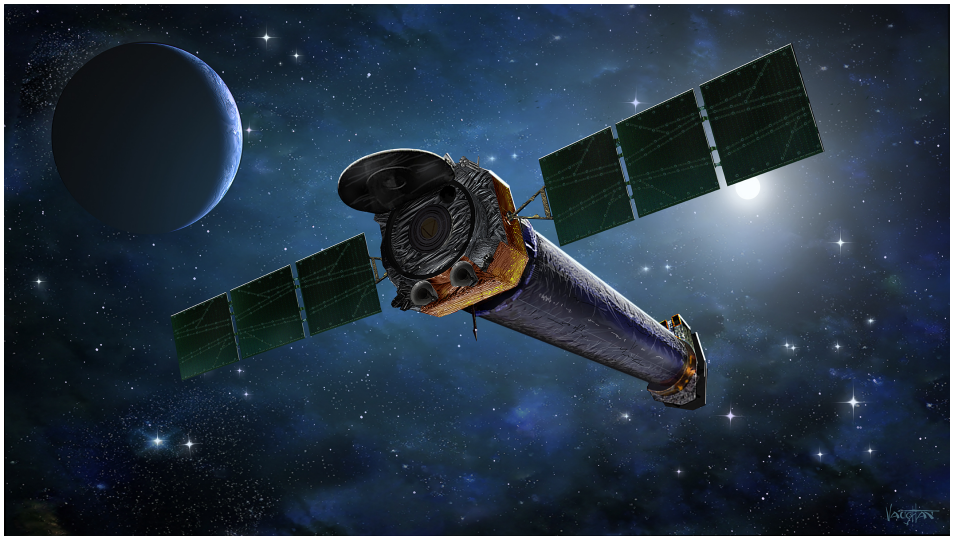

Figure 1.7: Artist impression of the Chandra X-ray Observatory. Image credit: NASA/CXC & J.Vaughan

source catalogue containing 4,396,228 sources was published.

1.4.3 Chandra

To study a critical component of galaxy clusters - the ICM - observations in the X-ray regime are required. As Earth's atmosphere is not transparent to X-ray photons, all X-ray observatories are space-based. The prime instrument for high angular resolution X-ray observations at the present time is the Chandra X-ray Observatory (Weisskopf et al. 2000), launched in 1999 by the Space Shuttle into a highly elliptical orbit (see Figure 1.7). This observatory offers a unique combination of angular and spectral resolution, which provide a uniquely detailed view of the X-ray sky. The Chandra X-ray Observatory contains multiple science instruments, such as the High Resolution Camera, the Low and High Energy Transmission Gratings and the Advanced Charged Couple Imaging Spectrometer (ACIS).

Of particular interest for galaxy cluster observations is the ACIS. By measuring both the direction and energy of incoming X-ray photons, the ten CCD chips of the ACIS provide a combination of imaging and spectroscopy with an angular resolution of only 0.5 arcseconds between 0.2 and 10 keV. Using this data, we are not only able to constrain the morphology of the ICM, but also its internal physical conditions such as the temperate and pressure. Additionally, the high angular resolution of the ACIS also allows the brightness from the AGN and the surrounding ICM to be disentangled.

1.5 Key questions

Active galactic nuclei and galaxy clusters have been active fields of research for multiple decades. Key questions have remained unanswered as to the formation and evolution of galaxy clusters, and the role of AGNs in that process. One of the key questions we are hoping to answer is how AGN feedback co-evolves with galaxy clusters. Initial indications suggest that AGN feedback may switch from a predominantly quasar-mode process to a more radio-mode process. Such an evolution in the way AGN feedback operates is critical to the interaction between the SMBH and its environment, and therefore also has a profound effect on the state of the ICM and star-formation in the cluster galaxies. Especially towards the Early Universe, observational constraints limit our understanding of the AGN feedback process.

Additionally, we need to understand how the mechanism of energy transfer from the relativistic jets of the AGN to the larger cluster environment. Fundamentally, this question is two-fold. First of all, it's not clear how the energy contained in the relativistic jets transfers to the ICM. Secondly, this energy also needs to be dissipated throughout the ICM. Radio-mode feedback is only emitted in two opposite directions in the cluster environment, but the ICM is distributed throughout the cluster.

Aside from the impact the AGN has on the large-scale environment, it is also valuable to understand the coupling to the environment of the host galaxy. For the host galaxy, the mode of feedback plays a significantly different role, with quasar-mode feedback having a much stronger effect. In addition, the host galaxy essentially regulates the flow of matter which feeds the AGN, and therefore also is key in understanding the duty cycle of the AGN.

Finally, the role of cluster mergers requires further investigation. Most research into AGN feedback gives preference to relaxed clusters due to practical considerations, but the effect of cluster mergers can not be neglected. Cluster mergers have a major impact on the dynamical state of the ICM as they can disrupt the cool core and introduce large-scale sloshing motions. Furthermore, the merging of the BCGs and eventually the central SMBHs plays a key role in their evolution, and therefore also the feedback cycle.

1.6 Thesis outline

The goal of this thesis is to study the study the operation of radio-mode feedback in galaxy clusters using radio and X-ray observations, with a particular focus on exploring the new parameter space available to us through the International LOFAR Telescope.

In **Chapter 2**, we study the mini halo and AGN of the Phoenix cluster at a redshift of $z = 0.597$. This cool-core cluster shows very high star-formation rates, indicating that the central AGN is failing to inhibit the cooling flow. Using multifrequency VLA observations between 1 and 12 GHz, we investigate the operation of the AGN in the center of the cluster as well as the origin of the mini

halo. Based on the correlation between the X-ray and radio morphologies of the mini-halo, we conclude that the mini-halo is most likely formed through turbulent re-acceleration. Additionally, we find that time variability of the AGN likely results in an observed disconnection between the radio and X-ray properties of the system.

In **Chapter 3**, we use a combination of multifrequency VLA observations and ILT observations of Hercules A to study the origin of ring structures in one its radio lobes. Through spectral index measurements, we are able to constrain the electron population of the synchrotron-emitting plasma. This allows us to differentiate between the shock model and the inner-lobe model which both try to provide an explanation for the presence of the observed ring structures. Based on the spectral curvature trend in the rings, we find that the inner-lobe model is most consistent with our observations.

In **Chapter 4**, we present a sample of 14 cool-core galaxy clusters observed with the ILT, of which 8 observations including the international stations. With this sample, we check whether the low-frequency observations taken with LOFAR detect the complete volume of the radio lobes, as detected in X-ray observations. This way, we demonstrate that ILT observations are able to constrain this volume, which plays a key role in determining the energy output of the central AGN. In turn, this enables us to reach higher redshifts than before and measure the power of an AGN into the early Universe.

In **Chapter 5**, we report on the results of a pilot project where we observe a high redshift ($z > 0.6$) sample of galaxy clusters with the ILT. We test the method demonstrated in Chapter 4 on a high-redshift sample of targets for the first time to confirm that the method is feasible in the distant Universe, where X-ray observations alone can not reach the required sensitivity.

1.7 Future prospects

With the aid of a new generation of observatories such as the International LOFAR Telescope, the Square Kilometer Array (SKA), the ngVLA, XRISM, Athena and Euclid, as well as theoretical progress with cosmological simulations such as the EAGLE simulations (e.g., ARTEMIS and COLIBRI, Crain et al. 2015; Schaye et al. 2015; Font et al. 2020), further progress can be made to obtain the answers to the aforementioned questions. Large surveys of the sky which probe deeper than before provide valuable catalogs of galaxies, AGNs and galaxy clusters, and enable the population of these objects to be investigated in a statistically meaningful way. For example, the Euclid mission is expected to catalog $> 10^5$ galaxy clusters up to a redshift of $z = 2$ (Euclid Collaboration 2019), after which follow-up observations of these objects can be performed with next-generation instruments across a wide range of the electromagnetic spectrum.

Two of the main upcoming radio observatories are the SKA in the Southern Hemisphere and the ngVLA in the Northern Hemisphere. Both of these observatories will offer a revolutionary sensitivity to the radio sky together with an excellent angular resolution. This will not only enhance our understanding of bright and

nearby radio sources, but also enable research on faint and distant radio sources which have not previously been studied. Similarly, the upcoming XRISM and Athena X-ray observatories are expected to provide an unparalleled combination of spectral resolution and sensitivity, which will enable groundbreaking new research on the physical properties of both AGNs and the ICM of galaxy clusters.

Of particular interest to this thesis is also the future upgrade of the International LOFAR Telescope to LOFAR 2.0 by ASTRON. This upgrade will improve our ability to perform high-resolution radio observations below 100 MHz, which will offer an unprecedented ability to study steep-spectrum radio emission. In time, this will provide us with a much more accurate understanding of the physics that govern AGN, galaxy clusters, and by extension our entire Universe.

2

Very Large Array observations of the mini-halo and AGN feedback in the Phoenix cluster

Roland Timmerman, Reinout J. van Weeren, Michael McDonald, Alessandro Ignesti, Brian R. McNamara, Julie Hlavacek-Larrondo and Huub J. A. Röttgering,

Published in Astronomy & Astrophysics, February 2021, volume 646, A38.

Abstract

The relaxed cool-core Phoenix cluster (SPT-CL J2344-4243) features an extremely strong cooling flow, as well as a mini halo. Strong star formation in the brightest cluster galaxy indicates that active galactic nuclei (AGN) feedback has been unable to inhibit this cooling flow. We aim to study the strong cooling flow in the Phoenix cluster by determining the radio properties of the AGN and its lobes. In addition, we used spatially resolved radio observations to investigate the origin of the mini halo. We present new multifrequency Very Large Array 1–12 GHz observations of the Phoenix cluster which resolve the AGN and its lobes in all four frequency bands as well as the mini halo in the L and S bands. Using our L-band observations, we measure the total flux density of the radio lobes at 1.5 GHz to be 7.6 ± 0.8 mJy, and the flux density of the mini halo to be 8.5 ± 0.9 mJy. Using high-resolution images in the L and X bands, we produced the first spectral index maps of the lobes from the AGN and find the spectral indices of the northern and southern lobes to be -1.35 ± 0.07 and -1.30 ± 0.12, respectively. Similarly, using L- and S-band data, we mapped the spectral index of the mini halo, and obtain an integrated spectral index of $\alpha = -0.95 \pm 0.10$. We find that the mini halo is most likely formed by turbulent re-acceleration powered by sloshing in the cool core due to a recent merger. In addition, we find that the feedback in the Phoenix cluster is consistent with the picture that stronger cooling flows are to be expected for massive clusters such as this one, as these may feature an underweight supermassive black hole due to their merging history. Strong time variability of the AGN on Myr timescales may help explain the disconnection between the radio and the X-ray properties of the system. Finally, a small amount of jet precession of the AGN likely contributes to the relatively low intracluster medium re-heating efficiency of the mechanical feedback.

2.1 Introduction

The emission of strong X-ray radiation by the intracluster medium (ICM) in galaxy clusters suggests that this medium should often cool down rapidly: within a timescale of $\sim 10^9$ years or fewer (e.g., Fabian 1994). As the ICM cools down, it is expected to flow down the gravitational well of the cluster, and accrete onto the galaxy at the center. This accretion of matter should then trigger star formation in the central galaxies proportionally to the cooling flow of the ICM. However, both this cooling of the ICM and the star formation in the center of the cluster are observed to be much weaker than expected (Fabian et al. 1982; McNamara & O'Connell 1989; Page et al. 2012; McDonald et al. 2018), leading to what is known as the "cooling flow problem". The generally accepted solution to this problem is that feedback from active galactic nuclei (AGN) supplies energy to the ICM in the form of radiation and jetted outflows of plasma, thereby preventing the medium from cooling down (e.g., Brüggen & Kaiser 2002; McNamara & Nulsen 2007; Fabian 2012).

Studying this feedback process is essential to our understanding of the formation and evolution of galaxies, as it plays a critical role in the cooling of the ICM and the star formation in galaxies across cosmic time (e.g., Matteo et al. 2005; Croton et al. 2006; Menci et al. 2006; Sijacki et al. 2007; del P. Lagos et al. 2008; Ciotti et al. 2010; Mathews & Guo 2011; Vogelsberger et al. 2014; Rasia et al. 2015). In particular, clusters of galaxies form a great opportunity to study AGN feedback, due to the relatively dense ICM, which is capable of creating strong cooling flows. The ICM is often also dense enough to keep the jetted outflows from the AGN contained, which allows this mechanical form of feedback to be studied in detail (McNamara & Nulsen 2012).

The interaction between the ICM and the jetted outflows from the AGN can be directly observed in the X-ray regime. As the jetted outflows displace the ICM, they create large cavities that are observed as depressions in X-ray observations. At radio frequencies, bubbles of synchrotron-emitting plasma are observed to be coincident with these cavities, verifying that these cavities are produced by the AGN (Gull & Northover 1973; Gitti et al. 2012b).

Despite much research into AGN feedback in galaxy clusters, many open questions remain. Of particular interest for this work is the connection between the central AGN and the mini halo surrounding the brightest cluster galaxy (BCG). Mini halos are faint, diffuse synchrotron-emission regions commonly found in relaxed cool-core galaxy clusters. They span a region of a few hundred kpc, as they are generally confined to the cool-core region of a galaxy cluster. Mini halos often feature an amorphous shape, and have been found to show steep spectral indices of around $\alpha = -1$ to $\alpha = -1.5$ (Gitti et al. 2004; Giacintucci et al. 2019; Van Weeren et al. 2019).

The origin of mini halos remains a topic of debate, which is hampered by the difficulty of obtaining high-quality data on mini halos, as the central AGN often dominates the view. The emission of synchrotron radiation in the mini halo means that there must be a population of cosmic-ray electrons present in a magnetic field. However, based on the short lifetime of these electrons of 10–100

Myr, they must be accelerated in-situ (Brunetti & Jones 2014). Two mechanisms are proposed by which the electrons can be accelerated. In the hadronic model, relativistic, secondary electrons are injected by collisions between relativistic and thermal protons (e.g., Pfrommer & Enßlin 2004; Fujita et al. 2007). This model predicts the presence of diffuse gamma-ray emission, produced by the same proton-proton collisions and a gradual decrease in radio emission due to the diffusion of cosmic ray (CR) protons in the ICM. In the case of radio emission produced purely by secondary electrons, the spectral index would depend only on the energy distribution of the CR protons, and hence it would not vary with the radius.

Alternatively, according to the turbulent re-acceleration model, fossil electrons from the AGN are re-accelerated to high energies by magneto-hydrodynamic turbulence in the cluster (e.g., Gitti et al. 2002; Mazzotta & Giacintucci 2008; ZuHone et al. 2013). This turbulence is thought to generally be caused by strong cooling flows or a merger event in the recent history of the cluster, although recent observations of an Mpc-scale radio halo in a cool core cluster (Bonafede et al. 2014) and ultra-steep-spectrum emission extending beyond the cool core (Savini et al. 2018) have challenged that idea. The turbulent re-acceleration model predicts a possible steepening of the spectrum with radius and a radio brightness profile that is strongly contained by the cold fronts produced in the ICM by a recent merger event. These cold fronts are density discontinuities created by the cold and dense gas from the cool core or a subcluster moving through the surrounding hot gas, and therefore they also commonly form the boundary of a turbulent region (e.g., Markevitch & Vikhlinin 2007). Accurately determining the properties of mini halos is essential to understanding the underlying acceleration mechanism, and thereby their origin.

In this paper, we adopt a ΛCDM cosmology, with cosmological parameters of $H_0 = 70\text{km s}^{-1}\text{ Mpc}^{-1}$, $\Omega_m = 0.3$, and $\Omega_\Lambda = 0.7$. In this cosmology, the luminosity distance to the Phoenix cluster at $z = 0.597$ is 3 508 Mpc, and an angular scale of 1 arcsecond at this redshift corresponds to 6.67 kpc. Furthermore, we followed the convention of defining our spectral indices according to $S \propto \nu^{\alpha}$.

2.2 The Phoenix cluster

In this work, we focus on the Phoenix cluster (SPT-CL J2344−4243), a massive galaxy cluster at redshift $z = 0.597$ discovered by Williamson et al. (2011) in the 2 500 deg^2 South Pole Telescope Survey. The Phoenix cluster is a relaxed cool-core cluster featuring a type 2 QSO (Ueda et al. 2013), and it is characterized by its high cooling flow and star formation rate. X-ray, optical, and infrared observations by McDonald et al. (2012, 2013, 2019) show a cooling flow of $\sim 3\,100\ M_\odot$ per year, with a star-formation rate of $\sim 800\ M_\odot\ yr^{-1}$. Whereas the star formation rate is generally on the order of 1% of the predicted cooling flow, for the Phoenix cluster this ratio is almost 30%, indicating that the feedback process has not been able to completely inhibit the cooling flow. Spectroscopic observations of the warm and cold gas in the core of the Phoenix cluster suggest that this rapid star formation may be a short phase, as the molecular gas supply is expected to deplete on a

timescale of ~ 30 Myr (McDonald et al. 2014).

Using Chandra observations, Hlavacek-Larrondo et al. (2014) revealed the presence of X-ray cavities in the ICM. Follow-up research using deeper observations by McDonald et al. (2015, 2019) provided an estimate of the scale of these cavities of 8–14 kpc, which suggests a jet power from the AGN of $1.0^{+1.5}_{-0.4} \times 10^{46}$ erg s^{-1}. In addition, star-forming filaments extending up to 50–100 kpc from the core of the cluster were observed using deep optical imaging. ALMA observations also show molecular gas filaments measuring 10–20 kpc in length tracing the edges of the X-ray cavities (Russell et al. 2017).

Observations using the *Giant Metrewave Radio Telescope* (GMRT) uncovered a mini halo surrounding the BCG, which spans a region of 400–500 kpc (Van Weeren et al. 2014). This mini halo was later observed by Raja et al. (2020) using the *Karl G. Jansky Very Large Array* (VLA) in CnB configuration. By subtracting compact emission from their data, they detect the mini halo and derive a flux density of the mini halo at 1.5 GHz of 9.65 ± 0.97 mJy. They find that the 3σ contours of their map span a region of 310 kpc.

New deep Chandra and X-band VLA observations by McDonald et al. (2019) revealed radio jets that are coincident with the previously detected X-ray cavities. In addition, they present *Hubble* observations suggesting that the AGN may lift cool low-entropy gas up to larger radii, where it can cool faster than its fallback time, resulting in multiphase condensation. The gas kinematics and strong high-ionization emission lines indicate that relatively strong turbulence may be present in the core.

In this paper, we aim to investigate the strong cooling flow observed in the Phoenix cluster by imaging the AGN and its jetted outflows across a wide range of radio frequencies. In addition, we aim to study the origin of the mini halo by measuring its properties using spatially resolved radio observations for the first time.

2.3 Observations and data reduction

The Phoenix cluster was observed with the VLA in the L, S, C, and X bands, covering the frequency range from 1 GHz to 12 GHz (PI: McDonald, 17A-258). The X-band data of this project was previously presented by McDonald et al. (2019). In the L band, the VLA observed in both A and B configuration, which we complement with archival CnB-configuration observations (PI: Datta, 14B-397) recently presented by Raja et al. (2020). In the S, C, and X band, the VLA observed in A, B, and C configuration. The L- and S-band observations were recorded using 16 spectral windows of 64 channels each, resulting in a total bandwidth of 1 GHz and 2 GHz, respectively. The C- and X-band observations were recorded using 32 spectral windows of 64 channels each, resulting in a total bandwidth of 4 GHz for both bands. All new observations have a total of 2.5 hours of integration time per configuration. An overview of the observations is presented in Table 2.1.

For our new observations, we used 3C138 and 3C147 as primary calibrators

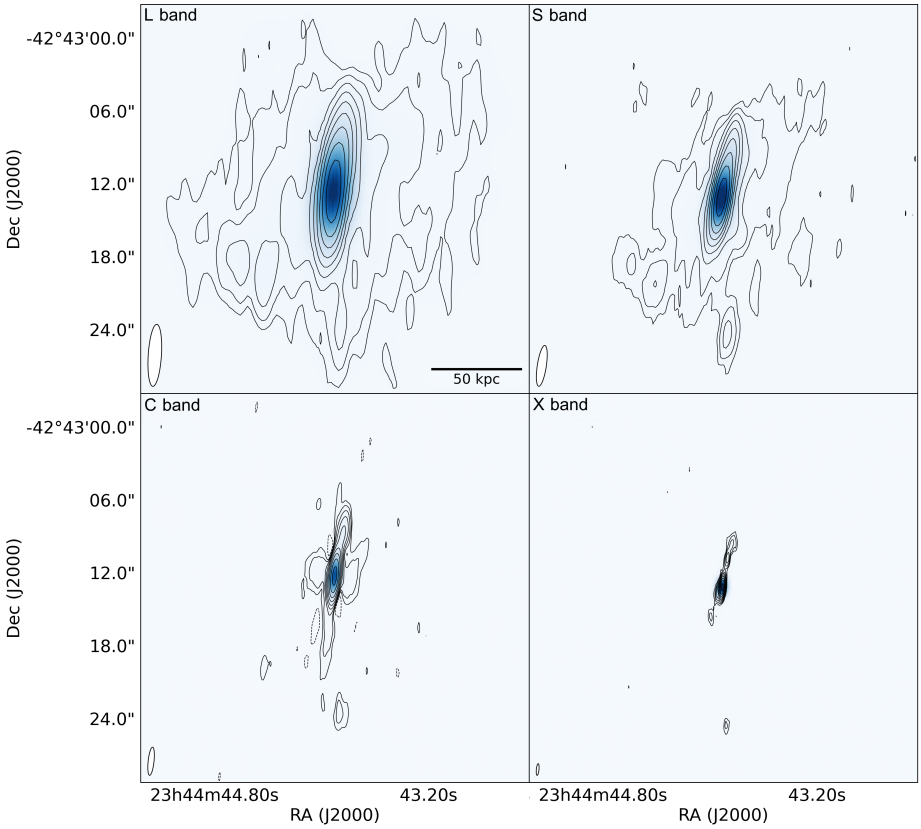

Figure 2.1: VLA images of Phoenix cluster in L band (top-left), S band (top-right), C band (bottom-left), and X band (bottom-right). Contours are drawn at [-1, 1, 2, 4, 8, ...] $\times\ 4\sigma_{\rm rms}$, where $\sigma_{\rm rms} = 10.8$ µJy beam^{-1} (L band), $\sigma_{\rm rms} = 5.9$ µJy beam^{-1} (S band), $\sigma_{\rm rms} = 4.3$ µJy beam^{-1} (C band), and $\sigma_{\rm rms} = 2.2$ µJy beam^{-1} (X band). The beam sizes are indicated in the bottom-left corners of each panel.

Table 2.1: Summary of the observations.

Configuration	Obs. date	Freq. (GHz)	Int. time (s)	$\theta_{\rm FWHM}$ (")
L band, A array	24 Mar. 2018	1-2	2	3 × 0.7
L band, B array	2 Nov. 2017	1-2	3	10 × 2
L band, CnB array *(archival)*	23 Jan. 2015	1-2	5	16 × 9
S band, A array	11 Mar. 2018	2-4	2	2 × 0.4
S band, B array	25 Sep. 2017	2-4	3	6 × 1
S band, C array	10 Jun. 2017	2-4	5	18 × 4
C band, A array	4 Mar. 2018	4-8	2	1 × 0.3
C band, B array	8 Sep. 2017	4-8	3	3 × 0.6
C band, C array	9 Jun. 2017	4-8	5	9 × 2
X band, A array	6 Mar. 2018	8-12	2	0.5 × 0.1
X band, B array	7 Sep. 2017	8-12	3	2 × 0.4
X band, C array	5 Jun. 2017	8-12	3	6 × 1

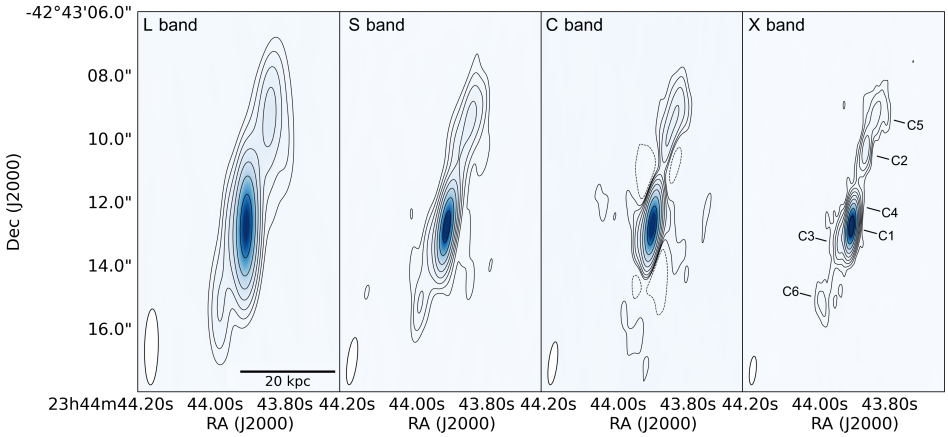

Figure 2.2: VLA images of Phoenix cluster in L band (robust -1.5), S band (robust -1), C band (robust -0.5), and X band (robust 0). Contours are drawn at [-1, 1, 2, 4, 8, ...] × $4\sigma_{\rm rms}$, where $\sigma_{\rm rms}$ = 40.8 µJy beam^{-1} (L band), $\sigma_{\rm rms}$ = 12.8 µJy beam^{-1} (S band), $\sigma_{\rm rms}$ = 6.9 µJy beam^{-1} (C band), and $\sigma_{\rm rms}$ = 2.2 µJy beam^{-1} (X band). The source components as detected by Akahori et al. (2020) using the ATCA are indicated in the X-band map. The beam sizes are indicated in the bottom-left corners of each panel.

with a total integration time of approximately five to ten minutes at the end of the observation. As the secondary calibrator, we used J0012-3954. Scans with an integration time of approximately two to three minutes on the secondary calibrator were repeated every 15 minutes. In the archival L band, CnB-array data, 3C48 was observed for 12 minutes as the primary calibrator. No secondary calibrator was included in this observation.

The data were reduced with the Common Astronomy Software Application (CASA; McMullin et al. 2007). The data reduction begins with a Hanning smoothing, the flagging of shadowed antennas, the calculation of gain elevation curves and corrections to the antenna positions, and the use of the TFCrop algorithm within CASA to apply automatic radio frequency interference (RFI) flagging. Next, manual flags were applied to exclude bad data from the calibration process. After the flagging, the initial complex gain solutions were calculated based on the central channels from each spectral window. These initial complex gain solutions were used to determine the delay terms. The bandpass calibration solutions were then derived based on the delay terms and the initial complex gain solutions. With the correct bandpass solutions applied, the complex gain solutions can be derived for the complete bandwidth of each spectral window. Using the polarized calibrator 3C138, we derived the global cross-hand delay solutions. The unpolarized calibrator, 3C147, then allowed the polarization leakage terms to be calculated. Finally, 3C138 was used again to calibrate the polarization angle. Using all relevant calibration tables, the complex gain solutions were redetermined, and the flux scale was set based on models of 3C138 and 3C147 by Perley & Butler (2013). The calibration solutions were then applied to the target source, after which the TFCrop and RFlag automatic flagging algorithms were used to remove previously undetected RFI. Next, the calibrated data of the target source were split out, after which point the AOFlagger software (Offringa et al. 2010) was used to remove any remaining RFI.

Finally, we improved the calibration through the process of self-calibration. We used CASA to calculate new calibration solutions and applied these to the data, and we used WSClean (Offringa et al. 2014) for the imaging and deconvolution. Each data set was self-calibrated by initially performing phase-only self-calibration, and later performing amplitude and phase self-calibration, with iteratively shorter calibration solutions. Then, all data sets of the same spectral band were concatenated to form one data set per band. These data sets were then self-calibrated again to obtain the final data sets. Imaging was performed using Briggs weighting (Briggs 1995) with a robust parameter of zero. The C-band data experienced issues during calibration, which is suspected to be caused by the very low declination of the source. For this reason, it is difficult to discern real structures from noise features near the AGN.

2.4 Results

The images we obtain are shown in Figure 2.1. The L-band image shows the central compact AGN with the diffuse mini halo surrounding it. The mini halo

Table 2.2: Properties of the images shown in Figure 2.1.

Freq. band	Flux density (mJy)	Peak flux (mJy beam^{-1})	rms noise (µJy beam^{-1})	b_{major} (")	b_{minor} (")	b_{PA} (deg)
L-band	33.8	20.4	10.8	5.1	1.1	-3.7
S-band	18.0	10.5	5.9	3.4	0.74	-8.6
C-band	7.95	6.46	4.3	2.5	0.51	-5.9
X-band	4.01	3.20	2.2	0.96	0.22	-5.6

is less visible in the S-band image due to its spectral slope, as well as the more compact beam. In the C-band image, the jetted outflows are visible toward the north and the south of the AGN. A small part of the mini halo is still visible toward the east and west of the AGN. Finally, the X-band image shows the jets at the highest angular resolution. The total flux densities, peak fluxes, rms noise levels, and beam sizes of the final images are summarized in Table 2.2.

To show the maximum resolution attainable with each of the four data sets, images of the target using lower robust parameters are shown in Figure 2.2. This shows that using a different weighting scheme, the jetted outflows can even be resolved in the L band. Comparing our observations to the ATCA observations of Akahori et al. (2020), we find that our VLA observations are able to resolve all components observed with the ATCA: C1 (AGN core), C2, C4, C5 (northern lobe), and C3 and C6 (southern lobe). Akahori et al. (2020) mention that they possibly detect jet precession, as components C3 and C4 (near the AGN), appear to be emitted in a different direction than components C2 and C6 in the northern and southern jets, respectively.

The emission from the AGN appears to be coincident with the BCG, as shown in Figure 2.3. In addition, the L-band emission extends far beyond the optical size of the BCG and the star-forming filaments. The radio emission from the cluster coincides with X-ray emission detected by Chandra (McDonald et al. 2015), as shown in Figure 2.4. To confirm that the jetted outflows detected in our VLA observations are coincident with the cavities previously detected in the ICM, we subtracted a β-model from the X-ray map, and then overlaid the L- and X-band contours on the residuals, as shown in Figure 2.5. Although there is a small subarcsecond uncertainty in the relative alignment between the images, it is clear that the X-ray cavities are inflated by magnetized radio plasma. We find no radio emission coincident with the possible ghost cavities previously marginally detected by McDonald et al. (2015) farther toward the north-east and south-east.

To derive the overall spectral index of the source, we combined measurements of the total flux density of the cluster in our four bands with archival data from Mauch et al. (2003), McDonald et al. (2014), Van Weeren et al. (2014) and Akahori et al. (2020). We assume a 5% uncertainty on our flux density estimates in accordance with Perley & Butler (2017). By fitting a power-law profile through the data, we obtain an overall spectral index of -1.12 ± 0.02, as shown in Figure 2.6. To account for a possible curvature in the spectrum, we fit a second-degree polynomial in log-space through the data, but find the curvature term to be consistent with zero

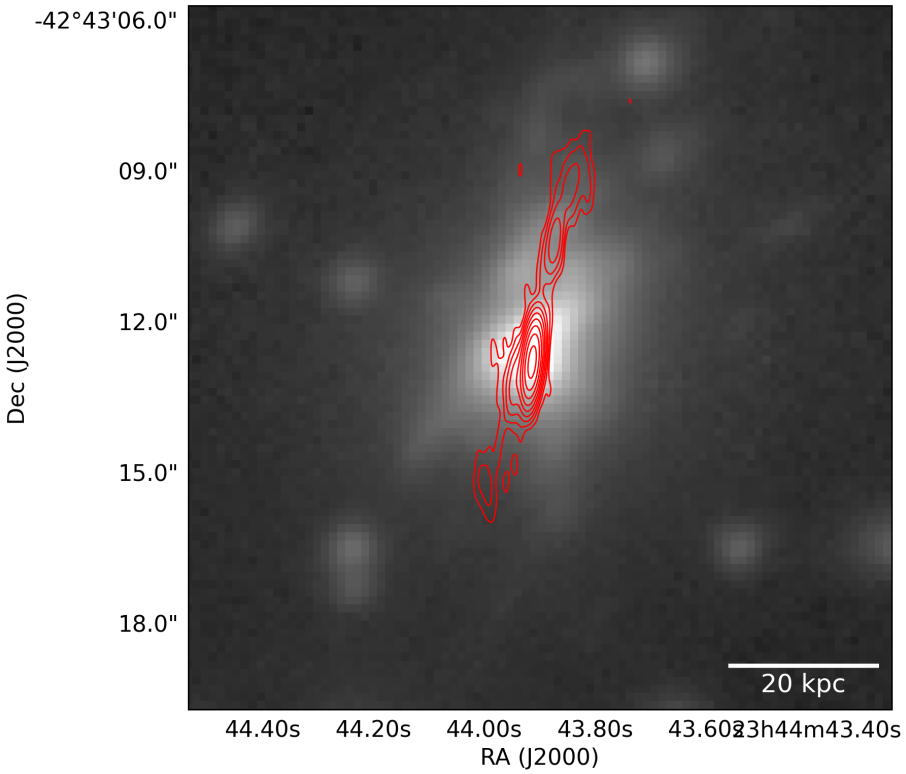

Figure 2.3: Optical r-band image of Phoenix cluster taken with Megacam on the Magellan Clay Telescope (McDonald et al. 2015). The red contours indicate the X-band emission and are drawn at [-1, 1, 2, 4, 8, ...] $\times$ $4\sigma_{\rm rms}$, where $\sigma_{\rm rms} = 2.2$ µJy beam^{-1}.

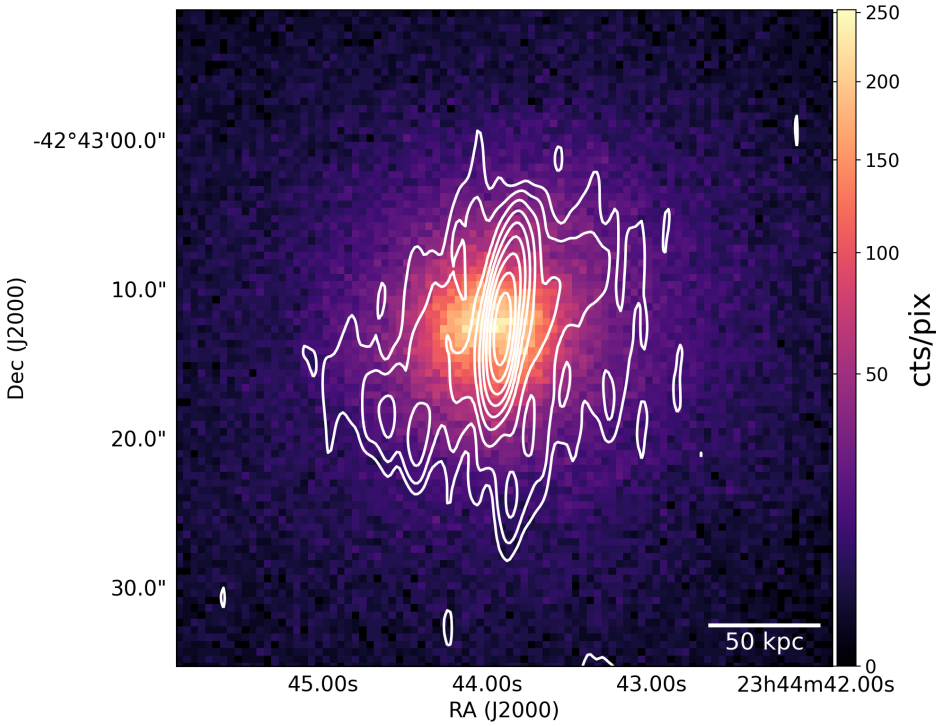

Figure 2.4: X-ray (0.7-2 keV) image by Chandra (McDonald et al. 2015). The white contours indicate the L-band emission as observed with the *Very Large Array* and are drawn at [-1, 1, 2, 4, 8, ...] $\times$ $4\sigma_{\rm rms}$, where $\sigma_{\rm rms} = 10.8$ µJy beam^{-1}.

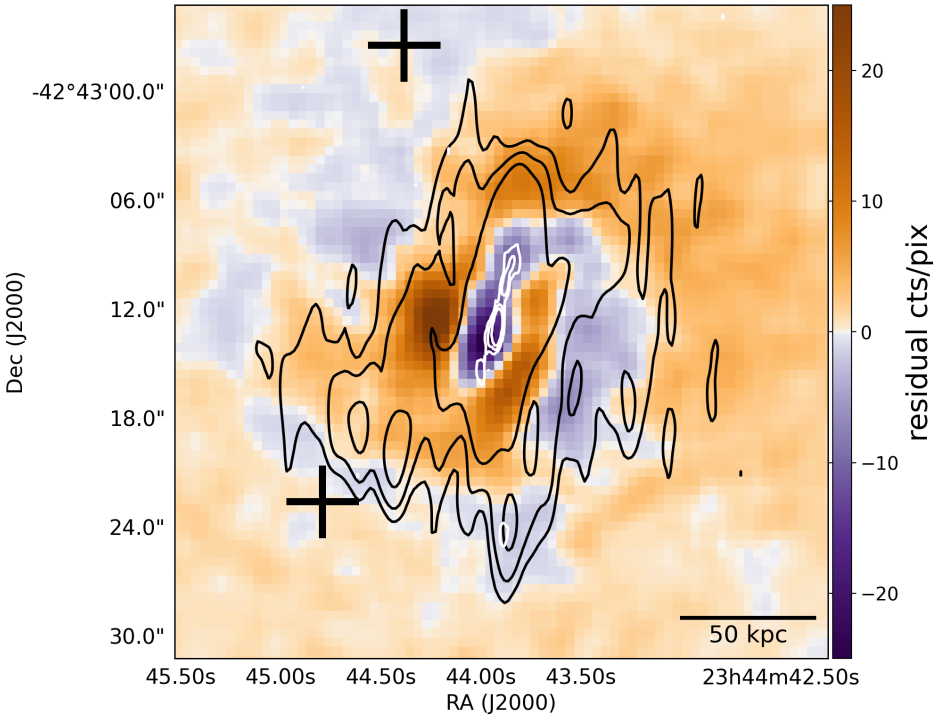

Figure 2.5: Residuals of Chandra X-ray image (McDonald et al. 2015) minus a β-model. The residuals were smoothed by a boxcar function with a scale of three pixels (1.5 arcsec). The white contours indicate the emission in the X band as observed with the VLA and are drawn at [-1, 1, 4, 16] $\times$ $4\sigma_{\rm rms}$, where $\sigma_{\rm rms}$ = 2.2 µJy beam^{-1}. The black contours indicate the emission in the L band as observed with the VLA, and are drawn at [-1, 1, 2, 4] $\times$ $4\sigma_{\rm rms}$, where $\sigma_{\rm rms}$ = 10.8 µJy beam^{-1}. The black pluses indicate the positions of the ghost cavities detected by McDonald et al. (2015).

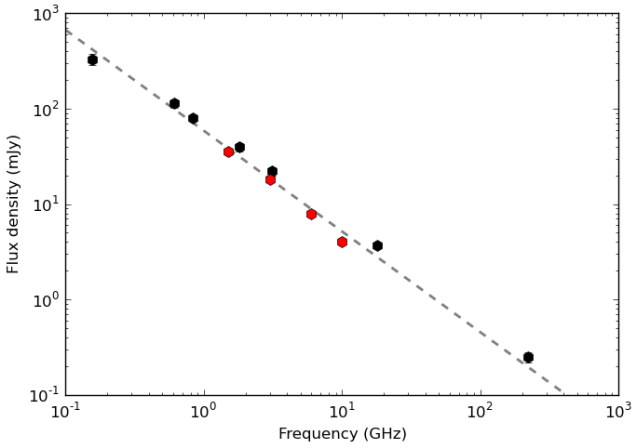

Figure 2.6: Spectral energy distribution of Phoenix cluster. The black dots show data obtained from literature. The red dots show data presented in this work. The best-fit spectral index through the data is -1.12 ± 0.02. A curvature term is included in the fit, but is found to be negligible. The data point at 220 GHz is excluded from the fit as free-free and thermal dust emissions are expected to contribute significantly at this frequency.

within the 95% confidence interval. We excluded the data point at 220 GHz from this fit, as we expect that free-free and thermal dust emissions can significantly contribute to the spectrum at such high frequencies, causing the model of a single power law to break down.

To study the mini halo and the AGN, we needed to separate these two components. By producing a map of the source using only the long baselines, we obtained an image of the AGN and its jets, without contamination from the more extended mini halo. Based on the X-band imaging, we find that the AGN and its jets are more compact than an angular scale of ten arcseconds, which corresponds to a limit on the baseline length of 20 kλ. After having produced an L-band image using only baselines longer than 20 kλ, we find that the remaining flux density of the source is 25.2 mJy within the 3σ contours. Comparing this flux density to the total flux density of 33.8 mJy, we find that there is a discrepancy of 8.6 mJy, which we attribute to the mini halo.

Alternatively, the flux density of the mini halo can be estimated through radial profile fitting by describing both the AGN and the mini halo using circular Gaussians. This enables the flux of the AGN and the mini halo to be spatially disentangled, thereby potentially providing a more accurate measurement of their total flux densities. We produced an L-band image with a Briggs robust parameter of -1 to improve the resolution of the image, and thereby reduced the scale of the central AGN. This image was smoothed to a circular beam of 2.8 arcseconds based on the major axis of the image. Through a least-squares fitting, we obtained separate estimates for the flux density of the AGN and the mini halo.

For the AGN, we find a flux density of 23.6 $\pm$ 2.4 mJy, whereas we find a flux density of 8.5 $\pm$ 0.9 mJy for the mini halo.

Similarly, we can perform a radial fit with all compact emission masked out, as we know that the jetted outflows are only present in the northern and southern directions, which can cause a systematic error. With the L-band map produced using only long baselines, we were able to define a mask of where we expected the source to be dominated by compact structure. Outside of this mask, the mini halo is expected to be the dominant component. We defined this mask as the 3σ region in the 20 kλ L-band map. Using this mask, we were able to fit the source using a single Gaussian profile to represent the mini halo. The estimate obtained with a mask for the flux density of the mini halo is considerably lower, at only 5.9 mJy. As the values obtained from the first two methods agree very well, we adopt a value of 8.5 mJy for the flux density of the mini halo in L band for the rest of this paper.

From the radial fitting process, we can also obtain an estimate for the extent of the mini halo. From the radial fit, we find that it can be described by a Gaussian with a FWHM of 13.8 arcseconds, deconvolved with the beam. At a redshift of $z = 0.597$, this corresponds to a scale of 92 kpc. The maximum observable radius of the mini halo –defined as the radius at which the mini halo reaches the noise level– is 17.8 arseconds, or about 120 kpc. This gives a total diameter of the mini halo of $\sim$240 kpc.

To map the spectral index of the halo, we smoothed both the L-band and the S-band images to a circular beam size of five arcseconds and aligned the images by matching the positions of a nearby point source. To avoid contamination from the AGN and its jets, we masked out the central region using the same mask as with the radial fitting. After calculating the spectral index between the two maps and excluding the masked region, we obtained the spectral index map of the mini halo as shown in Figure 2.7.

The spectral index map of the mini halo shows an annulus with a mean spectral index of $\alpha = -0.95 \pm 0.10$. However, the signal-to-noise ratio is too low to provide insight about any potential gradients or cut-offs in the spectrum as a function of radius. Using this spectral index, we calculated the radio luminosity of the mini halo using

$$P_{1.4\mathrm{GHz}} = 4\pi S_{1.4\mathrm{GHz}} D_L^2 (1+z)^{-\alpha-1}, \tag{2.1}$$

where $S_{1.4\mathrm{GHz}}$ is the flux density at 1.4 GHz and D_L is the luminosity distance to the source, and we find a value of $P_{1.4\mathrm{GHz}} = (13.0 \pm 1.4) \times 10^{24}$ W Hz^{-1}.

To map the spectral index of the AGN and its lobes, we took the high-resolution L-band image, as shown in Figure 2.2, and we smoothed the X-band image to this resolution. Next, we aligned the images based on a nearby point source. By calculating the spectral index between the L band and X band, we obtain the map shown in Figure 2.8.

In this spectral index map, we can resolve both the spectral indices of the two lobes, as well as the spectral index of the AGN. We find that the northern lobe has a spectral index between the L and X bands of -1.35 $\pm$ 0.07, and the southern lobe has a spectral index of -1.30 $\pm$ 0.12. The AGN in the center of the map

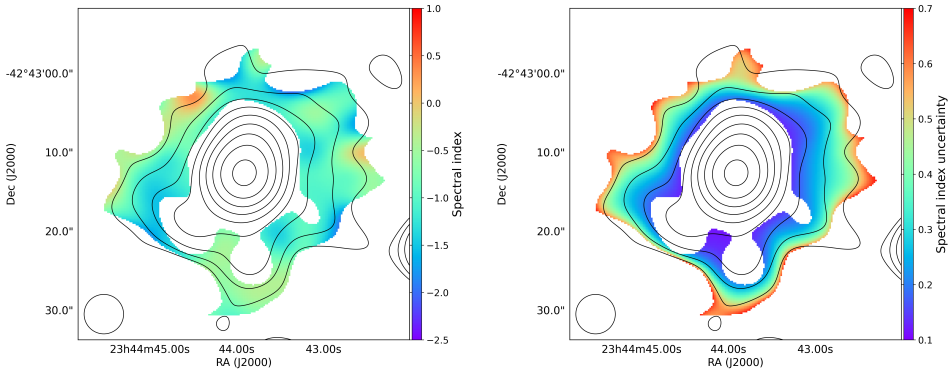

Figure 2.7: *Left:* spectral index map from L- and S-band images. *Right:* corresponding uncertainties of the spectral index map. The contours show the L-band image smoothed to a resolution of five arcseconds and are drawn at [-1, 1, 2, 4, 8, ...] $\times\ 4\sigma_{\rm rms}$, where $\sigma_{\rm rms} = 17.9$ µJy beam^{-1}. The circular beam of five arcseconds is shown in the bottom-left corner.

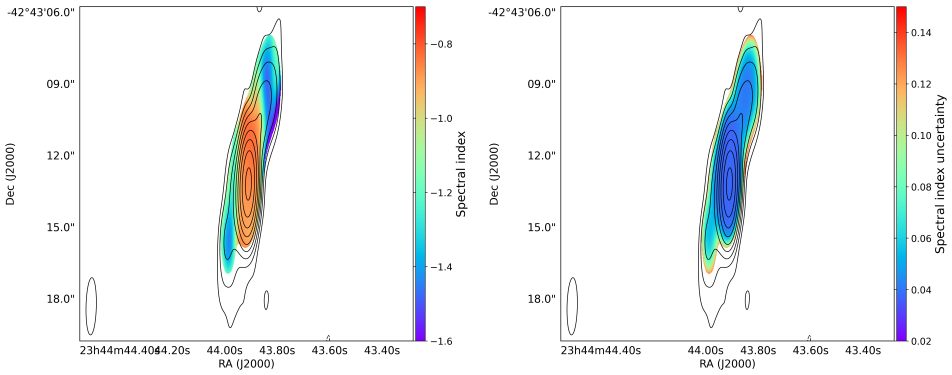

Figure 2.8: *Left:* spectral index map from L- and X-band images. *Right:* corresponding uncertainties of the spectral index map. The contours show the X-band image smoothed to the L-band resolution and they are drawn at [-1, 1, 2, 4, 8, ...] $\times\ 4\sigma_{\rm rms}$, where $\sigma_{\rm rms} = 2.6$ µJy beam^{-1}. The beam is shown in the bottom-left corner.

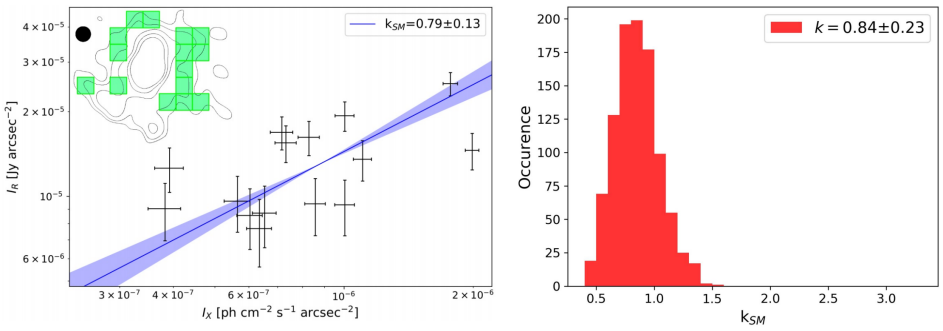

Figure 2.9: Results from Monte Carlo point-to-point analysis. *Left:* an example of an estimate for k using a particular choice for the grid position. The data points and error bars show the estimated radio surface brightness vs. X-ray surface brightness for a given grid cell. The slope of the best-fit power law through these data (blue line) is shown in the legend. The contours in the top-left corner indicate the [3,6,12,24,48] $\times\sigma$ contours of the circularly-smoothed L-band image with a Briggs robust parameter of -1, where $\sigma = 18$ µJy. The beam size is 2.8 arcseconds circular, and is indicated by the solid black circle. *Right:* histogram of all values of k from the Monte Carlo point-to-point analysis. The resulting best estimate for $k_{\rm MC}$ is reported in the legend.

shows a spectral index of -0.86.± 0.04. Due to the alignment of the lobes with the synthesized beam, we do not have the resolution required to check for a spectral gradient along the outflows. By subtracting a point source convolved with the beam from the high-resolution L-band image, we find that the radio lobes have a total flux density of 7.6 ± 0.8 mJy.

Finally, as we have VLA observations in full polarization mode, we checked for polarized emission using RM synthesis. However, we were unable to find a significant amount of polarized emission from the cluster, which is consistent with the results of Akahori et al. (2020).

2.5 Discussion

2.5.1 The origin of the mini halo

Our VLA observations clearly resolve the mini halo and the AGN in the Phoenix cluster. We estimate the mini halo to have a maximum observable deconvolved diameter of about 240 kpc, and a radio luminosity at 1.4 GHz of $P_{1.4\rm GHz} = (13.0 \pm 1.4) \times 10^{24}$ W Hz^{-1}. Our estimate for the size of the mini halo is smaller than that of Van Weeren et al. (2014), who estimated a size in the range of 400-500 kpc using 610 MHz GMRT observations. This may be an indication of spectral steepening in the outer regions of the mini halo, as a detection by the GMRT at 610 MHz and a non-detection by the VLA at 1.5 GHz in this region implies a spectral index steeper than $\alpha = -1.5$, based on the rms noise levels in both maps. However, we do not see a trend in our spectral index maps to suggest such

a spectral steepening. In addition, the GMRT data suffers from a relatively poor angular resolution and sensitivity compared to the VLA, so we cannot make any definite claims on the spectrum of the mini halo in the outer regions. Our reported value for the radio luminosity at 1.4 GHz is consistent with previous estimates by Van Weeren et al. (2014) and Raja et al. (2020), who calculated values of $P_{1.4\mathrm{GHz}} = (10.4 \pm 3.5) \times 10^{24}\mathrm{WHz}^{-1}$ and $P_{1.4\mathrm{GHz}} = (14.38 \pm 1.80) \times 10^{24}\mathrm{WHz}^{-1}$, respectively.

We mapped the spectral index of the mini halo and derive an integrated spectral index between the L and S bands of -0.95 ± 0.10, which is consistent with the spectral index of -0.98 ± 0.16 as derived by Raja et al. (2020) between 610 MHz and 1.5 GHz. We were unable to find evidence for a radial gradient in the spectral index map due to the low signal-to-noise ratio.

Further insight into the origin of the diffuse emission can be provided by the spatial correlation between the radio (I_R) and X-ray (I_X) surface brightnesses. This correlation is expected because the relativistic electron population, and hence the radio emission, are predicted to be linked to the thermal plasma in both hadronic and re-acceleration models. The I_R-I_X correlation allows us to constrain the distribution of the nonthermal ICM components with respect to the thermal plasma and thereby investigate the origin of the radio emission (e.g., Brunetti & Jones 2014; Ignesti et al. 2020).

We used the Monte Carlo point-to-point analysis presented in Ignesti et al. (2020) to evaluate the I_R-I_X correlation for the Phoenix cluster. We use a circularly smoothed image of the Phoenix cluster in the L band with a Briggs robust parameter of -1 to improve the resolution of the map, and thereby reduce the area affected by AGN-related emission while simultaneously increasing the amount of samples of mini-halo emission. The X-ray surface brightness is obtained from archival Chandra observations. The surface brightnesses I_R and I_X have been sampled with 1000 randomly-generated meshes. For the cells in the mini-halo region, values of I_R and I_X are measured and fit with a power-law relation, $I_R \propto I_X^k$, using the BCES algorithm (Akritas & Bershady 1996). We present in Figure 2.9 both the result of the analysis performed on a single grid (left panel) and the final result of the MC routine (right panel). We measured a sub-linear scaling index, k, of 0.84 ± 0.23, which indicates that the radio emission likely declines slower than the X-ray emission. This result is interestingly more similar to what is observed for giant radio halos –which often feature sub-linear indices k in the range of 0.5 to 1.0 (Govoni et al. 2001; Feretti et al. 2001; Giacintucci et al. 2005; Hoang et al. 2019; Xie et al. 2020)– than to mini halos, which generally feature a super-linear scaling with indices k in the range of 1.1 to 1.3 (Ignesti et al. 2020). Such a flat index, k, indicates that the X-ray emission is more peaked than the radio emission, which is in agreement with the exceptionally luminous cool core of this cluster. Therefore, it suggests that the distribution of nonthermal components does not strongly depend on the properties of the cool core.

On the basis of these results, we can explore the scenario of purely hadronic origin of relativistic electrons. We followed the approach presented in Ignesti et al. (2020) to infer the ICM magnetic field to constrain the physical boundaries of the hadronic model for the Phoenix cluster. We used the thermodynamic profiles from

McDonald et al. (2015) to compute the ICM electron density and temperature. From these, we numerically calculated the X-ray emissivity. Assuming a hadronic model, we can compare these to the radio emissivity expected in a pure hadronic model (e.g., Brunetti et al. 2012) to constrain the magnetic field configurations that are consistent with our value of the index k. We assume a magnetic field profile of the form

$$B(r) = B_0 \left(\frac{n(r)}{n_0} \right)^{\eta}, \tag{2.2}$$

where B_0 and n_0 are the central values of the magnetic field strength and the thermal ICM number density, respectively, and the index η determines the scaling relation between the magnetic field and the ICM density. The constraints we derive on the magnetic field configuration are shown in Figure 2.10. We find that for typical values of the central magnetic field strength (10-20 µG; Carilli & Taylor 2002), we require the index η to be 0.2-0.3, indicating that the ICM density is much more peaked than the magnetic field strength. Similarly, for a typical value of $\eta = 0.5$, we require the central magnetic field strength to be at least 50 µG, which is far higher than commonly observed.

To provide context to these estimates of the magnetic field configuration from the point-to-point analysis, we also calculate the equipartition magnetic field. Under the assumption that the magnetic field and the cosmic ray particles evolve over similar timescales, they are expected to be coupled. This coupling is supposed to lead to an equilibrium between the energy densities of the cosmic ray particles and the magnetic field (Govoni & Feretti 2004; Beck & Krause 2005). For the classical equipartition magnetic field, we obtain a field strength of 3.4 µGauss. For the revised equipartition magnetic field, we obtain a field strength of 5.5 µGauss using a commonly adopted value of $\gamma_{\rm min} = 100$ for the low-energy cut-off of the cosmic ray particle energy distribution. This shows that the equipartition magnetic field strength is much lower than the magnetic field strength predicted by a hadronic model.

In addition, we can test predictions from hadronic models on the spectral index of the mini halo. According to a hadronic model, the radio-emitting electrons are injected by collisions between cosmic-ray protons from the AGN and thermal protons in the ICM. This implies that the synchrotron spectral index α is directly proportional to the cosmic ray proton injection spectral index δ as $\alpha \approx \delta/2$ (e.g., Blasi & Colafrancesco 1999; Pfrommer & Enßlin 2004; Brunetti et al. 2017). Therefore, our spectral index of $\alpha = -0.95 \pm 0.10$ requires a cosmic ray proton injection spectral index of $\delta = -1.90 \pm 0.20$, but such a flat distribution is only marginally consistent with the generally observed values of δ in the range of -2.1 to -2.4 (e.g., Völk et al. 1996; Blasi & Colafrancesco 1999; Schlickeiser 2002; Enßlin 2003; Pinzke & Pfrommer 2010).

As we find that both the magnetic field configurations obtained by assuming a hadronic model and the relatively flat spectral index of the mini halo are inconsistent with the values generally reported in literature, we conclude that our results disfavor a pure hadronic origin of the radio emission, although we cannot exclude that proton-proton collisions played a role in the origin of seed electrons for

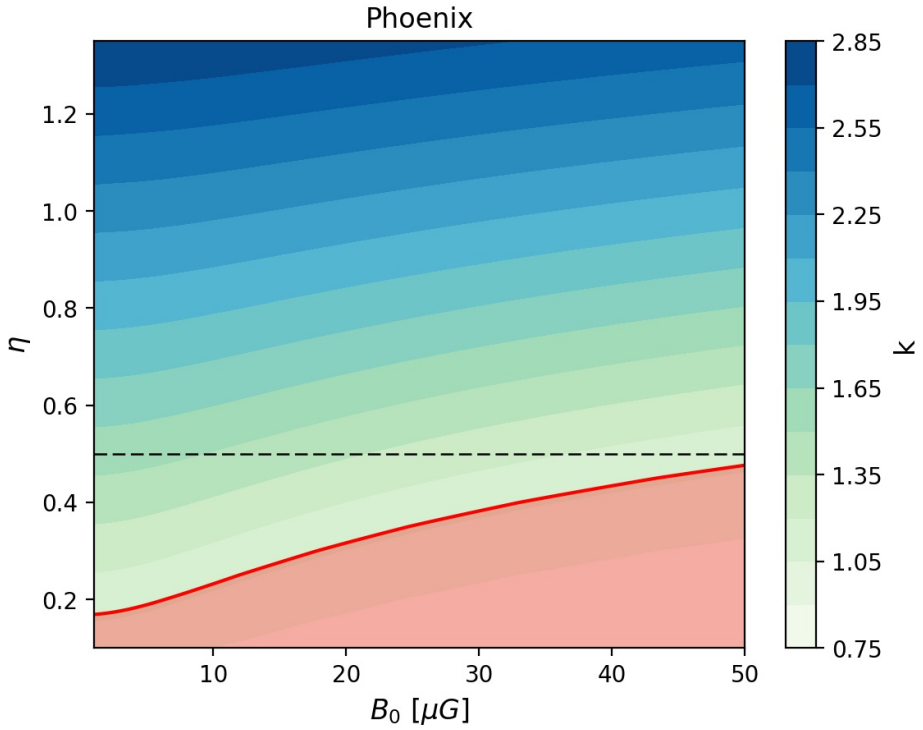

Figure 2.10: Index k for combinations of magnetic field strength and the index η. The horizontal dashed line at η=0.5 indicates the equilibrium configuration between thermal and nonthermal energy density. The red region indicates the parameter space consistent with values of k that we obtained using the Monte Carlo point-to-point analysis.

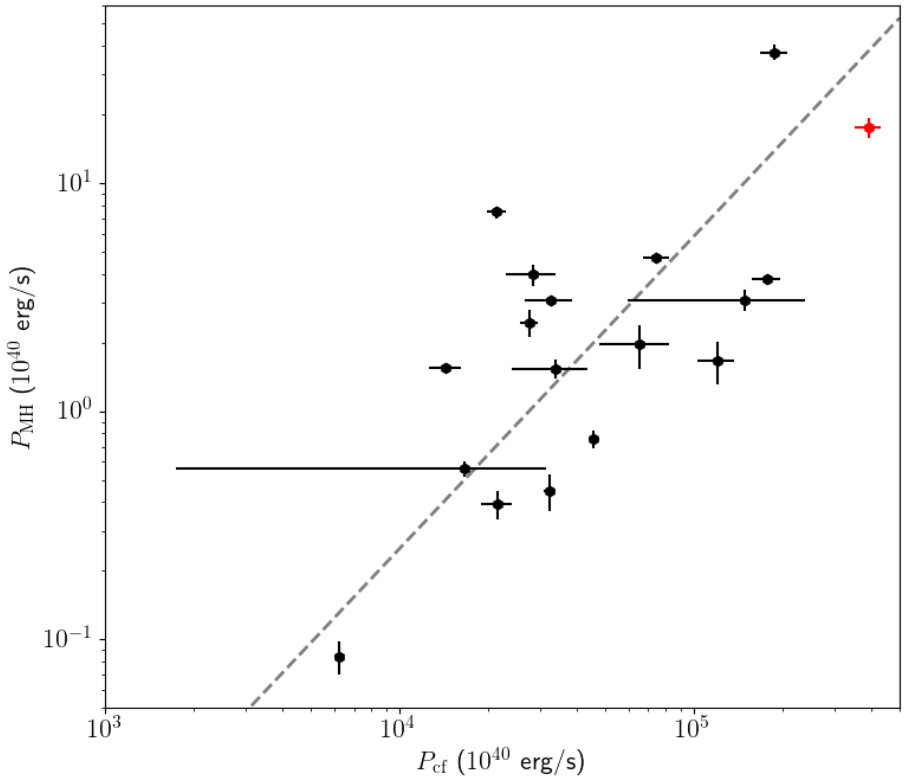

Figure 2.11: Cooling flow power versus mini-halo radio luminosity at 1.4 GHz for the sample of mini halos from Giacintucci et al. (2019). The red data point indicates the Phoenix cluster. The dashed grey line indicates the best power-law fit through the data and is given by $\log P_{\rm MH}[10^{40}{\rm erg/s}] = (1.37 \pm 0.17) \log P_{\rm cf}[10^{40}{\rm erg/s}] - (6.07 \pm 0.79)$. The integrated mini-halo luminosities are from Giacintucci et al. (2019) and this work. Values of the cooling rates and ICM temperatures are from Arnaud et al. (1987), Churazov et al. (2003), Gitti & Schindler (2004), Böhringer et al. (2005), Covone et al. (2006), Leccardi & Molendi (2008), Bravi et al. (2015), McDonald et al. (2015), Main et al. (2016), Werner et al. (2016) and McDonald et al. (2018).

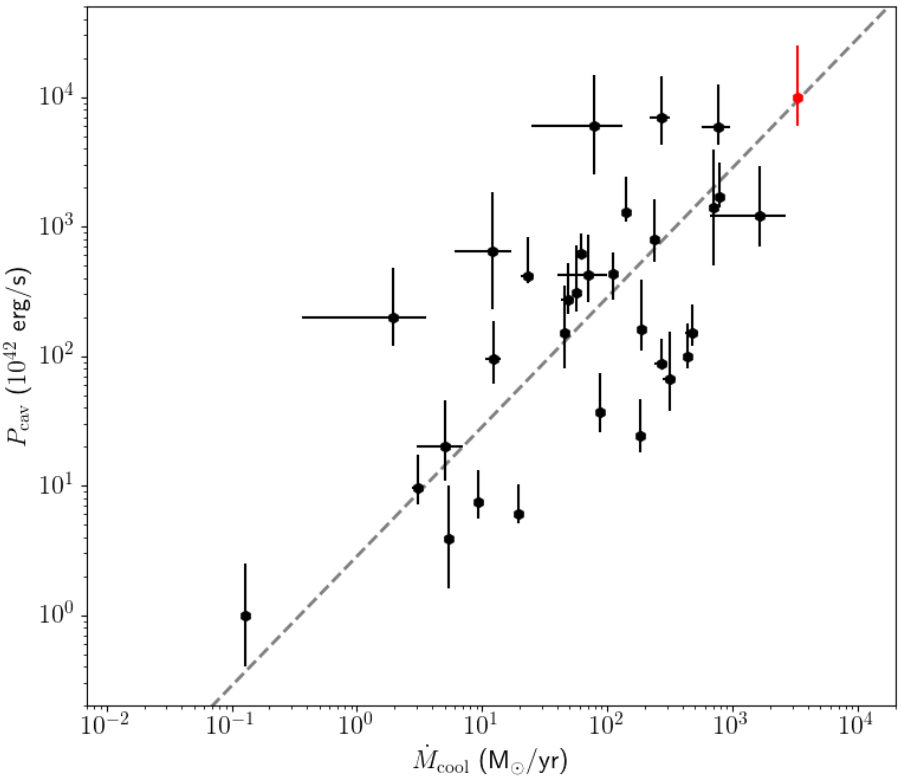

Figure 2.12: ICM cooling rate $\dot{M}_{\rm cool}$ vs. cavity power $P_{\rm cav}$ for the sample of clusters from Rafferty et al. (2006). The red data point indicates the Phoenix cluster. The gray dashed line indicates the best power-law fit through the data and is given by $\log P_{\rm cav}[10^{42}{\rm erg/s}] = (1.00 \pm 0.10) \log \dot{M}_{\rm cool}[{\rm M}_\odot/{\rm yr}] + (0.45 \pm 0.24)$. All black data points are from Rafferty et al. (2006) and McDonald et al. (2018), and the Phoenix cluster data are from McDonald et al. (2015, 2019).

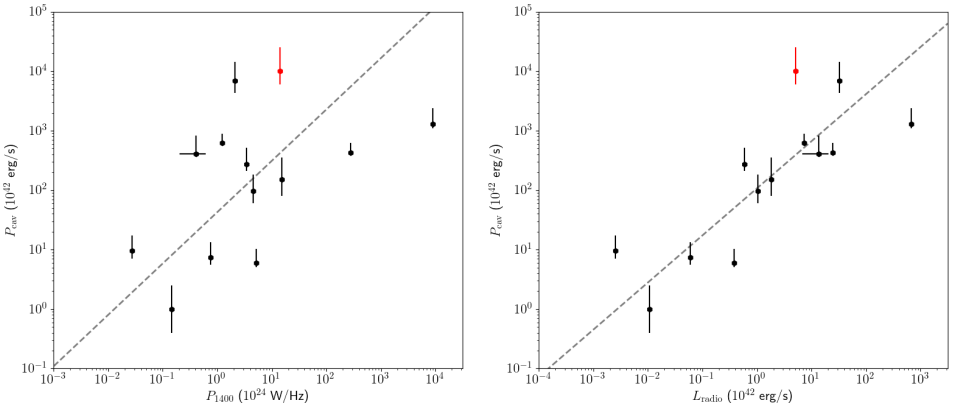

Figure 2.13: *Left:* radio luminosity of the lobes at 1.4 GHz vs. cavity power for Phoenix cluster (red) and the Bîrzan et al. (2008) sample of mini halos (black). The dashed line shows the best power-law fit through the data and is given by $\log P_{\rm cav}[10^{42}{\rm erg/s}] = (0.86 \pm 0.20) \log P_{1400}[10^{24}{\rm W/Hz}] + (1.63 \pm 0.29)$. *Right:* bolometric radio luminosities of the lobes between 10 MHz and 10 GHz for the same sample. The dashed line shows the best power-law fit through the data and is given by $\log P_{\rm cav}[10^{42}{\rm erg/s}] = (0.79 \pm 0.15) \log L_{\rm radio}[10^{42}{\rm erg/s}] + (2.03 \pm 0.19)$. Phoenix cluster data are from McDonald et al. (2019) and this work, and data for the other clusters are from Bîrzan et al. (2008).

the re-acceleration. Therefore, a turbulent re-acceleration model is the preferred model to explain the origin of the mini halo in the Phoenix cluster. However, the question remains as to what causes this turbulence.

Mazzotta & Giacintucci (2008) observed a correlation between the mini-halo emission and the spiral-shaped cold fronts produced by sloshing of the gas in the cool core (Markevitch et al. 2003; Ascasibar & Markevitch 2006). Magneto-hydrodynamic simulations by ZuHone et al. (2011a,b, 2013, 2015) show that this sloshing can induce turbulence and amplify the magnetic fields required to re-accelerate thermal electrons to relativistic speeds. In addition, their simulations predict luminosities and spectral indices that are in agreement with observations. Recent research by Richard-Laferrière et al. (2020) suggests that in addition to sloshing, AGN feedback may also contribute significantly to the amount of turbulence. For the Phoenix cluster, we find that the extent of the mini halo matches with the extent of the sloshing pattern in the ICM observed using X-ray data (see Figure 2.5). Toward the south of the AGN, the mini halo appears to be confined to the overdense region in the ICM, whereas toward the west it appears to be confined to the underdense region in the ICM.

On the other hand, Gitti et al. (2002, 2004, 2007) suggested that the turbulence in the core can be induced by the strong cooling flow accreting onto the cool core. If so, a direct relation is expected between the mini-halo cooling flow power $P_{\rm cf}$ and the integrated mini-halo radio power $\nu P_{\rm MH}$. The cooling flow power is calculated as $P_{\rm cf} = \dot{M}kT/\mu m_{\rm H}$, where $\dot{M}$ is the mass accretion rate, k is Boltzmann's constant, T is the temperature of the ICM, μ is the mean molecular weight, and $m_{\rm H}$ is the mass of a hydrogen atom. We plotted the correlation between these two properties

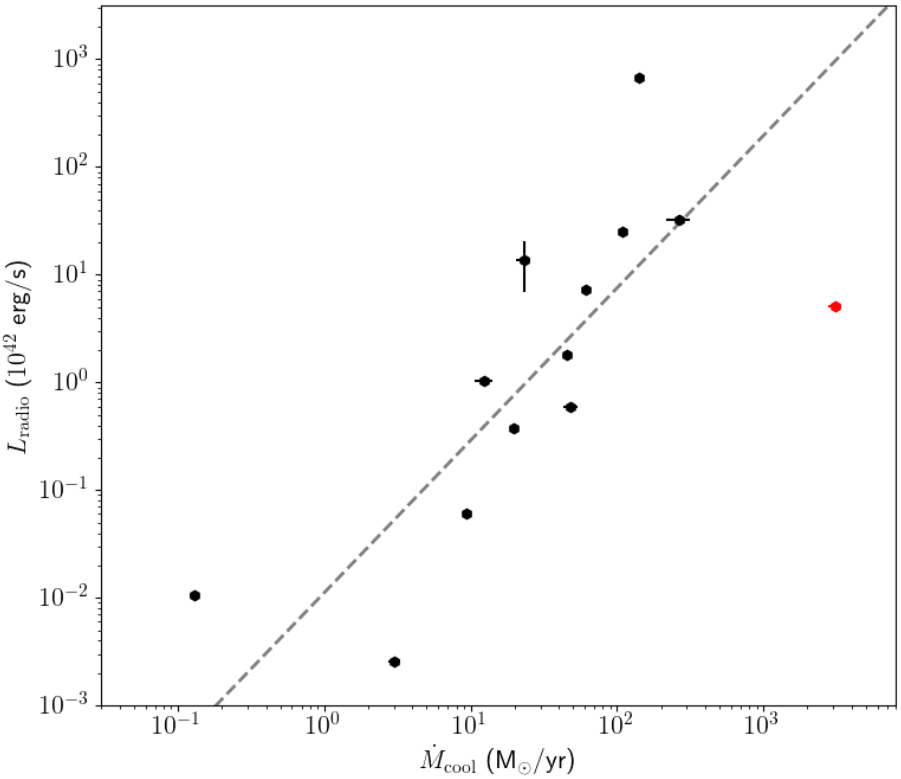

Figure 2.14: ICM cooling rate $\dot{M}_{\rm cool}$ vs. bolometric radio luminosity of lobes between 10 MHz and 10 GHz. The red data point indicates the Phoenix cluster, and the black data points indicate the sample of Bîrzan et al. (2008). The dashed line shows the best power-law fit through the data and is given by $\log L_{\rm radio}[10^{42}{\rm erg/s}] = (1.41 \pm 0.35) \log \dot{M}_{\rm cool}[{\rm M}_\odot/{\rm yr}] - (1.95 \pm 0.53)$. Phoenix cluster data are from McDonald et al. (2019) and this work, and data for the other clusters are from Bîrzan et al. (2008); McDonald et al. (2019).

based on the Giacintucci et al. (2019) sample of mini halos, as shown in Figure 2.11. As previously verified by Doria et al. (2012) and Bravi et al. (2015) using different samples, this correlation between the cooling flow power and the integrated radio power of the mini halo is indeed present. However, the relatively large intrinsic scatter suggests that this correlation may not indicate a causal connection between the cooling flow rate and turbulence in the cool core. Instead, this correlation could, for example, emerge due to dependence on a third parameter.

Therefore, we conclude that the turbulent re-acceleration model powered by sloshing is the prime candidate to explain the origin of the mini halo. Based on the close similarities between the mini-halo emission region and the sloshing region, and the agreement between the observed spectral index and theoretical predictions, we find sloshing to be the main source of turbulence in the ICM, although we do not exclude that the exceptionally strong cooling flow in the Phoenix cluster may have partly contributed to the turbulence.

2.5.2 The extreme feedback in the Phoenix cluster

Two of the main open questions about the feedback process in the Phoenix cluster remain: why does this cluster feature such a strong cooling flow and why are the radio and X-ray observations so disconnected. According to the explanation recently proposed by McDonald et al. (2018), the strong cooling flow could be a consequence of the way the most massive clusters (such as the Phoenix cluster) are formed. As lighter clusters merge and form more massive clusters, their low-entropy gas content merge relatively quickly compared to their central galaxies. This delayed merging of the central galaxies leads to the most massive clusters having relatively underweight supermassive black holes powering their AGNs, as they generally have a rich and recent merging history. For supermassive black holes, it has been observed that the mechanical power levels off as the accretion rate reaches a few percent of the Eddington rate (Russell et al. 2013). This is in contrast to the radiative power of the AGN, which continues to increase with the accretion rate. In the context of a galaxy cluster, this means that if the central supermassive black hole is underweight, the same accretion rate of the AGN is more likely to reach this saturation point and result in the AGN being unable to compensate for the cooling flow with mechanical feedback. Verifying this explanation would require precise measurements of the black hole masses, which we can not derive from our radio observations. Therefore, definitively answering this open question is not the goal of this work. However, we can investigate if our observations are consistent with this explanation.

According to this explanation, the overall feedback process in the Phoenix cluster is not abnormal. Instead, the Phoenix cluster should simply be in the tail of the distribution. To see in which aspects the Phoenix cluster is an outlier to the general population, we looked into its cavity power and ICM cooling rate. The cavity power $P_{\rm cav}$ of a cluster can be estimated by dividing the total enthalpy $E_{\rm cav}$ of the cavities by the buoyant rise time. Here, the total enthalpy $E_{\rm cav}$ can be calculated as $E_{\rm cav} = 4PV$, where P is the total pressure of the ICM at the position of the cavities and V is the volume of the cavities. The buoyant rise

time is the time required for the cavities to move from the AGN to their present position under the assumption that they rise through the ICM buoyantly. The ICM cooling rate within a particular radius indicates how much mass in the ICM cools down per year due to the emission of thermal bremsstrahlung, and it can be calculated as the ICM mass enclosed within the given radius divided by the cooling time. We plotted the cavity power versus the ICM cooling rate for the Phoenix cluster and the sample of clusters from Rafferty et al. (2006), as shown in Figure 2.12. Here we find that the Phoenix cluster is the most extreme cluster in the sample, both in terms of the cooling flow rate and the cavity power. However, the Phoenix cluster is consistent with the observed correlation. Similarly, we plotted the radio luminosity of the jetted outflows at 1.4 GHz, as well as the bolometric radio luminosity, against the cavity power, for a sample of clusters, as shown in Figure 2.13. This is where the Phoenix cluster does appear to be an outlier, as the cavity power is too high for both the bolometric radio luminosity of the lobes and their radio luminosity at 1.4 GHz. This is amplified if we plot the cooling flow rate against the bolometric radio luminosity of the lobes, as shown in Figure 2.14. In this comparison, the Phoenix cluster is a strong outlier in the correlation. For its cooling flow rate, the radio lobes in the Phoenix cluster are far too faint.

We observe a disconnection between the radio- and the X-ray properties of the Phoenix cluster. In the radio regime, the AGN in the Phoenix cluster appears to be relatively modest, whereas in the X-ray regime, both the AGN and the cooling flow are among the strongest of all known clusters. We suspect that this difference between the radio and the X-ray may be caused by strong time variability of the AGN on Myr timescales. In our radio observations, both the northern and southern lobes appear to be detached from the AGN, and this feature is also visible in the ATCA observations presented by Akahori et al. (2020). In addition, we find that the central AGN is not a perfect point source, but it is elongated toward the northwest and southeast, indicating that new outflows are being detected. Outburst power has been observed to vary from factors of several in Hydra A (Wise et al. 2007) to two orders of magnitude in MS0735 (Vantyghem et al. 2014) over timescales of tens of Myr. This observed variability has been corroborated by numerical simulations (e.g., Li et al. 2015; Prasad et al. 2015), providing an explanation for the lobe structure in the Phoenix cluster. It is possible that the sloshing in the ICM contributes in part to this AGN variability by displacing the accretion material of the AGN, similar to as observed in A2495 by Pasini et al. (2019). However, whereas the BCG in A2495 appears to be oscillating back and forth through the cool core, the BCG in the Phoenix cluster is stationary at the center of the cool core. This means that sloshing can only affect the AGN activity if it inhibits the cooling flow. Detailed simulations by Zuhone et al. (2010) suggest that sloshing mainly introduces variability in the cooling flow on timescales of 1 Gyr or more. These timescales are too long to explain the AGN variability in the Phoenix cluster, so we consider it to be unlikely that sloshing plays a major role. In this scenario, the lack of radio luminosity would be caused by a break in the AGN activity, as the only contribution to the lobe radio luminosity is caused by a relatively short and old outburst. This break in the AGN activity would not necessarily affect the currently observed cavity power, as the cavities require

time to expand, and they are therefore more dependent on a later stage of an outburst. However, the current volume of the cavities will not be sustainable due to this AGN variability. As the break in the outflows reaches the cavities, they will deflate, resulting in the average cavity power likely being lower than the presently observed value.

Finally, the relatively low amount of jet precession observed in the Phoenix cluster by Akahori et al. (2020) and our X-band observations likely also contributes to the low ICM re-heating efficiency of the mechanical feedback, as the energy from the AGN is not distributed isotropically, but rather predominantly in the direction of the jets. The explanation by McDonald et al. (2018) combined with time variability of the AGN activity and a low jet precession angle may resolve some of the remaining open questions on the AGN feedback in the Phoenix cluster, although a more quantitative investigation would be required to confirm the validity of this model.

2.6 Conclusions

In this paper, we present new *Karl G. Jansky Very Large Array* observations, enabling the radio lobes of the AGN and the mini halo in the Phoenix cluster to be studied in detail at frequencies from 1 to 12 GHz. In particular, our observations resolve the radio lobes of the AGN in all four frequency bands, and the mini halo can be detected in both our L and S bands. Using these multifrequency observations, we studied the remarkable feedback scenario in the Phoenix cluster and the origin of its mini halo.

We find that the total flux density of the source at 1.5 GHz is 33.8 ± 1.7 mJy, with an overall spectral index of -1.12 ± 0.02. Using our L- and S-band observations, we find that the mini halo has an average spectral index of -0.95 ± 0.10. By subtracting compact emission and through radial profile fitting, we find that the mini halo has a total flux density at 1.5 GHz of 8.5 ± 0.9 mJy, which corresponds to a radio luminosity at 1.4 GHz of $(13.0 \pm 1.4) \times 10^{24}$ W Hz^{-1}. In addition, we find that the mini halo has a maximum observable radius in the L band of 240 kpc. At 1.5 GHz, the radio lobes show a total flux density of 7.6 ± 0.8 mJy, and spectral indices with respect to 10 GHz of -1.35 ± 0.07 (northern lobe) and -1.30 ± 0.12 (southern lobe).

Due to the relatively flat spectral index of the mini halo, the low index k, and the extreme magnetic field configuration we obtain by assuming a hadronic model, we conclude that our results disfavor a pure hadronic origin of the mini halo. On the contrary, we confirm the correlation between the cooling flow power and the radio luminosity of the mini halo with respect to other clusters. Also, we observe the sloshing pattern in the ICM to match with the extent of the mini halo at radio frequencies, and we find our integrated spectral index of the mini halo to be consistent with numerical predictions for a turbulent re-acceleration model. For these reasons, we conclude that a turbulent re-acceleration model is the preferred model to explain the origin of the mini halo, and in particular we favor sloshing in the cool-core as an explanation for the turbulence.

By measuring the flux density of the radio lobes in the L band for the first time, the mechanical feedback in the Phoenix cluster has been studied from a radio perspective. We observe a disconnection between the X-ray and radio properties of the Phoenix cluster: the cavity power and cooling flow rate are both among the most extreme ever measured, whereas the bolometric radio luminosity of the lobes is relatively modest. We find that the feedback in the Phoenix cluster is overall consistent with the proposed explanation by McDonald et al. (2018), which states that the strong cooling rate and inefficient feedback are characteristic of more massive clusters. Strong time variability of the AGN activity on Myr timescales may explain the disconnection between the radio and the X-ray properties of the system. Finally, a small amount of jet precession likely also contributes to the low ICM re-heating efficiency of the AGN feedback.

For future research, it would be valuable to obtain more high-resolution radio observations of a sample of mini halos to further test the correlation between the mini-halo emission and the sloshing pattern in the ICM, as this could provide very strong evidence for the turbulent re-acceleration model, and current results look promising. In addition, low-frequency observations may test whether the sloshing of the ICM produces more extended, ultra-steep spectrum emission beyond the cold fronts, as observed in the cases of PSZ1G139.61+24 and RXJ1720.1+2638 by Savini et al. (2018, 2019).

Acknowledgements

We would like to thank the anonymous referee for useful comments. RT and RJvW acknowledge support from the ERC Starting Grant ClusterWeb 804208. Support for this work was provided to MM by NASA through Chandra Award Number GO7-18124 issued by the Chandra X-ray Observatory Center, which is operated by the Smithsonian Astrophysical Observatory for and on behalf of the National Aeronautics Space Administration under contract NAS8-03060.

3

Origin of the ring structures in Hercules A

Sub-arcsecond 144 MHz to 7 GHz observations

Roland Timmerman, Reinout J. van Weeren, Joseph R. Callingham, William D. Cotton, Richard A. Perley, Leah K. Morabito, Nectaria A. B. Gizani, Alan H. Bridle, Christopher P. O'Dea, Stefi A. Baum, Grant R. Tremblay, Preeti Kharb, Namir E. Kassim, Huub J. A. Röttgering, Andrea Botteon, Frits Sweijen, Cyril Tasse, Marcus Brüggen, Javier Moldon, Timothy Shimwell and Gianfranco Brunetti,

Published in Astronomy & Astrophysics, February 2022, volume 658, A5.

Abstract

The prominent radio source Hercules A features complex structures in its radio lobes. Although it is one of the most comprehensively studied sources in the radio sky, the origin of the ring structures in the Hercules A radio lobes remains an open question. We present the first sub-arcsecond angular resolution images at low frequencies (<300 MHz) of Hercules A, made with the International LOFAR Telescope. With the addition of data from the Karl G. Jansky Very Large Array, we mapped the structure of the lobes from 144 MHz to 7 GHz. We explore the origin of the rings within the lobes of Hercules A, and test whether their properties are best described by a shock model, where shock waves are produced by the jet propagating in the radio lobe, or by an inner-lobe model, where the rings are formed by decelerated jetted plasma. From spectral index mapping our large frequency coverage reveals that the curvature of the different ring spectra increases with distance away from the central active galactic nucleus. We demonstrate that the spectral shape of the rings is consistent with synchrotron aging, which speaks in favor of an inner-lobe model where the rings are formed from the deposition of material from past periods of intermittent core activity.

3.1 Introduction

The origin of the three bright rings in the lobes of the notable radio source Hercules A (Bolton 1948) has remained unclear since their identification by Dreher & Feigelson (1984). Understanding the formation of such rings in the radio lobes of active galactic nuclei (AGN) provides insight into the dynamics of the relativistic jets, the role of shock waves, and particle acceleration in the lobes of radio AGN. Hercules A is associated with a central dominant (cD) galaxy located in the center of a galaxy cluster at a redshift of $z = 0.154$ (Greenstein 1962), and is known for its extreme brightness and large angular scale. Hercules A spans approximately 190 by 60 arcseconds on the sky (530 by 170 kpc), and has a flux density of roughly 45 Jy at 1.4 GHz, enabling detailed studies of the structure of the entire source, from the freshly emitted jets to the old diffuse plasma in the lobes. Therefore, the source is used as a standard to assess the physics of fainter lobed AGN.

Hercules A displays complex structures in its lobes that have been difficult to interpret relative to the standard Fanaroff-Riley (FR) I and II schemes (Fanaroff & Riley 1974; Meier et al. 1991). The source has two bright radio lobes; however, the characteristic hotspots of FR II-type radio galaxies are absent. Similarly, while Hercules A is jet-dominated, the lobes feature hard outer edges instead of fading away into the intracluster medium (ICM), as is typical for an FR I-type source. For these reasons, Hercules A is generally categorized as an intermediate FR I/II source (e.g., Meier et al. 1991; Sadun & Morrison 2002; Saxton et al. 2002; Gizani & Leahy 2003). The eastern lobe is dominated by a bright jet from the AGN that slowly diffuses into the lobe, while the western lobe mainly shows a very distinct series of three rings (Dreher & Feigelson 1984; Mason et al. 1988) at projected distances of between 55 kpc and 230 kpc from the host galaxy. The jets from the AGN produce Alfvénic perturbations that cross the relativistic plasma of the lobes and induce brightness fluctuations. Recent investigations by Gizani & Leahy (1999, 2003, 2004) used both radio observations from the Very Large Array (VLA) and X-ray observations from the Röntgensatellit (ROSAT) to study Hercules A. They concluded, based on the observed rotation measure features and an analytical model for the magnetic field strength, that the eastern jet is orientated towards us while the western jet is receding from us at an inclination angle of 50° relative to the line of sight. In addition, they suggested that the apparent absence of a jet structure in the western lobe could be due to Doppler dimming, which could be as strong as a factor of ~ 20 (Gizani & Leahy 2003). Subsequent research by Gizani et al. (2005) at 74 MHz and 325 MHz using the VLA–Pie Town link (Lane et al. 2005) found that the spectral differences between the jets and the lobes at these low frequencies are smaller than those observed at higher frequencies (Gizani & Leahy 2003). Such spectral differences imply the presence of regions of various ages, thereby supporting the multiple outbursts interpretation. Unfortunately, the limited angular resolution of the VLA–Pie Town link (~ 10 arcseconds at 74 MHz) did not permit a detailed investigation of the rings.

Despite the many studies focused on understanding the structure of Hercules A, a few key features of the lobes remain a mystery. Of particular interest for this paper is the origin of the rings present in the western lobe. Two models have

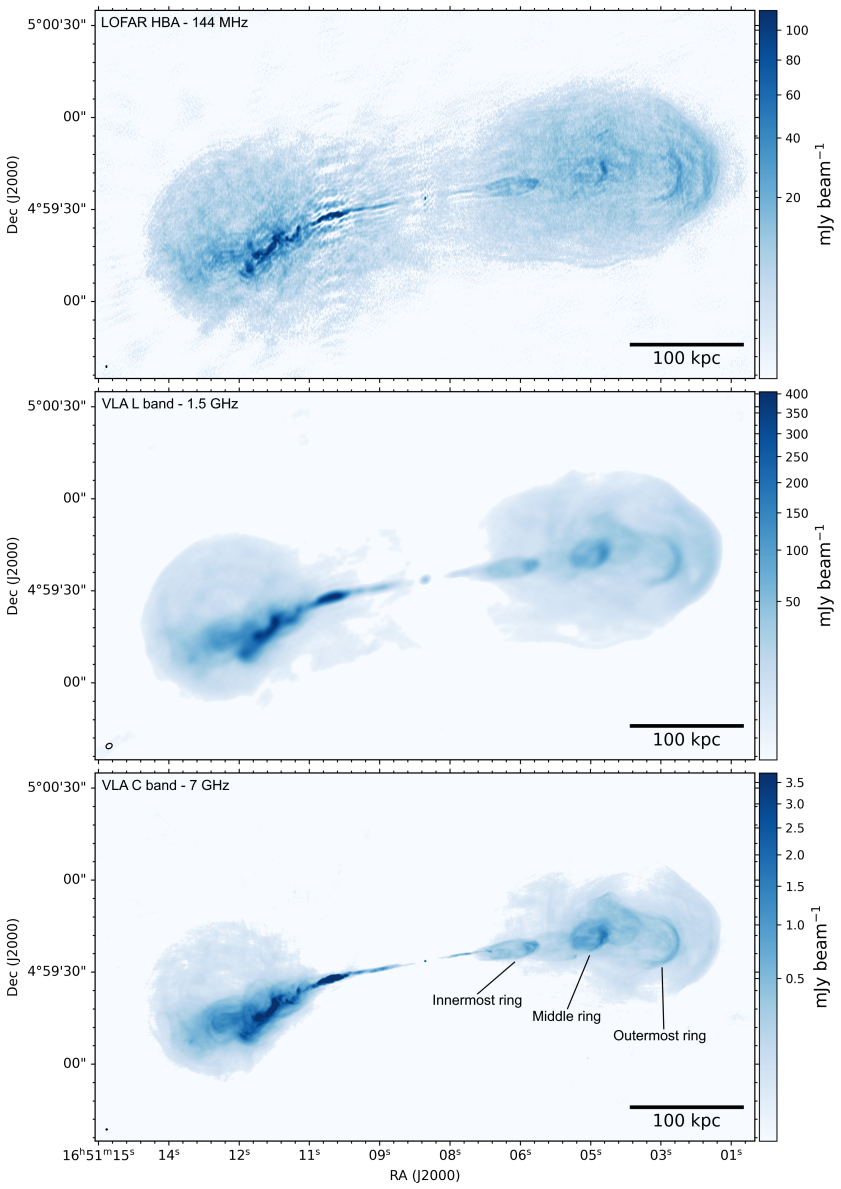

Figure 3.1: Radio images of Hercules A constructed from the LOFAR HBA (144 MHz, top panel), the VLA L band (1.5 GHz, middle panel), and VLA C band (7 GHz, bottom panel). The scale bar in the bottom right corner of each panel measures 100 kpc at the redshift of Hercules A. The color scale of each image goes from three times the rms noise level to the peak brightness. The synthesized beam sizes of the three images are indicated by the white oval in the bottom left corner of each panel, and are summarized along with the rms noise levels in Table 3.1.

been proposed (e.g., Mason et al. 1988; Meier et al. 1991; Morrison & Sadun 1996; Saxton et al. 2002; Gizani & Leahy 2003): either the rings are caused by a series of shocks between the old lobe material and new material from jet outbursts or the rings form the surfaces of multiple inner lobes associated with separate AGN outbursts.

In the shock model, adiabatic compression and particle acceleration are assumed to be responsible for producing thin and curved emission regions, which closely match the observed morphology of the rings. Although it is an idealized assumption that the compression is adiabatic, this is a commonly employed assumption when studying shock models in Hercules A and other sources (e.g., Meier et al. 1991; Brüggen et al. 2007; Jubelgas et al. 2007). However, the shock model is difficult to match with the spectral indices of the rings, which are relatively flat compared to the lobes, even at low frequencies. This implies that the shock wave induces a significant amount of particle acceleration. Although the observed spectral indices are not unusual for shock waves, it is peculiar that the outermost ring in the western lobe features a significantly steeper spectrum. Assuming that the lobe spectrum evolves mainly due to aging, the spectral index of the outermost ring could be obtained solely through adiabatic compression. In addition, the spectra of the rings have been found to be similar to that of the eastern jet, which would have to be merely a coincidence (Gizani & Leahy 2003).

In the second scenario the rings could be formed as the surface of inner lobes. As the jetted plasma decelerates, its beaming is reduced and its apparent brightness increases. This also provides an explanation for the lack of visible rings in the eastern lobe, where this effect works in the opposite way. Time retardation between the two lobes due to their inclination to the line of sight can also break their symmetry. Without invoking any particle acceleration, the steep spectrum of the outermost ring is no longer problematic. However, this strong rim-brightening is generally not observed in lobes.

Using new International LOFAR Telescope observations at 144 MHz, and Karl G. Jansky Very Large Array (VLA) observations in both the L and C bands, we aim to study the spectral properties of Hercules A between 144 MHz and 7 GHz at subarcsecond angular resolution. This wide range of observing frequencies provides an unparalleled data set to study the spectral properties of the source, and to test for any spectral turnovers due to absorption mechanisms, which generally occur at frequencies below 1 GHz. Furthermore, the unprecedented angular resolution and sensitivity at low frequencies provide a large lever arm in frequency space, facilitating an investigation into the origin of the rings in the Hercules A lobes.

In this paper we adopt a ΛCDM cosmology with a Hubble parameter of $H_0 = 67.4$ km s^{-1} Mpc^{-1}, a matter density parameter of $\Omega_m = 0.315$, and a dark energy density parameter of $\Omega_\Lambda = 0.685$ (Planck Collaboration 2020). We define our spectral indices α according to $S \propto \nu^\alpha$, where S is flux density and ν is frequency.

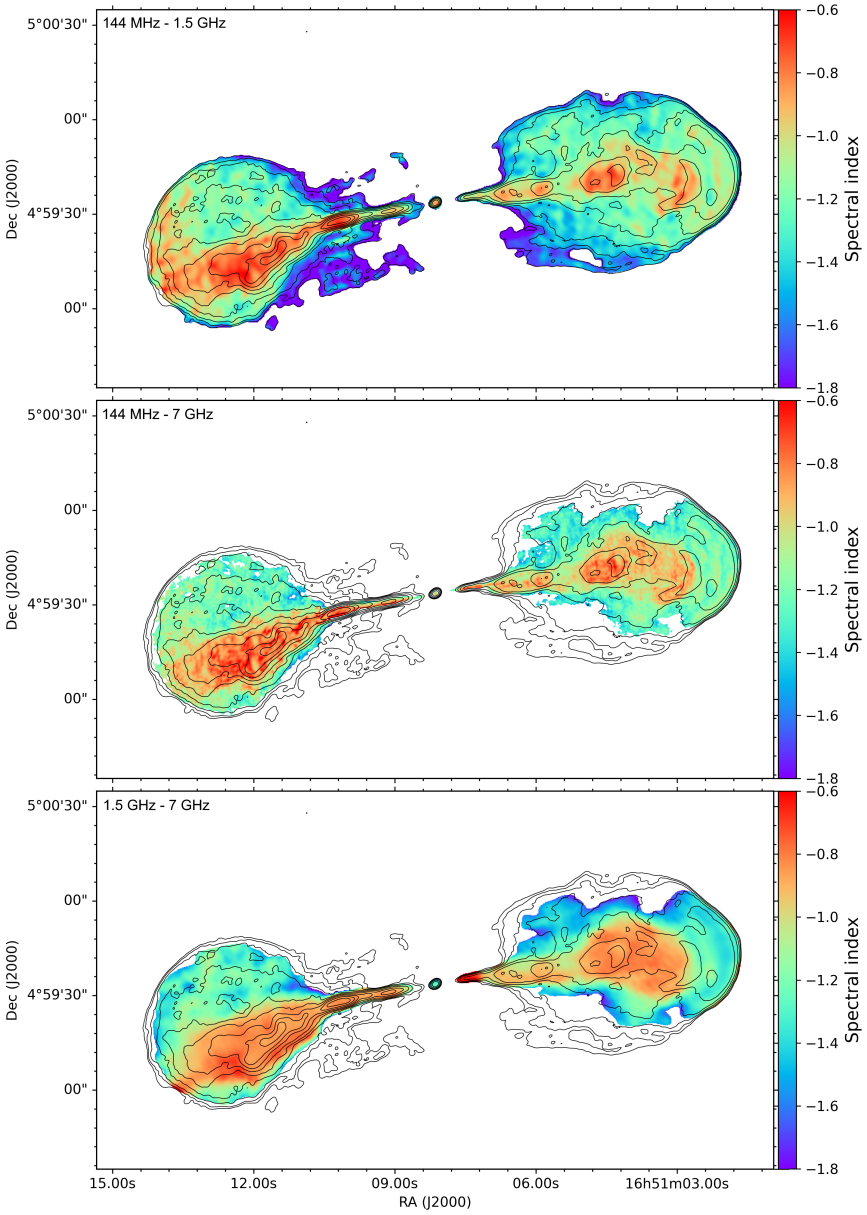

Figure 3.2: Spectral index maps of Hercules A between 144 MHz and 1.5 GHz (top panel), 144 MHz and 7 GHz (middle panel), and 1.5 GHz and 7 GHz (bottom panel). The contours indicate the L-band emission (1.5 GHz), and are drawn at [1, 2, 4, 8, ...] $\times$ $5\sigma_{\rm rms}$, where $\sigma_{\rm rms} = 224.2$ µJy beam^{-1}.

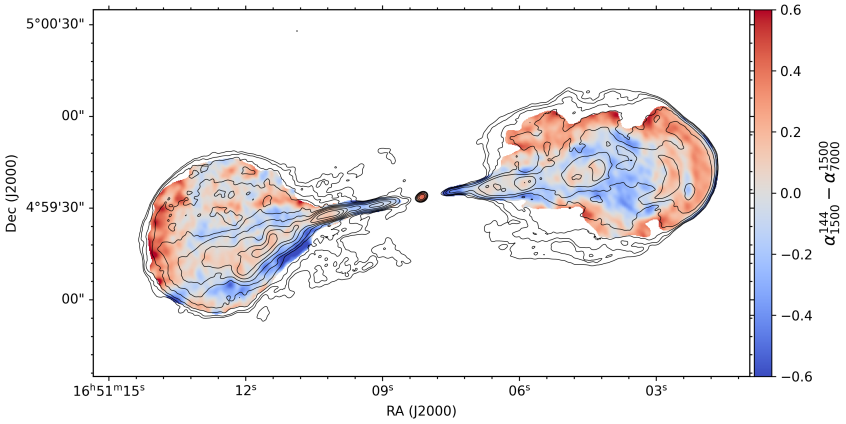

Figure 3.3: Spectral index curvature map of Hercules A. The spectral index curvature is calculated as the spectral index between 144 MHz and 1.5 GHz minus the spectral index between 1.5 GHz and 7 GHz. The red regions indicate where the spectrum is steeper at high frequencies than at low frequencies, whereas the blue regions indicate where the spectrum is flatter at high frequencies than at low frequencies. The contours indicate the L-band emission (1.5 GHz), and are drawn at [1, 2, 4, 8, ...] $\times 5\sigma_{\rm rms}$, where $\sigma_{\rm rms} = 224.2$ µJy beam^{-1}.

3.2 Observations and data reduction

3.2.1 LOFAR

Hercules A was observed with LOFAR's High Band Antennas (HBA, Van Haarlem et al. 2013) at frequencies between 120 and 168 MHz (PI: Timmerman, Project code: LC14-019). The data were recorded with spectral channels of 12 kHz to cover a total bandwidth of 48 MHz and with a time resolution of 1 second per integration. The observation took place on 8 June 2020, for a duration of 4 hours. The gain and bandpass calibrator source 3C 295 was observed for 10 minutes before and after the target scan. The initial data reduction was performed using Prefactor (Van Weeren et al. 2016; Williams et al. 2016; de Gasperin et al. 2019), which performed the initial flagging and used a model of the calibrator source to derive the calibration solutions for the Dutch stations. In particular, Prefactor first derived the polarization alignment and Faraday rotation. Based on these solutions, it derived the bandpass calibration solutions. Next, the clock corrections were derived by clock-total electron content (TEC) separation. These calibration solutions were then applied to the target data, after which the data were flagged again and averaged to a time resolution of 8 seconds and frequency channels of 98 kHz. Finally, a sky model of the target was obtained from the TIFR GMRT Sky Survey (TGSS) and used to perform a phase-only calibration cycle.

After this, the LOFAR-VLBI pipeline developed by Morabito et al. (2022) was employed to perform the initial calibration of the international LOFAR stations. This pipeline applied the Prefactor solutions to the unaveraged data containing

all stations. Then, the pipeline identified the best in-field calibrator source from the Long Baseline Calibrator Survey (LBCS, Jackson et al. 2016, in prep.), and used this to derive the antenna delays by solving for the TEC. In the case of this observation, the target source Hercules A was used for this calibration step due to its high flux density. Finally, these calibration solutions were applied to the data to obtain the final calibrated data set.

To further improve the quality of the calibration, we performed phase and amplitude self-calibration on Hercules A using the Default Preprocessing Pipeline (DPPP, Van Diepen et al. 2018) for deriving and applying updated calibration solutions and WSCLEAN (Offringa et al. 2014) for imaging. The final imaging was performed using the Briggs weighting scheme (Briggs 1995) with a robust parameter of -1, according to the Common Astronomy Software Application (CASA; McMullin et al. 2007) definition. To calibrate the flux density scale, we scaled the final image (see Fig. 3.1) to match the data from Kellerman et al. (1969), where we interpolated their flux density measurements between the two nearest frequencies, which are 38 and 178 MHz. The low-frequency measurements of Kellerman et al. (1969) captured all of the flux density of Hercules A due to their low-resolution observations. A correction factor of 1.09 was applied to the data from Kellerman et al. (1969) to convert their measurements to the Scaife & Heald (2012) flux density scale, which is identical to the RCB flux density scale (Roger et al. 1973) at these low frequencies. We assume a 10% uncertainty on the absolute flux scale due to intrinsic problems at low frequencies.

3.2.2 Karl G. Jansky Very Large Array

In addition to the LOFAR observations, Hercules A was observed with the VLA in the L band (1–2 GHz) and the C band (6–8 GHz) between September 2010 and September 2011 (Project code: TDEM0011). The L-band observations were performed in the A, B, and C configurations, while the C-band observations were also performed in D configuration. The data were recorded in full polarization mode, with spectral channels of 1 MHz for the L-band observations and 2 MHz for the C-band observations. To exploit the complete 4 GHz of bandwidth available in the C band, the observations were performed separately for the lower and upper halves of the C band. The lower half of the C-band data were recently presented by Wu et al. (2020), and the upper half of the C-band data are now presented along with the L-band observations for the first time. To calibrate both the flux density scale and the bandpass, scans on 3C 286 were included in the observations. PKS J1651+0129 was used for phase-reference calibration. The flux density scale of the VLA observations was set to the Perley & Butler (2017) scale, which is consistent with the Scaife & Heald (2012) flux density scale to within 5%.

The data reduction was performed using the Obit software package (Cotton 2008). First, the data was Hanning smoothed and flagged. Next, the parallactic angle corrections, the delay calibration solutions, and the bandpass calibration solutions were determined. Using these solutions, the gains of the calibrator sources were derived based on source models and the flux density scale of the phase reference source was determined. Following this calibration procedure the

Table 3.1: Properties of the images shown in Fig. 3.1.

	HBA	L band	C band
Observatory	LOFAR	VLA	VLA
Frequency (MHz)	144	1500	7000
Bandwidth (MHz)	48	1024	2048
Total flux density (Jy)	474.7	51.5	11.2
Flux scale uncertainty	10%	5%	5%
rms noise (µJy beam^{-1})	395.4	224.2	6.1
b_{major} (")	0.547	2.085	0.396
b_{minor} (")	0.234	1.592	0.349
b_{PA} (deg. East of North)	1.602	-59.930	86.550

data was flagged again, and the entire calibration was repeated with all flags applied from the start. Finally, the calibration solutions were applied to the data. To improve the calibration, Hercules A and the calibrator source, 3C 286, were both self-calibrated. Based on the refined model of 3C 286, corrections to the amplitude calibration were derived and applied to Hercules A. Hercules A was first self-calibrated based on the individual data sets. Then, these data sets were combined based on their spectral bands, and finally self-calibrated again. The imaging of the final data products was performed with multi-resolution CLEAN using the Briggs weighting scheme with robust parameters of -2.5 (L band) and -1 (C band), according to the Astronomical Image Processing System (AIPS) definition. We assume a 5% uncertainty on the absolute flux scale in accordance with Perley & Butler (2017).

3.3 Results

To investigate the nature of the rings, spectral index maps were produced between all three observing bands, as shown in Fig. 3.2. To ensure a consistent sensitivity to the different spatial scales, upper and lower limits on the baseline length were applied to the LOFAR data to match both the L- and C-band VLA data. This reduced the largest angular scale to which the data are sensitive to 4.2 arcminutes in the case of a match with the C-band data and 20 arcminutes in the case of a match with the L-band data, both of which exceed the maximum angular scale of Hercules A (190 arcseconds). The resulting images were convolved to the same synthesized beam and confirmed to be aligned based on the central compact source. Finally, all regions below a 5σ confidence level in the spectral index map were masked out. Tests were performed to ensure that bowl effects due to the lack of short baselines do not introduce significant features in the spectral index maps.

In each of the spectral index maps, the jets are found to feature a spectral index of around $\alpha = -0.8$ between the three bands, which is flatter than the typical values derived for the lobes. In the eastern lobe the flow of jetted plasma can be clearly traced by the gradual steepening of its spectrum as it ages and

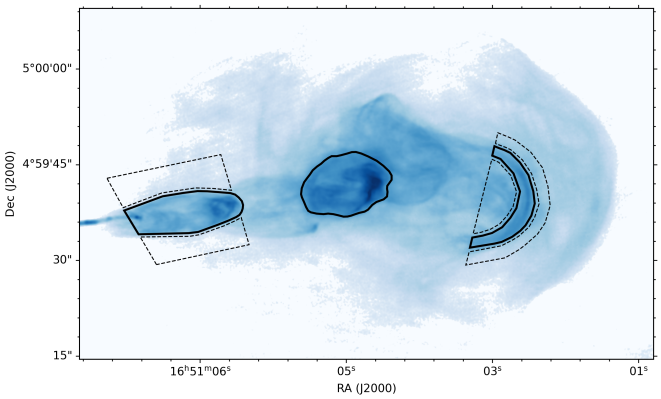

Figure 3.4: VLA image of the western lobe of Hercules A in C band (7 GHz). The solid black regions indicate the regions used to measure the flux density of the rings. The regions with the dashed black borders indicate the regions used to estimate the background surface brightness of the lobe material at the position of the rings.

merges into the lobe. The jet appears to slowly diffuse, and to reach the outer edge of the lobe before diffusing into the lobe and eventually sinking back towards the central galaxy. In the western lobe the jetted plasma can mostly be seen as a relatively flat-spectrum ($\alpha > -1$) region in the center of the lobe. In addition, the rings are clearly distinguishable in the spectral index map between 144 MHz and 1.5 GHz. The spectral index of the bridge in between the two radio lobes remains poorly constrained, as this structure is too faint in the VLA maps, but will, in any case, have to be as steep as $\alpha = -1.8$ or less to be consistent with a non-detection in the L-band image (1.5 GHz).

For use in the Discussion (Section 4), we calculate the difference between the spectral index maps between 144 MHz and 1.5 GHz, and 1.5 GHz and 7 GHz (Fig. 3.3). This difference allows us to determine whether the spectral index is constant from low to high frequencies, or if the spectral index changes. This can be interpreted as a measure of the curvature of the spectrum. In the spectral curvature map, the red regions indicate that the spectrum is steeper at high frequencies, whereas the blue regions indicate that the spectrum is steeper at low frequencies. In the western lobe, the three ring structures are distinguishable and feature steepening spectra. Interestingly, each ring shows more steepening than the previous one, counting from the core. The ring closest to the core shows an average spectral index curvature of 0.02 ± 0.07. The ring in the middle shows an average spectral index curvature of 0.04 ± 0.07. Finally, the farthest ring from the AGN shows an average spectral index curvature of 0.16 ± 0.07. We note that the uncertainties on these measurements are dominated by systematic uncertainties, and are thus strongly spatially correlated.

3.4 Discussion

The origin of the ring structures in the western lobe has been one of the main topics of debate regarding Hercules A since their discovery by Dreher & Feigelson (1984). Currently, the shock model (e.g., Mason et al. 1988; Meier et al. 1991) and inner-lobe model (e.g., Morrison & Sadun 1996) remain in consideration, as neither model could be easily given preference (Gizani & Leahy 2003). However, our new observations extend the observed frequency range to much lower frequencies, while maintaining sufficient angular resolution to clearly resolve the rings. This allows us to measure the spectral properties of the rings over more than a decade of frequency, facilitating a comprehensive test of which model fits the data best.

The shock model provides one explanation for the morphology of the rings. In this model the rings are the shocks which induce adiabatic compression and particle acceleration when irregularities in the jet pass through the lobe. This scenario is able to recover the observed structure in the eastern lobe (Gizani & Leahy 2003). However, this model struggles to provide a compelling explanation for the observed spectral indices of the rings in the western lobe. First, the rings are found to have a relatively flat spectral index. Between our two lowest frequency bands we observe spectral indices of the rings in the western lobe of around $\alpha = -0.8$, which is consistent with the spectral index of the eastern jet. The true value is most likely flatter than this as the observed spectral index includes contributions from the steeper-spectrum lobe material along the line of sight to the ring. Such flat spectral indices are unlikely to be produced merely through adiabatic compression, as adiabatic compression can only straighten the spectrum towards the injection spectral index (Enßlin & Gopal-Krishna 2001), and even the low-frequency spectral index of the lobe is about $\alpha = -1.2$. In comparison, the spectra of the rings at high frequencies are flatter than the spectrum of the lobes at low frequencies, indicating that particle acceleration is required as well. However, if particle acceleration by shocks plays a role, then it is difficult to explain why the outermost ring in the western jet features the steepest spectrum. The outermost ring forms the bow shock ahead of the western jet as it is caused by the frontal collision between the jet and the lobe. Therefore, it should be the strongest shock of the set. To resolve this, the outermost ring requires a significantly different Mach number and mixture between thermal and relativistic components compared to the other rings.

An alternative model posits that the rings in the western lobe are the surfaces of inner lobes created by the jet (Gizani & Leahy 2003). As the western jet recedes away from us, the brightness of this jet is strongly reduced by Doppler dimming. However, as the jets form inner lobes within the old plasma, the surface of this jetted plasma is decelerated, which reduces their Doppler dimming. This gives the surface of these inner lobes an apparent increase in brightness from our perspective. In the inner-lobe model, the bright rings are expected to be formed by the jetted material, and should therefore be similar to the jet in terms of spectral index, which is consistent with our observations. In particular, it is not problematic that the outer ring has the steepest spectrum of the set due to radiative aging since particle acceleration and adiabatic compression are not expected to contribute significantly. However, the inner-lobe model does have difficulty explaining the

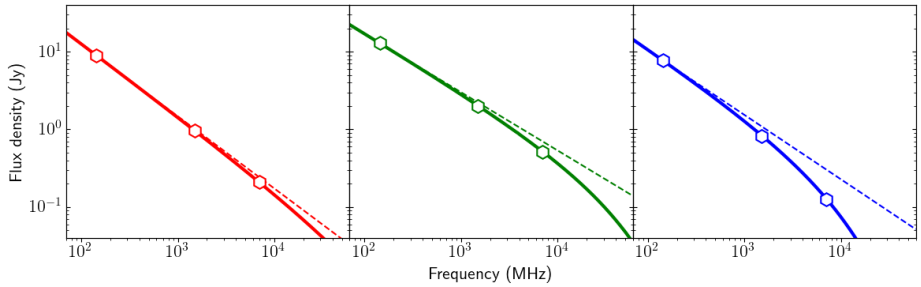

Figure 3.5: Illustration of the spectral curvature of the rings in the western lobe, assuming a Jaffe-Perola model (Jaffe & Perola 1973). From left to right, the three panels show the inner, middle, and outer rings with injection indices of $\alpha_{\rm inj} = -0.93$, $\alpha_{\rm inj} = -0.75$, and $\alpha_{\rm inj} = -0.83$, respectively. The hexagons indicate the total flux densities of the rings at the three different frequencies. The error bars on these measurements are drawn, but do not extend beyond the marker. The solid lines show the spectra of the three rings with the amount of curvature as measured from the flux density measurements without background subtraction. The dashed lines show the respective injection spectra without any curvature for comparison.

morphology of the rings. Inner lobes generally do not feature rim brightening, although this could at least partially be explained if the inner lobes are mainly filled with the Doppler-beamed jetted stream (Gizani & Leahy 2003). The inner-lobe model implies that the AGN experiences intermittent periods of activity, similar to that observed in the Perseus cluster (Fabian et al. 2006), Hydra A (Wise et al. 2007), MS0735 (Vantyghem et al. 2014), some peaked-spectrum radio sources (Callingham et al. 2017), and the Phoenix cluster (Timmerman et al. 2022b), for instance. In the case of Hercules A evidence of such intermittency has already been provided by Gizani et al. (2002), who detect a possible pair of parsec-scaled radio jets from a new outburst, and O'Dea et al. (2013), who suggest based on Hubble Space Telescope observations that the AGN experienced an episode of activity about 60 Myr ago, and that it restarted about 20 Myr ago.

Accurate spectral index measurements can provide valuable information on the composition and physical conditions present in the emission region. Our low-frequency data allow us to not only accurately determine the overall spectral index, but also detect curvature in the spectrum. In the shock model the rings are formed by adiabatic compression and particle acceleration in the lobe. Both of these mechanisms work to straighten out the spectrum towards a single power-law model. On the other hand, the inner-lobe model predicts that the rings should feature the same spectral properties as the jet, which is subject to aging. In a synchrotron-emitting plasma, the higher-energy electrons radiate away their energy first, causing a break in the synchrotron spectrum (e.g., Scheuer & Williams 1968). As the plasma ages, this break frequency shifts towards lower frequencies, leading to an increasingly steep spectrum at higher frequencies.

As presented in Fig. 3.3, we observe a trend where each consecutive ring, count-

ing from the core, shows more spectral steepening. To exclude the possibility that the spectral curvature trend emerges due to variations in the lobe emission along the line of sight, we also measured the spectral curvature by estimating the flux density contribution of the rings independent of the foreground material (see Fig. 3.1). We did this by first measuring the total flux density within the ring region, and then subtracting the flux density due to the background surface brightness of the lobe. The regions used for this measurement in the C band are shown in Fig. 3.4. The background level is estimated as the mean surface brightness of two regions on opposite sides of the rings. We assume a 10% uncertainty on all flux density measurements. Using the total flux density measurements without background subtraction, we obtained spectral curvature values $\alpha_{\rm curv} = \alpha_{1500}^{144} - \alpha_{7000}^{1500}$ of 0.04 ± 0.13, 0.09 ± 0.13, and 0.27 ± 0.13 for the inner, middle, and outer rings, respectively. For the background subtraction we excluded the middle ring from the analysis as the complex morphology of the ring and its environment prevent a reliable background level from being estimated. This leaves only the inner and outer rings, for which we estimate background-subtracted spectral curvatures of 0.15 ± 0.13 and 0.36 ± 0.13, respectively.

We measure an increasing spectral curvature of the rings before and after background subtraction, implying that we are detecting the typical break in the synchrotron spectrum as a consequence of aging. This is also consistent with the similar spectral curvature values we found between the inner and middle ring, with the outer ring showing much stronger curvature. An illustration of the complete spectrum of each of the rings is shown in Fig. 3.5. A Jaffe-Perola spectral model (Jaffe & Perola 1973) was fitted to the flux density measurements of each of the three rings to derive their respective injection index and break frequency. In the illustration, the break frequencies of the rings shift to lower frequencies the farther the rings are from the central AGN, causing the spectrum to steepen. We find relatively steep injection indices for the three rings of $\alpha = -0.75$ up to $\alpha = -0.93$. However, similar and steeper injection indices are not uncommon (e.g., Bîrzan et al. 2008; Harwood et al. 2013, 2015; Shulevski et al. 2015). Although this model is strongly based on Doppler effects, it should be noted that the spectra will be significantly redshifted and will undergo beaming effects. However, as the rings all have a reduced Doppler factor due to the deceleration of the jetted plasma, the redshift of their spectra will be relatively low. This prevents the redshift of the rings from significantly affecting their relative break frequencies.

To investigate whether the observed amount of spectral curvature is realistic for Hercules A, we derived the magnetic field strength in the jet required to produce such spectra. From our observations, we measure angular distances between the three rings of about 24 arcseconds, with a distance between the core of the AGN and the innermost ring of 37 arcseconds. This corresponds to projected physical distances of 66 kpc between the rings and 103 kpc between the core and the innermost ring. Assuming an angle between the jets and the line of sight of 50 degrees (Gizani & Leahy 1999) and a jet speed of $\beta = 0.8$ (Gizani & Leahy 2003), we find that the innermost, middle, and outermost rings are composed of plasma with ages of approximately 550 kyr, 900 kyr, and 1250 kyr, respectively. Here, we assume that the inner lobes propagate at the speed of the jets, which is a rough

approximation and is likely an upper limit to the true speed. However, more accurate measurements are unavailable, and the main goal is only to test whether the approximate numbers are sensible. Given these ages, and assuming a Jaffe-Perola spectral model, we derive magnetic field strengths in the jet of 28 μG, 36 μG, and 45 μG for the innermost, middle, and outermost rings, respectively. This trend in increasing magnetic field strength could be an indication of a deviation in the age estimates due to errors in the line-of-sight angle or jet speed, but it should be noted that there are also additional uncertainties due to the assumption of a Jaffe-Perola model, the methodology of measuring spectral curvature and the fact that there may be a small amount of redshift due to the recession of the jet. However, the approximate values of the magnetic field strength under the assumption of an inner-lobe model are in accordance with typical values derived for the jets of AGNs (e.g., Kataoka & Stawarz 2005; Godfrey & Shabala 2013).

In addition to the spectral steepening of the rings, we also see that the environment of the jets shows spectral flattening at high frequencies, as shown in Fig. 3.3. This could be produced, for instance, by particle acceleration in regions that are opaque at low frequencies, or it could indicate a mismatch in the surface brightness sensitivities of LOFAR and the VLA. Such a discrepancy can emerge due to differences in the *uv*-coverage of the two arrays. LOFAR in particular suffers from a sparse *uv*-coverage at intermediate scales (1–2 arcsecond). However, the total flux density of the source has been carefully calibrated across all three frequencies and the consistent measurements obtained using different methods indicate the validity of our results.

3.5 Conclusions

In this paper we presented new LOFAR and VLA observations of Hercules A with the aim of investigating the nature of the ring features seen in the radio lobes. Our LOFAR observations clearly resolve the jet and ring structures in the lobes at 144 MHz, enabling the lobes to be studied at low frequencies, for the first time at a sub-arcsecond angular resolution. The bridge of emission in between the two lobes is only significantly detected at 144 MHz, which implies a spectral index of $\alpha = -1.8$ or steeper to be consistent with a non-detection in our L-band observations (1.5 GHz).

To study the nature of the rings in the lobes of Hercules A, we investigate whether our observations are consistent with a shock model or an inner-lobe model. Spectral index mapping between 144 MHz and 7 GHz reveals that the rings in the western lobe feature spectral steepening at high frequencies. In particular, the spectral steepening increases as the rings are farther away from the central AGN. This suggests that the rings are subject to synchrotron aging, which is a clear prediction of the inner-lobe model. Therefore, we conclude that the observations presented in this paper are more consistent with the inner-lobe model where the jetted material from intermittent periods of AGN activity inflates small lobes within the outer lobe, which appear as ring-like structures. However, we do not exclude that adiabatic compression and particle acceleration contribute to the

brightness of the rings as well, and we note that definitive evidence to settle this debate remains yet to be found.

Even though this model contributes evidence in favor of the inner-lobe model, it still struggles to provide a complete explanation for the morphology of the rings. Supporting evidence could likely be obtained through detailed magnetohydrodynamical (MHD) simulations. The jetted outflows can be simulated based on our current understanding of the environment of Hercules A. By replicating the observed ring-like structures, their exact nature can be confirmed. In particular, MHD modelling would have to focus on reproducing the observed morphology and spectral properties of the rings in the western lobe, and on the lack of ring structures in the eastern lobe.

Acknowledgements

RT and RJvW acknowledge support from the ERC Starting Grant ClusterWeb 804208. JRC thanks the Nederlandse Organisatie voor Wetenschappelijk Onderzoek (NWO) for support via the Talent Programme Veni grant. CO and SB acknowledge support from the Natural Sciences and Engineering Research Council (NSERC) of Canada. AB acknowledges support from the VIDI research programme with project number 639.042.729, which is financed by the Netherlands Organisation for Scientific Research (NWO). JM acknowledges financial support from the State Agency for Research of the Spanish MCIU through the "Center of Excellence Severo Ochoa" award to the Instituto de Astrofísica de Andalucía (SEV-2017-0709) and from the grant RTI2018-096228-B-C31 (MICIU/FEDER, EU). This paper is based (in part) on data obtained with the International LOFAR Telescope (ILT) under project code LC14-019. LOFAR (Van Haarlem et al. 2013) is the Low Frequency Array designed and constructed by ASTRON. It has observing, data processing, and data storage facilities in several countries, that are owned by various parties (each with their own funding sources), and that are collectively operated by the ILT foundation under a joint scientific policy. The ILT resources have benefitted from the following recent major funding sources: CNRS-INSU, Observatoire de Paris and Université d'Orléans, France; BMBF, MIWF-NRW, MPG, Germany; Science Foundation Ireland (SFI), Department of Business, Enterprise and Innovation (DBEI), Ireland; NWO, The Netherlands; The Science and Technology Facilities Council, UK; Ministry of Science and Higher Education, Poland. The National Radio Astronomy Observatory is a facility of the National Science Foundation operated under cooperative agreement by Associated Universities, Inc.

4

Measuring cavity powers of active galactic nuclei in clusters using a hybrid X-ray–radio method

A new window on feedback opened by subarcsecond LOFAR-VLBI observations

Roland Timmerman, Reinout J. van Weeren, Andrea Botteon, Huub J. A. Röttgering, Brian R. McNamara, Frits Sweijen, Laura Bîrzan, Leah K. Morabito,

Published in Astronomy & Astrophysics, December 2022, volume 668, A65.

Abstract

Measurements of the quantity of radio-mode feedback injected by an active galactic nucleus into the cluster environment have mostly relied on X-ray observations, which reveal cavities in the intracluster medium excavated by the radio lobes. However, the sensitivity required to accurately constrain the dimensions of these cavities has proven to be a major limiting factor and it is the main bottleneck of high-redshift measurements. We describe a hybrid method based on a combination of X-ray and radio observations, which aims to enhance our ability to study radio-mode feedback. In this paper, we present one of the first samples of galaxy clusters observed with the International LOFAR Telescope (ILT) at 144 MHz and use this sample to test the hybrid method at lower frequencies than before. By comparing our measurements with results found in literature based on the traditional method using only X-ray observations, we find that the hybrid method provides consistent results to the traditional method. In addition, we find that the correlation between the traditional method and the hybrid method improves as the X-ray cavities are more clearly defined. This suggests that using radio lobes as proxies for cavities may help to circumvent systematic uncertainties in the cavity volume measurements. Encouraged by the high volume of unique ILT observations which have been successfully processed, this hybrid method enables radio-mode feedback to be studied at high redshifts for the first time even for large samples of clusters.

4.1 Introduction

The feedback process between active galactic nuclei (AGNs) and the dilute intracluster medium (ICM) that permeates a galaxy cluster is understood to be of critical importance in the formation and evolution of clusters of galaxies (e.g., McNamara & Nulsen 2007; Fabian 2012; Gitti et al. 2012a). The hot ICM ($T = 10^7 - 10^8$ K) emits strong X-ray emission through thermal bremsstrahlung, which cools this medium down and causes it to sink down the gravitational well in the form of a cooling flow (Fabian 1994). As this cooling flow accretes onto the brightest cluster galaxy (BCG) in the center of a cluster, it is expected to trigger a high rate of star formation. However, the observed star-formation rate is generally found to be lower than predicted based on the strength of the cooling flow (e.g., Fabian et al. 1982; McNamara & O'Connell 1989; Kaastra et al. 2001; Peterson et al. 2003; Peterson & Fabian 2006). In addition, the amount of energy radiated away by the ICM suggests that this medium should cool down on a timescale much shorter than the lifetime of the cluster.

As the cooling flow accretes onto the BCG, it feeds the AGN located in the center of the galaxy. The resulting activity of the supermassive black hole produces large amounts of energy in the form of radiation and strong jetted outflows. In the scenario where the feedback is predominantly radiative, the AGN is said to be in a 'quasar mode', whereas if the jetted outflows are dominant, the AGN is said to be in 'radio mode' (Croton et al. 2006). As this energy is injected into the ICM, it completes the feedback cycle which prevents a runaway cooling event. The jetted outflows expand into large lobes against the internal pressure of the ICM (Bridle & Perley 1984). This process can be observed in the radio regime of the electromagnetic spectrum, which shows the magnetized plasma emitted by the supermassive black hole, or using X-ray radiation, where these lobes which have been produced by the AGN appear as cavities in the ICM (e.g., Böhringer et al. 1993; Carilli et al. 1994).

Efforts have been made to employ radio observations to study the radio-mode feedback of AGNs, but they have not been able to demonstrate a reliable ability to measure the quantity of feedback (e.g., Bîrzan et al. 2008; Cavagnolo et al. 2010; O'Sullivan et al. 2011; Kokotanekov et al. 2017). Some of the best results have been obtained using bolometric radio luminosity measurements of the radio lobes, excluding the central core (Bîrzan et al. 2004, 2008). However, this method has only obtained a weak correlation with X-ray measurements of the power required to excavate a cavity for two reasons. First of all, bolometric radio luminosity measurements require deep observations along a wide frequency range, although at high frequencies the sensitivity to the radio lobes suffers from the increasingly steep spectrum of the aging radio plasma. This makes bolometric radio measurements of radio lobes difficult to obtain. In addition, even with perfect bolometric radio luminosity measurements, the correlation with the X-ray cavity power is weakened by the dependence of the radio emissivity and X-ray cavity power on additional parameters. Most notably, the synchrotron emissivity depends on the square of the local magnetic field strength, and the particle composition of the jets determines the ratio between the total momentum of the jet and the momentum

of the synchrotron-emitting electrons. Simulations show that the radio luminosity of lobes can vary with more than an order of magnitude for a given jet power (Hardcastle & Krause 2013, 2014).

The cavity power estimates derived from X-ray observations have generally been considered to offer the most reliable estimate of the amount of feedback (e.g., McNamara & Nulsen 2012; Bîrzan et al. 2004, 2014), but this method is also not without weaknesses. Clearly detecting the cavities requires very sensitive observations, which are infeasible at relatively high redshifts ($z > 0.6$, Hlavacek-Larrondo et al. 2015). In addition, unless a cluster is very relaxed, the ICM will feature more structure than just the cavities, which can affect the ability to reliably constrain the shape and size of the cavities.

Recent developments in data processing (Morabito et al. 2022) have enabled the calibration and imaging of observations taken with the complete International LOw Frequency ARray (LOFAR, Van Haarlem et al. 2013) Telescope (ILT). Long-baseline observations can now be reliably processed, even for complex (e.g., Timmerman et al. 2022b) or faint sources. The international stations of LOFAR are able to overcome the main obstacle of low-frequency radio observations: angular resolution. While the Dutch section of LOFAR offers an angular resolution of $\theta \approx 6$ arcseconds at 144 MHz, the inclusion of the international stations enables an angular resolution of $\theta \approx 0.3$ arcseconds to be reached. By observing at low frequencies with very long baselines, LOFAR is able to provide both the sensitivity and the angular resolution required to resolve the steep-spectrum emission from the radio lobes of AGNs.

We have observed a sample of cool-core galaxy clusters with AGNs up to a redshift of $z = 0.6$ using the ILT. Leveraging LOFAR's upgraded capabilities, we present a hybrid method of measuring the cavity power based on a combination of X-ray and radio data, which is likely to make these measurements feasible at higher redshifts than before. We test this method on our observed low-redshift sample to confirm that this method provides consistent results to those found in literature based on the traditional X-ray-based method.

In this paper, we adopt a ΛCDM cosmology with a Hubble parameter of $H_0 = 70$ km s^{-1} Mpc^{-1}, a matter density parameter of $\Omega_m = 0.3$, and a dark energy density parameter of $\Omega_\Lambda = 0.7$. We define our spectral indices α according to $S \propto \nu^\alpha$, where S is flux density and ν is frequency. All uncertainties denote the 68.3%=1σ confidence interval.

4.2 Methodology

4.2.1 Current cavity power estimation

The most favored method to measure the amount of radio-mode feedback injected into the ICM by the AGN has been to perform a dynamical analysis on the cavities in the ICM. Following the method described by Bîrzan et al. (2004), the amount of energy required to inflate a radio lobe ($E_{\rm cav}$) is the sum of the internal energy of the lobe ($E_{\rm internal}$) and the work required to excavate the region against the external ICM pressure (W). This gives

Table 4.1: Summary of the sample of galaxy clusters used in this paper. The horizontal line separates the clusters that are studied at high resolutions (∼0.3 arcseconds, top half) from the clusters that are studied at low resolutions (∼6 arcseconds, bottom half).

Cluster name	R.A. (J2000)	Dec. (J2000)	Redshift z	Mass M_{200} (10^{14} $M_\odot$)
Perseus (NGC 1275)	03h19m48.16s	41d30m42.11s	0.018	$6.65^{+0.43}_{-0.46}$ (1)
Abell 1795	13h49m00.50s	26d35m07.00s	0.063	$15.39^{+3.17}_{-2.92}h_{50}^{-1}$ (2)
Abell 2029	15h10m58.70s	05d45m42.00s	0.077	11.2 ± 0.4 (3)
ZwCl 2701	09h52m49.10s	51d53m05.00s	0.214	5.2 ± 0.5 (3)
4C+55.16	08h34m54.90s	55d34m21.07s	0.241	0.923 ± 0.182 (4)
RX J1532.9+3021	15h32m53.78s	30d20m59.41s	0.363	11.1 ± 1.1 (3)
MACS J1720.2+3536	17h20m16.80s	35d36m27.00s	0.391	8.1 ± 1.3 (3)
MACS J1423.8+2404	14h23m47.70s	24d04m40.00s	0.545	7.2 ± 0.9 (3)
Perseus (NGC 1275)	03h19m48.16s	41d30m42.11s	0.018	$6.65^{+0.43}_{-0.46}$ (1)
Abell 2199	16h28m37.00s	39d31m28.00s	0.030	$6.0^{+1.5}_{-1.8}$ (5,6)
2A 0335+096	03h38m35.30s	09d57m54.00s	0.035	$1.4^{115.5}_{-1.0}$ (5,7)
MKW 3S	15h21m50.70s	07d42m18.00s	0.045	5.1 (8)
Abell 1668	13h03m44.90s	19d16m37.20s	0.064	4.31 ± 1.63 (9)
Abell 2029	15h10m58.70s	05d45m42.00s	0.077	11.2 ± 0.4 (3)
3C 388	18h44m02.42s	45d33m29.81s	0.092	...
MS 0735.6+7421	07h41m40.30s	74d14m58.00s	0.216	7.12 ± 1.96 (10)

References. (1) Simionescu et al. (2011); (2) Reiprich & Böhringer (2002); (3) Mantz et al. (2016); (4) Takey et al. (2011); (5) Comerford & Natarajan (2007); (6) Łokas et al. (2006); (7) Voigt & Fabian (2006); (8) Pinzke et al. (2011); (9) Kopylova & Kopylov (2017); (10) Gitti et al. (2007)

$$\begin{aligned} E_{\rm cav} &= E_{\rm internal} + W \\ &= \frac{1}{\gamma - 1} pV + pV \\ &= 4pV, \end{aligned} \tag{4.1}$$

where γ is the adiabatic index of the radio lobe, p is the pressure of the surrounding ICM and V is the volume of the cavity. For a relativistic gas we know that $\gamma = 4/3$, leading to the final result.

To obtain the average power output of the AGN, this energy must be divided by the age of the cavity, which can be estimated in multiple ways. Firstly, because the radio lobe has a lower density than the surrounding ICM, a buoyant force acts upon this radio lobe, causing it to rise away from the center of the cluster. Assuming this dominates the kinematics of the lobe, the time required to reach the observed position of the cavity (the buoyancy timescale) can be estimated as

$$t_{\rm buoy} = R \sqrt{\frac{SC}{2gV}}, \tag{4.2}$$

where R is the projected distance to the center of the cluster, S is the cross-sectional area of the cavity, C is the drag coefficient ($C = 0.75$, Churazov et al. 2001), and g is the gravitational acceleration which we estimate following Bîrzan et al. (2004) using the approximation of an isothermal sphere such that $g \approx 2\sigma^2/R$ (Binney & Tremaine 1987), where σ is the stellar velocity dispersion.

Alternatively, because the lobe originates from a relativistic jet and therefore has a high amount of initial momentum, it can also be assumed that the cavity travels at the local speed of sound through the ICM. In this case, the age of the cavity can be estimated as

$$t_{\rm sound} = R \sqrt{\frac{\mu m_H}{\gamma kT}}, \tag{4.3}$$

where μ is the mean molecular weight, m_H is the mass of a hydrogen atom, γ is again the adiabatic constant which we assume to be equal to 5/3 for the ICM, and kT is the thermal energy of the ICM. Generally, these two estimates agree within a factor of two for cavities close to the center of the cluster (e.g., Bîrzan et al. 2004), and diverge as the cavities are more distant to the AGN. As the buoyancy timescale is expected to be more accurate for older cavities and agrees reasonably well with the sound speed timescale for newer cavities, we adopt the buoyancy timescale for the remainder of this paper.

Deriving most of the quantities required for these calculations has generally been performed based on X-ray observations. Estimating the cavity energy requires the ICM pressure and the volume of the cavities. The ICM pressure can be derived, for instance, by determining the temperature and density of the ICM as a function of radius, which immediately provides an estimate of the pressure. To obtain the cavity volume, an estimate of the smooth brightness profile of the X-ray emission is subtracted from the image, causing the cavities to appear as negatively

bright regions. From this, the dimensions and position of the cavity are generally derived assuming an ellipsoidal shape. Accurately measuring the cavity properties requires high-resolution X-ray observations, and therefore is almost exclusively performed using Chandra observations. These few quantities provide almost all the information required to estimate the cavity power, with only the stellar velocity dispersion remaining unknown in the case that the buoyancy timescale is assumed. This final parameter is normally derived through optical spectroscopy.

4.2.2 The hybrid X-ray–radio method

Although the high angular resolution provided by Chandra in principle enables small spatial scales to be resolved even at high redshifts, X-ray observations are plagued by a relatively low count statistics at high redshifts, which forms a bottleneck for the purely X-ray-based approach to constrain the size and shape of cavities. In addition, the ICM is in general not a smooth distribution. Additional structure in the ICM due to, for example, a recent merging event can make it difficult to reliably identify the cavities.

The radio lobes have previously been treated as proxies for the cavities in select clusters (e.g., Dunn & Fabian 2004; Allen et al. 2006; Cavagnolo et al. 2010; Gitti et al. 2010; Lanz et al. 2010; Ehlert et al. 2011; Vagshette et al. 2017; Seth et al. 2022), though generally this is avoided at high frequencies due to the lack of sensitivity to low-energy cosmic ray electrons, resulting in high systematic uncertainties. The first detailed study of this method was performed by Bîrzan et al. (2008) by comparing the cavity enthalpy estimated based on 327 MHz and 1400 MHz Very Large Array (VLA) observations with measurements obtained from Chandra X-ray images, where they found the 327 MHz observations to consistently overestimate the cavity enthalpy. Following this test, we employ radio observations taken with the ILT for the first time to probe the position, shape and size of the X-ray cavities by treating the radio lobes as proxies for the cavities. The enthalpy of the cavities is then derived using the volume measurements derived from radio observations and a pressure measurement derived from X-ray observations. Thanks to LOFAR's international stations, we now have a unique combination of angular resolution and sensitivity, offering an unprecedented view of the radio lobes.

This method has the advantage that in many instances the radio lobes will be detected much more clearly than the X-ray cavities, enabling cavity powers to be derived at higher redshifts than before. In addition, this method only requires observations at a single frequency, which therefore will also offer results more robustly compared to the multifrequency observations which were previously used to calculate the bolometric radio luminosity of the lobes. It is not uncommon for radio lobes to only be detected at low frequencies due to their steep spectra. Also, this method conveniently avoids requiring accurate flux scale calibration, which is known to be one of the main weaknesses of the current ILT calibration pipeline. Finally, because this method only depends on X-ray observations for ICM pressure measurements, which does not require high angular resolutions, it becomes more feasible for observatories like XMM-Newton to assist with the cavity

power measurements.

We note that one of the main sources of uncertainty from the purely X-ray-based approach persists in this method: the unknown projection effects. In addition, the sensitivity to the steep-spectrum radio plasma will decrease as this plasma ages, causing very old radio lobes to remain undetected in a standard-depth LOFAR pointing. It should be carefully checked if there is likely to be radio emission below the detection limit. If so, the radio-derived volume estimates may be unreliable. Finally, we note that even though it may be tempting to derive the equipartition pressure of the lobes, these estimates in general do not agree with the ICM pressure derived from X-ray observations (Croston & Hardcastle 2014).

4.3 Sample

We have compiled a sample of 8 targets based on the samples of Rafferty et al. (2006) and Bîrzan et al. (2008) for new high-resolution observations and a sample of 8 targets for low-resolution comparison based on the samples of Rafferty et al. (2006) and Bîrzan et al. (2020). Two targets of the low-resolution sample are in common with the high-resolution sample. This collective sample of 14 targets was based on the detection of X-ray cavities with an associated radio source, and spans a redshift range from $z = 0$ up to $z = 0.6$ (see Table 4.1).

For our high-resolution sample, we have processed and imaged observations taken with the ILT as described in Sect. 4.4.1. For our low-resolution sample, we mainly depend on images published as part of the LOFAR Two-Metre Sky Survey (LoTSS, Shimwell et al. 2017, 2019, 2022). For 2A 0335+096 and MS 0735.6+7421, LoTSS images are not available, so we instead use the images published in Ignesti et al. (2022) and Biava et al. (2021), respectively. Finally, for Perseus we have produced a low-resolution image using only the Dutch LOFAR stations after subtracting the dominant central component as observed in the high-resolution map, which previously interfered with attempts to image the cluster with an angular resolution of ∼6 arcseconds.

In addition to the LOFAR observations, we have processed archival VLA observations of our high-resolution sample to produce spectral index maps and aid with the identification of the radio structures. The details of these observations and the data reduction are described in Appendix 4.A.

4.4 Observations and data reduction

4.4.1 LOFAR

The sources in our sample have been observed with LOFAR's High Band Antennas at frequencies between 120 MHz and 168 MHz for a total of 8 hours per target. Each target observation was preceded and succeeded by a 10-minute-long observation of a well-known calibrator source for gain and bandpass calibration purposes. The initial data reduction and calibration was performed using the Prefactor software package (Van Weeren et al. 2016; Williams et al. 2016; de Gasperin et al.

Table 4.2: Summary of the LOFAR observations processed for the high-resolution images presented in this paper.

Cluster name	Project code	PI	Date	Duration
Perseus (NGC 1275)	LC6_015	Shimwell	3 Nov 2016	8 hours
Abell 1795	LC7_024	Shimwell	9 Feb 2017	8 hours
Abell 2029	LC14_019	Timmerman	10 Sep 2020	4 hours
			4 Oct 2020	4 hours
ZwCl 2701	LC9_019	Bîrzan	20 Feb 2018	8 hours
4C+55.16	LC14_019	Timmerman	9 Nov 2020	8 hours
RX J1532.9+3021	LC10_010	Bonafede	14 Sep 2018	8 hours
MACS J1720.2+3536	LC10_010	Bonafede	9 Jun 2018	8 hours
MACS J1423.8+2404	LC14_019	Timmerman	8 Oct 2020	8 hours

2019). After completing the initial flagging of data (Offringa et al. 2013, 2015), PREFACTOR derived the calibration solutions based on the calibrator source. These calibration solutions consist of the corrections for the polarization alignment and Faraday rotation, the bandpass, and the clock offsets. After applying all calibration solutions to the data, PREFACTOR performed another round of flagging and averaged the data to 8 seconds per integration and frequency channels with a bandwidth of 98 kHz. As a final step, a sky model of the field as provided by the TIFR Giant Metrewave Radio Telescope Sky Survey (TGSS, Intema et al. 2017) is used to calibrate the phases of the visibilities for the Dutch stations.

With the initial calibration of the Dutch stations completed, the LOFAR-VLBI pipeline developed by Morabito et al. (2022) is used to extend the calibration to the international LOFAR stations. First, the previously derived calibration solutions are transfered and applied to the target observation. Next, we select a bright and compact source in the field from the Long-Baseline Calibrator Survey (LBCS, Jackson et al. 2016, 2022), and use this to calibrate the international stations. In the case of Abell 2029, no calibrator source in the field was known, so one had to be manually found. After obtaining the calibration solutions for the international stations on the calibrator source, the solutions are transferred to the target source.

Due to the direction dependence of the calibration solutions, additional calibration has to be performed on the target source itself after transferring the previously derived solutions. To perform this final self-calibration (Van Weeren et al. 2021), the Default Preprocessing Pipeline (DPPP, Van Diepen et al. 2018) was employed to derive and apply updated calibration solutions, and WSCLEAN (Offringa et al. 2014) was employed to produce an image of the source. The self-calibration consisted of total electron content (TEC) and phase corrections, and depending on the brightness of the target source also of amplitude corrections. The core stations of LOFAR were combined into a single virtual station to narrow down the field of view and reduce interference from unrelated sources near the target. The angular resolution of the final images is on the order of 0.3 arcseconds at a central frequency of 144 MHz, with small variations between the different observations.

4.4.2 Chandra

The superb subarcsecond resolution of the *Chandra* satellite provides a good match to that achieved by LOFAR-VLBI observations. For this reason, we made use of archival *Chandra* Advanced CCD Imaging Spectrometer (ACIS) data to study the X-ray cavities associated with the AGN in our sample. Data were retrieved from the *Chandra* data archive[1] and processed with CIAO v4.12 and CALDB v4.9.0 starting from the `level=1` event file. Observing periods affected by background flares were removed by inspecting light curves extracted in the 0.5−7.0 keV band using the `deflare` task. When multiple ObsIDs were available, event files were combined with the `merge_obs` script. All images used for the analysis are exposure-corrected and were obtained in the 0.5−2.0 keV band. A summary of the ObsIDs used in this work together with the total net exposure time per cluster is reported in Table 4.3.

4.5 Results

4.5.1 Imaging

To study the radio lobes present in our sample, we have imaged all sources in our high-resolution (∼0.3 arcseconds) sample using WSClean with a Briggs robust parameter of -0.5 (Briggs 1995), as shown in Fig. 4.1. The images of the low-resolution (∼6 arcseconds) sample have mainly been sourced externally, with the Perseus cluster forming the only exception, as previously discussed in Sect. 4.3.

After producing the X-ray images, a Multi-Gaussian Expansion (Cappellari 2002) was used to subtract a smooth model of the ICM brightness distribution from the images to obtain the residual map, where the cavities are most clearly visible. This technique is particularly efficient in revealing surface brightness depressions like cavities, as demonstrated by, for example, Rafferty et al. (2013) and Bîrzan et al. (2020). Depending on the total photon count, the residuals were smoothed with a Gaussian function to reduce noise. In the case where background structures obfuscate the cavities, an unsharp mask was applied to flatten out the image while maintaining the cavity structures. The LOFAR images were overlaid on the X-ray residuals to correlate the radio lobes with the X-ray cavities, as shown in Fig. 4.2.

High-resolution sample

In this section we briefly describe the high-resolution radio images (see Fig. 4.1), radio/X-ray overlays (see Fig. 4.2), and spectral index maps (see Fig. 4.7) of individual clusters.

- **Perseus**: The high-resolution image of Perseus shows a dominant flat-spectrum central compact component surrounded by diffuse emission. The steeper-spectrum ($\alpha = -0.9$) jetted outflows from the AGN are visible toward the north and the south. The lingering steep-spectrum ($\alpha = -1.8$) emission

[1] `https://cda.harvard.edu/chaser`

Table 4.3: Summary of the *Chandra* observations processed for the X-ray residual maps presented in this paper.

Cluster name	Net exposure time (ks)	Observation ID
Perseus (NGC 1275)	1450	1513, 3209, 4289, 4946...4953, 6139, 6145, 6146, 11713...11716, 12025, 12033, 12036, 12037
Abell 2199	156	497, 498, 10748, 10803...10805
2A 0335+096	82	7939, 9792
MKW 3S	56	900
Abell 1795	1161	493, 494, 3666, 5286...5289, 6160, 6162, 6163, 10900, 12026, 12028, 12029 ,13106...13108, 13110, 13414 14268..14270, 15485...15487, 16432...16434, 16436, 16465, 17228, 17397...17399, 17401, 17405, 17408, 17683, 17685, 17686, 18423...18427, 18429, 18433, 19868...19870, 19877...19879, 19968, 19969, 20642...20644, 20651...20653, 21830...21832, 21839...21841, 22829...22831, 22838...22840, 24602, 24609...24611
Abell 1668	10	12877
Abell 2029	126	891, 4977, 6101, 10434...10437
3C 388	35	4756, 5295
ZwCl 2701	127	3195, 7706, 12903
MS 0735.6+7421	512	4197, 10468...10471, 10822, 10918, 10922
4C+55.16	94	1645, 4940
RX J1532.9+3021	107	1649, 1665, 14009
MACS J1720.2+3536	60	3280, 6107, 7225, 7718
MACS J1423.8+2404	133	1657, 4195

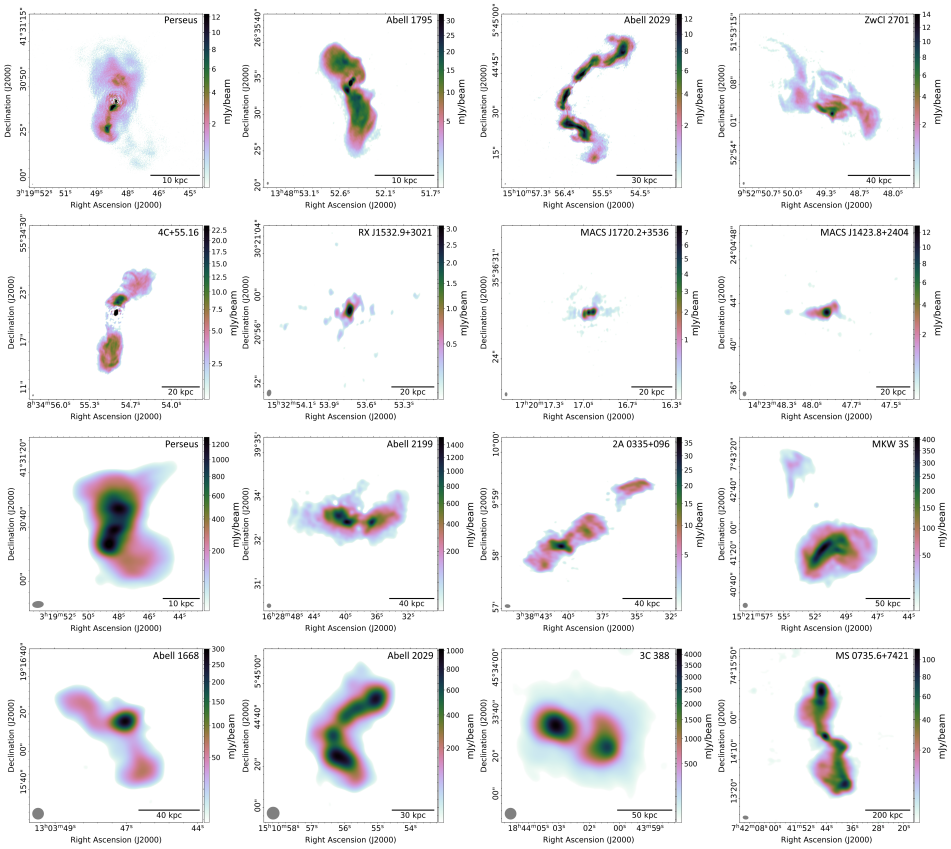

Figure 4.1: LOFAR images of all galaxy clusters our the sample. The top 8 panels show the high-resolution maps produced by including LOFAR's international stations and the bottom 8 panels show the low-resolution maps produced using only the Dutch part of the array. We note that Perseus and Abell 2029 are presented in both sections. The central dominant compact component in the Perseus cluster was peeled from the data for the low-resolution map for calibration purposes. The color maps range from three times the rms noise level to the peak brightness, except in the cases of Perseus, Abell 1795 and 4C+55.16, for which the peak brightness of the lobes was used due to the otherwise dominant central compact component. The scale bar in the bottom right corner of each panel measures the listed length at the redshift of the respective clusters. The beam is indicated in gray in the bottom left corner of each panel.

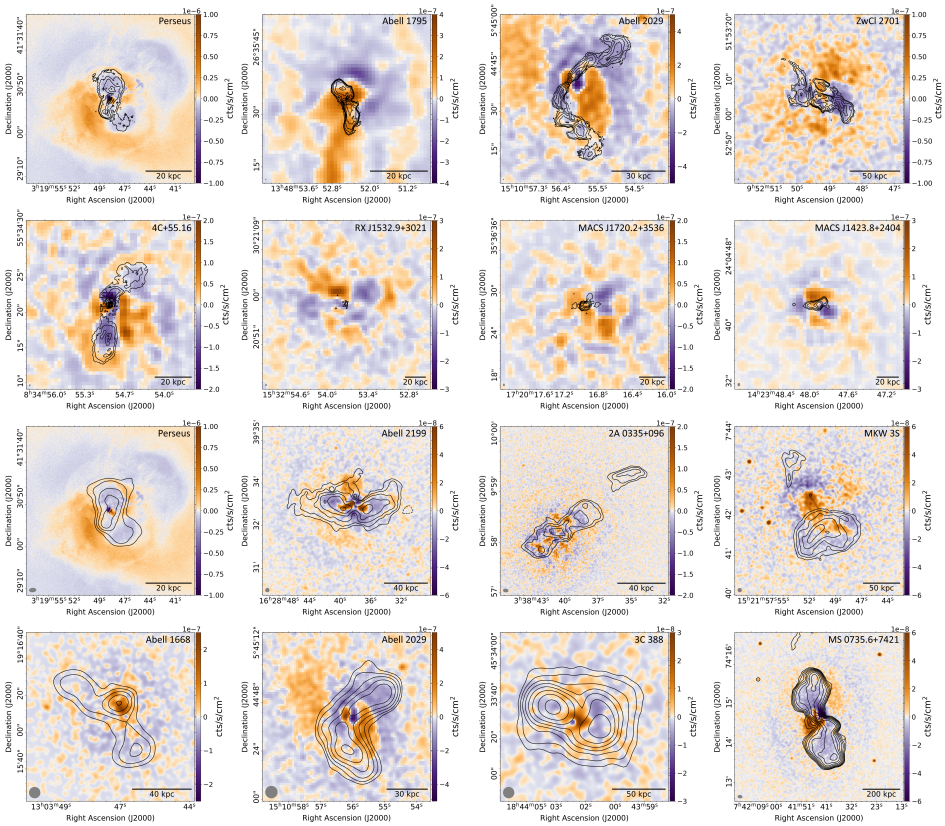

Figure 4.2: Residuals from the *Chandra* X-ray images after subtracting a smooth model of the ICM surface brightness. The top 8 panels show the X-ray residual maps corresponding to the high-resolution sample and the bottom 8 panels show the X-ray residual maps corresponding to the low-resolution sample. We note that Perseus and Abell 2029 are presented in both sections. The orange and purple colors indicate regions with surface brightness excess and deficiency, respectively. The black contours indicate the radio emission, and are drawn in increments of factors of 2, starting at 5 times the rms noise level. The scale bar in the bottom right corner of each panel measures the listed length at the redshift of the respective clusters. The beam is indicated in gray in the bottom left corner of each panel.

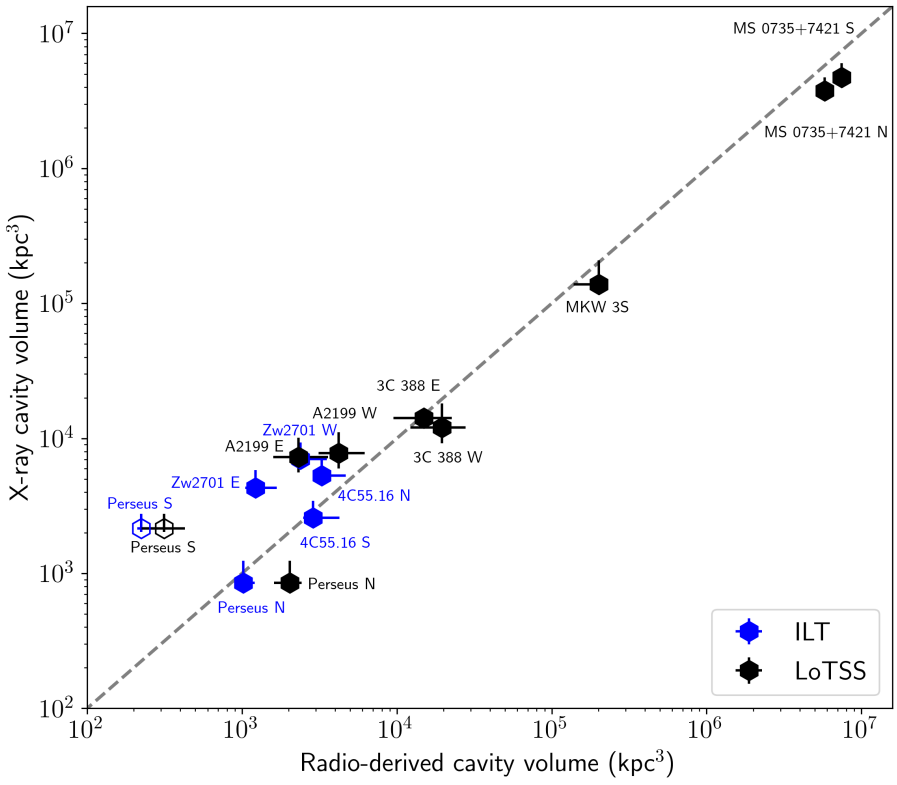

Figure 4.3: Radio-estimated cavity volumes versus X-ray-estimated cavity volumes. The blue data points indicate the measurements derived using high-resolution observations, while the black data points indicate the measurements derived using low-resolution observations. The dashed line indicates the line of equality. The open markers indicate the cavities for which the radio lobe does not visually match the cavity as observed in the X-ray.

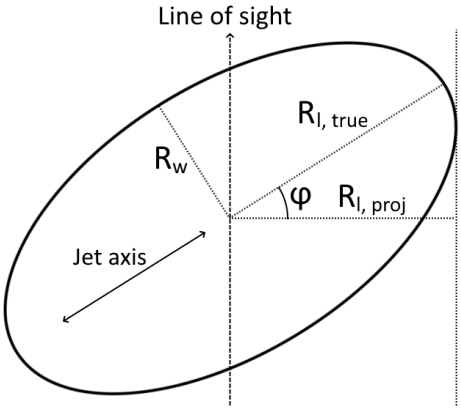

Figure 4.4: Schematic of the construction used to estimate the uncertainties on the cavity volume measurements.

of a previous outburst can still be seen toward the southwest of the center, similar to as previously reported based on VLA and MERLIN observations by Pedlar et al. (1990) and Gendron-Marsolais et al. (2017, 2020). From the X-ray overlay, it is clear that all detected radio emission is coincident with an X-ray depression (Fabian et al. 2000). The X-ray residuals, the radio morphology, and the spectral indices strongly suggest that the AGN experienced at least two distinct outbursts.

- **Abell 1795**: There are two clear radio lobes visible toward the north and the south. As previously observed with the VLA by Van Breugel et al. (1984), it appears that the radio jet is emitted along the northeast to southwest direction, and both jets then bend away toward the north and south, respectively. The spectral index gradient along the lobe clearly shows the direction of the outflow. There is no clear correlation between these radio lobes and an X-ray depression, although this is likely to be at least in part due to the presence of a long X-ray filament stretching from the center of the cluster about 40 arcseconds toward the south (Fabian et al. 2001), which can affect both the cavity structure and our ability to detect it.

- **Abell 2029**: The radio structure of Abell 2029 as detected with LOFAR shows an FR I-type morphology (Fanaroff & Riley 1974) with two radio filaments toward the northwest and the south, similar to as observed by Taylor et al. (1994) using the VLA. Similar as to in Abell 1795, the spectral index gradually steepens toward the older regions of the outflows. The radio lobes do not clearly coincide with depressions in the X-ray brightness, although the spiral pattern detected in the X-ray residuals (Clarke et al. 2004) may hinder a clear detection of cavities in a comparable manner as with Abell 1795. We also note the presence of multiple filamentary structures throughout the radio outflows.

- **ZwCl 2701**: The low-frequency radio structure of ZwCl 2701 shows complex features previously unreported in literature. A mildly bright compact component with a peak brightness of 14 mJy is located in the central region, surrounded by diffuse emission. An apparently separated filamentary structure is located approximately 6 arcseconds north of the core. Two radio lobes previously reported by Bîrzan et al. (2020) can be found approximately 7 arcseconds east and west of the core, where they coincide with the cavities previously also observed in the X-ray by Vagshette et al. (2016). An additional tail-like structure is seen just north of the eastern lobe, but due to the morphology of this structure and the lack of coinciding X-ray brightness depression, it is assumed that this structure is not a constituent of the radio lobe.

- **4C+55.16**: The structure of 4C+55.16 consists of a bright compact flat-spectrum component in the center with two steeper-spectrum radio lobes extending about 9 arcseconds in the northwestern and southern directions, similar to as observed by Xu et al. (1995). The southern lobe coincides with a very clear cavity with an X-ray bright rim almost fully surrounding the cavity. The northern radio lobe also coincides with a cavity, but the extent of this cavity is less pronounced (Hlavacek-Larrondo et al. 2011).

- **RX J1532.9+3021**: Only a faint compact radio component can be detected in the LOFAR map of RX J1532.9+3021, similar as to previously reported by Yu et al. (2018). Although the X-ray residuals show two clear brightness depressions toward the east and west of the cluster (Hlavacek-Larrondo et al. 2013), no coincident radio emission is detected.

- **MACS J1720.2+3536**: The LOFAR map reveals three faint compact components located within one arcsecond of one another, consistent with observations by Yu et al. (2018) using the VLA. It is unclear what the physical nature is of these components, but it is not assumed that the two outer components represent radio lobes. Hlavacek-Larrondo et al. (2012) report the detection of a clear cavity north of the core and a fainter cavity toward the south, but no radio emission is found to be coincident with those regions.

- **MACS J1423.8+2404**: This cluster is the most distant object in our sample, with a redshift of $z = 0.545$ (Limousin et al. 2010). The structure of MACS J1423.8+2404 shows a central faint compact component with two elongations toward the east and northwest. A hint of this eastern extension was also reported by Yu et al. (2018) based on 1.5 GHz VLA observations. These extensions may be related to the radio jets, as two X-ray brightness depressions are detected roughly in the same location, but these cannot be relied on to provide a description of the radio lobes due to their low significance.

Low-resolution sample

In this section we briefly describe the low-resolution radio images (see Fig. 4.1) and overlays (see Fig. 4.2) of individual clusters. Low-resolution LOFAR maps of Abell 2199, 2A 0335+096, MKW 3S, Abell 1668 and MS0735.6+7421 were previously published by Bîrzan et al. (2020). In addition, the low-resolution maps presented in Fig. 4.1 of 2A 0335+096 and MS 0735.6+7421 were obtained from Ignesti et al. (2022) and Biava et al. (2021), respectively. Finally, a low-resolution LOFAR map of 3C 388 was already previously published by Brienza et al. (2020).

- **Perseus**: To aid with the calibration of the data and obtain a clear view of the diffuse emission, the central dominant compact component was peeled from the data based on the high-resolution imaging. The northern and southwestern lobes are still clearly resolved. The southwestern lobe is more prominently detected in the low-resolution map and completely fills the X-ray cavity.

- **Abell 2199**: The LoTSS map reveals two extended radio lobes located toward the east and west of the core of the cluster, similar to as previously observed at 408 MHz with the One-Mile Telescope (OMT) at Cambrige by Parker & Kenderdine (1967). Similar to as observed with the OMT, no central compact component can be detected in the LOFAR map, although this component was present at higher frequencies in previously reported Westerbork Synthesis Radio Telescope maps (Jaffe & Perola 1974) and VLA maps (Burns et al. 1983), suggesting that the core is strongly self-absorbed. Despite the chaotic structure in the X-ray residuals, it is clear that the radio lobes coincide with the observed cavities, as also previously reported by Johnstone et al. (2002).

- **2A 0335+096**: As reported by Ignesti et al. (2022), the radio structure of this cluster at 144 MHz consists predominantly of diffuse emission. Although no compact central component is detected, the central region shows a bright extended component. Two diffuse radio lobes are located toward the northwest and southeast of the center. A diffuse component is located further toward the northwest, and is apparently separated from the rest of the cluster. It is unclear whether this structure is a radio lobe associated with a previous outburst of the AGN, or if it has a different physical nature. The X-ray residuals show a chaotic structure (Mazzotta et al. 2003; Sanders et al. 2009), which hampers a clear identification of the cavities.

- **MKW 3S**: Similar to as reported by Mazzotta et al. (2002), a single bright extended radio lobe toward the south of the core dominates the radio structure of MKW 3S. An additional fainter diffuse component is located toward the north, but no compact emission associated with the AGN is detected. The X-ray residuals show a cavity coincident with the southern radio lobe, but although there is a surface brightness depression toward the north, this is not found to be directly coincident with the northern radio emission.

- **Abell 1668**: Two radio lobes toward the northeast and south are clearly detected in the LoTSS map. These radio lobes are directly connected to a central compact component. Pasini et al. (2021) report two possible X-ray cavities toward the northwest, but these do not coincide with the observed radio emission. The lack of clear cavity detections may in part be due to the low sensitivity of the available X-ray observations.

- **Abell 2029**: From the low-resolution radio map of Abell 2029 we see the same radio lobes toward the northwest and south of the core. However, whereas both our high-resolution map and the previously reported VLA maps (Clarke et al. 2004) show more bent lobe structures, these features are not resolved in the low-resolution map. Similar as with the high-resolution map, the spiral pattern detected in the X-ray residuals hinders a clear identification of cavities coincident with the radio lobes.

- **3C 388**: Similar to as observed with the OMT by Mackay (1969) and Branson et al. (1972), the LoTSS map shows two bright radio lobes located toward the east and west of the core of the cluster. No central compact component can be clearly detected. Both of the radio lobes are coincident with X-ray depressions (Kraft et al. 2006), although the low sensitivity of the X-ray observations does not enable these cavities to be studied in detail.

- **MS 0735.6+7421**: As reported by Biava et al. (2021), the LOFAR map of MS 0735.6+7421 shows two bright radio lobes extending toward the north and south of a central compact component. This structure is mainly similar to as observed with the VLA by Cohen et al. (2005). The X-ray residuals show cavities directly coincident with the entire extent of the radio emission, and feature clear rims fully surrounding the cavities (McNamara et al. 2005).

4.5.2 Analysis

From our LOFAR images, we measure the size of the radio lobes assuming an ellipsoidal shape. The major and minor axes of the radio lobes are estimated by eye, preferably based on the CLEAN models, to optimally incorporate the identification of the different components present in the images. In the situation where a radio lobe does not feature clearly defined edges (e.g., 3C 388), the dimensions are estimated based on the steepest gradients surrounding the lobe. Due to the low surface brightness, the lobes could not be reliably identified for three sources in our sample: RX J1532.9+3021, MACS J1720.2+3536 and MACS J1423.8+2404. For this reason, these three sources have been excluded from further analysis. This will be further discussed in Sect. 4.6.2.

One of the most fundamental differences between the hybrid method and the purely X-ray-based method is that the cavity volume is now derived based on radio observations. To confirm that these measurements are reliable, we compare the X-ray-derived estimates for the cavity volume, as found in the literature, to our radio-derived estimates, as shown in Fig. 4.3. As the dominant uncertainty of the volume measurements is generally due to projection effects, we quantify

this uncertainty through a Monte Carlo approach where we randomly select an orientation for the cavity and calculate which true volume would correspond to the projected dimensions of the cavity. Assuming a projected semi-major length along the jet axis $R_{\mathrm{l,\ proj}}$ and a projected semi-minor axis perpendicular to the jet axis R_{w}, the deprojected semi-major axis of the cavity can be calculated as

$$R_{\mathrm{l,\ true}} = \sqrt{\frac{R^2_{\mathrm{l,\ proj}} - R^2_w \sin^2\varphi}{\cos^2\varphi}}, \tag{4.4}$$

where φ is the angle between the true jet axis and the projected plane. The semi-minor axis of the cavity is independent of the orientation. Given the deprojected semi-major axis, the cavity volume can be calculated as $V = \frac{4}{3}\pi R_{\mathrm{l,\ true}} R^2_{\mathrm{w}}$. A schematic of this construction is shown in Fig. 4.4. For consistency, we recalculate the uncertainties on the cavity volumes of the literature X-ray estimates as well using the same method. In addition, we implement an uncertainty on the projected dimensions of the cavity. For literature values, we adopt an uncertainty on the order of the most precise digit if the uncertainty is not published (e.g., an uncertainty of 1 kpc on 13 kpc and 0.1 kpc in the case of 13.0 kpc). For our radio estimates, we assume an uncertainty of a quarter of the synthesized beam width. The final cavity volume estimates are then calculated as the median of the cavity volume probability distribution function, with the 68.3% confidence interval serving as the projection-based uncertainty.

In some cases, a direct comparison between the X-ray cavity and the observed radio lobes is not possible. For instance, Rafferty et al. (2006) only report one cavity in the case of Abell 1795 and Abell 2029, leaving it unknown which radio lobe should match this cavity. Based on the significant difference in the reported distance to the center between the X-ray cavity and the radio lobe, it is safe to conclude that these do not correspond to the same structure. Similarly, although two cavities are reported in 2A 0335+096, the perturbed structure at the core hampers a certain match between the X-ray cavities and the radio lobes. Finally, in the case of Abell 1668, cavities are detected toward the north and northwest of the center, whereas the radio lobes are detected at larger radii toward the south and northeast. Due to these issues, the aforementioned systems are excluded from Fig. 4.3.

Following this comparison, we proceed by calculating the cavity power corresponding to the observed radio lobes. For this calculation, we follow the same Monte Carlo procedure as before, where we assume a random orientation and use the resulting true cavity volume and distance to the center of the cluster to calculate the cavity volume. For the ICM pressure, we assume the same values used in literature for the X-ray cavity power estimates and do not vary this with radius as the pressure profiles are generally not published.

For the consistency of the uncertainties on the data, we also calculate the X-ray cavity power and its uncertainty and confirm that these estimates match the published values. The cavity power estimates based only on X-ray observations and the relevant intermediate data are summarized in Table 4.4. Similarly, the cavity power estimates based on our hybrid X-ray–radio method and the rele-

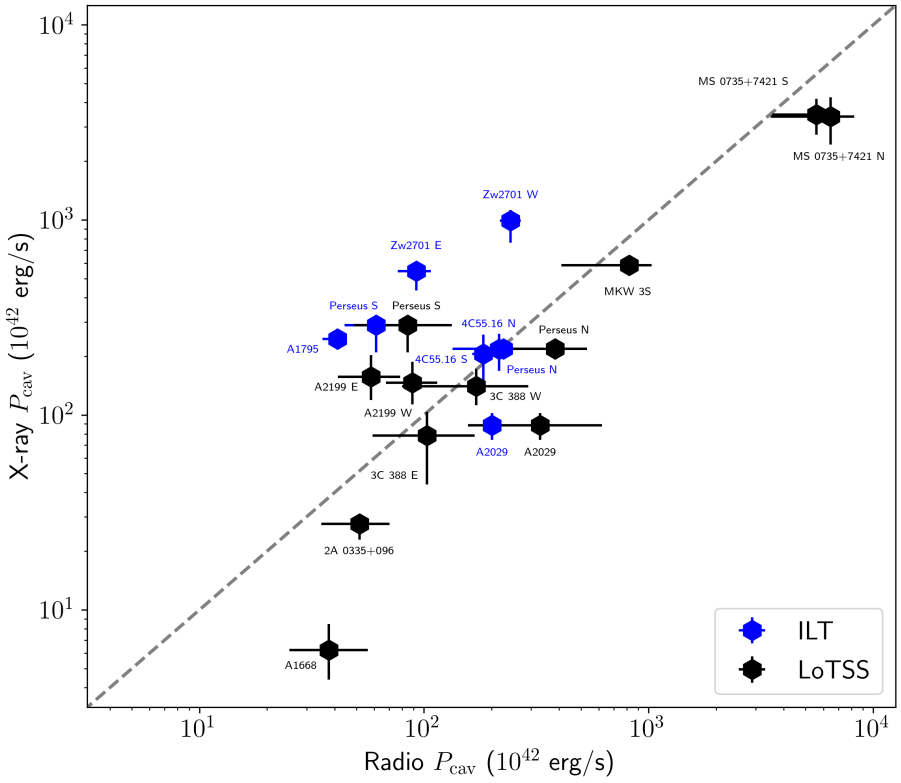

Figure 4.5: Hybrid X-ray–radio cavity power measurements versus the purely X-ray-based cavity power estimates. The blue data points indicate the measurements derived using high-resolution observations, while the black data points indicate the measurements derived using low-resolution observations.

vant intermediate data are summarized in Table 4.5. The comparison between the hybrid X-ray–radio measurements and the purely X-ray-based cavity power measurements is shown in Fig. 4.5.

As a final consistency check, we plot our hybrid cavity power estimates as a function of cluster redshift to confirm whether there is any systematic effect between our hybrid estimates and the X-ray-based estimates found in the literature, as shown in Fig. 4.6. As the two data sets trace the same redshift dependence, it is clear that there is no systematic bias.

4.6 Discussion

Constraining the amount of mechanical feedback injected into the ICM by the AGN has not only been considered to be a vital step in understanding the for-

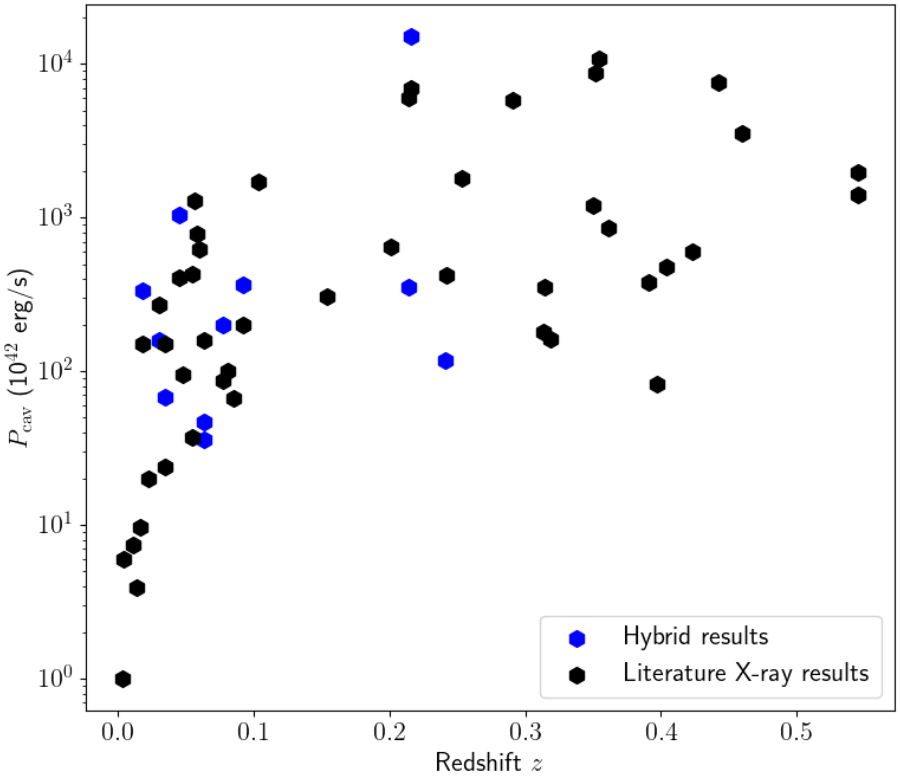

Figure 4.6: Cavity power as a function of redshift. The blue data points indicate the cavity power measurements derived using our hybrid method, while the black data points indicate the cavity power estimates found in Rafferty et al. (2006) and Hlavacek-Larrondo et al. (2012). From Hlavacek-Larrondo et al. (2012) we only select the cavities indicated as clearly detected.

Table 4.4: Properties of the cavities in our sample derived using the traditional X-ray method.

(a) Cluster name	(b) p (keV/cm^3)	(c) R_l (kpc)	(d) R_w (kpc)	(e) R (kpc)	(f) V (kpc^3)	(g) t_buoy (10^7 yr)	(h) P_cav (10^{42} erg/s)	(i) Ref.
Perseus (N)	0.4478	8.2	4.7	6.5	850^{+390}_{-80}	$1.0^{+0.7}_{-0.1}$	218^{+19}_{-26}	(1)
Perseus (S)	0.387	9.1	7.3	9.4	2160^{+610}_{-130}	$1.7^{+1.3}_{-0.3}$	289^{+37}_{-80}	(1)
Abell 2199 (E)	0.1251	15	10	19	7250^{+2890}_{-1650}	$3.1^{+2.2}_{-0.5}$	157^{+46}_{-38}	(1)
Abell 2199 (W)	0.1205	16	10	21	7800^{+3280}_{-1800}	$3.5^{+2.4}_{-0.6}$	146^{+41}_{-33}	(1)
2A 0335+096	0.1291	9.3	6.5	23	1790^{+670}_{-140}	$5.5^{+3.9}_{-0.9}$	$26.6^{+3.2}_{-4.7}$	(1)
2A 0335+096	0.1125	4.8	2.6	28	155^{+71}_{-21}	$10.1^{+6.6}_{-1.4}$	0.98 ± 0.12	(1)
MKW 3S	0.0675	54	23	59	138200^{+70100}_{-19800}	$9.1^{+5.7}_{-1.2}$	586^{+62}_{-58}	(1)
Abell 1795	0.242	19	7.2	19	4720^{+2530}_{-580}	$2.8^{+1.7}_{-0.4}$	245^{+32}_{-29}	(1)
Abell 1668 (N)	0.0836	2.6	1.5	3.5	$27.8^{+13.7}_{-7.3}$	$0.63^{+0.41}_{-0.13}$	$2.14^{+0.67}_{-0.53}$	(2)
Abell 1668 (NW)	0.0836	2.4	2.4	3.5	$57.5^{+20.1}_{-16.1}$	$0.67^{+0.50}_{-0.15}$	$4.01^{+2.12}_{-1.76}$	(2)
Abell 2029	0.3612	13	7.2	32	3190^{+1450}_{-420}	$7.6^{+5.0}_{-1.1}$	$88.3^{+14.1}_{-14.0}$	(1)
3C 388 (E)	0.0436	15	15	27	14110^{+2510}_{-2220}	$4.5^{+3.8}_{-0.8}$	$78.2^{+25.6}_{-34.2}$	(1)
3C 388 (W)	0.0486	24	10	21	12040^{+6130}_{-2860}	$2.3^{+1.5}_{-0.4}$	140^{+33}_{-28}	(1)
ZwCl 2701 (E)	0.7802	12.25	8.75	18.9	4310^{+1520}_{-420}	$3.6^{+2.6}_{-0.5}$	545^{+69}_{-110}	(3)
ZwCl 2701 (W)	0.8364	14.0	10.5	19.25	7030^{+2280}_{-600}	$3.4^{+2.6}_{-0.5}$	993^{+128}_{-228}	(3)
MS 0735.6+7421 (N)	0.0469	110	87	160	$3766000^{+954000}_{-472000}$	$29.6^{+17.5}_{-5.2}$	3390^{+860}_{-960}	(1)
MS 0735.6+7421 (S)	0.409	130	89	180	$4726000^{+1289000}_{-539000}$	$32.1^{+17.5}_{-5.2}$	3470^{+700}_{-730}	(1)
4C+55.16 (NW)	0.3135	13	9.4	22	5290^{+1850}_{-620}	$4.4^{+3.2}_{-0.7}$	217^{+44}_{-49}	(1)
4C+55.16 (S)	0.4338	10	7.5	16	2590^{+850}_{-360}	$3.2^{+2.3}_{-0.6}$	205^{+52}_{-55}	(1)

Notes. Columns: (a) cluster name; (b) ICM pressure; (c) cavity radius along the jet axis; (d) cavity radius perpendicular to the jet axis; (e) cavity distance from the AGN core; (f) cavity volume; (g) buoyancy timescale; (h) cavity power; (i) reference

References. (1) Rafferty et al. (2006); (2) Pasini et al. (2021); (3) Vagshette et al. (2016)

Table 4.5: Properties of the cavities in our sample derived using the hybrid X-ray–radio method. The horizontal line separates the clusters that are studied at high resolutions (top half) from the clusters that are studied at low resolutions (bottom half).

(a) Cluster name	(b) $R_{\rm l}$ (kpc)	(c) $R_{\rm w}$ (kpc)	(d) R (kpc)	(e) V (kpc^3)	(f) $t_{\rm buoy}$ (10^7 yr)	(g) $P_{\rm cav}$ (10^{42} erg/s)	(h) Ref.
Perseus (N)	6.7	5.9	6.6	1020^{+190}_{-30}	$1.2^{+1.0}_{-0.2}$	226^{+36}_{-92}	(1)
Perseus (S)	4.3	3.4	4.5	223^{+64}_{-12}	$0.83^{+0.65}_{-0.13}$	$61.3^{+7.6}_{-17.0}$	(1)
Abell 1795 (N)	2.2	2.3	3.5	$48.5^{+8.2}_{-6.6}$	$0.67^{+0.59}_{-0.11}$	$10.5^{+2.7}_{-5.1}$	(1)
Abell 1795 (S)	5.5	2.3	4.7	140^{+72}_{-19}	$0.65^{+0.42}_{-0.09}$	$30.7^{+3.1}_{-2.8}$	(1)
Abell 2029 (N)	9.0	3.9	10.8	644^{+328}_{-87}	$1.8^{+1.1}_{-0.2}$	$76.5^{+7.3}_{-6.8}$	(1)
	9.2	5.0	31.6	1100^{+510}_{-120}	$8.8^{+5.7}_{-1.2}$	$26.1^{+2.4}_{-2.9}$	(1)
Abell 2029 (S)	6.1	2.7	8.2	217^{+107}_{-35}	$1.4^{+0.9}_{-0.2}$	$31.9^{+4.1}_{-3.7}$	(1)
	19.5	3.9	27.1	1480^{+850}_{-210}	$4.7^{+2.9}_{-0.6}$	$66.7^{+5.1}_{-4.9}$	(1)
ZwCl 2701 (E)	8.4	5.6	22.3	1220^{+460}_{-170}	$5.8^{+4.1}_{-0.8}$	$92.6^{+14.6}_{-16.0}$	(1)
ZwCl 2701 (W)	12.7	6.3	23.3	2390^{+1150}_{-330}	$4.7^{+3.1}_{-0.6}$	243^{+27}_{-25}	(1)
4C+55.16 (NW)	12.6	7.4	16.0	3270^{+1410}_{-410}	$2.7^{+1.8}_{-0.4}$	216^{+27}_{-29}	(1)
4C+55.16 (S)	13.5	6.7	20.9	2880^{+1380}_{-400}	$3.9^{+2.5}_{-0.5}$	184^{+21}_{-20}	(1)
Perseus (N)	7.2	8.6	6.9	2040^{+380}_{-430}	$1.2^{+0.8}_{-0.2}$	384^{+148}_{-189}	(1)
Perseus (S)	4.4	4.1	4.3	314^{+115}_{-89}	$0.81^{+0.61}_{-0.21}$	$84.7^{+48.2}_{-36.1}$	(1)
Abell 2199 (E)	12.8	6.0	16.2	2320^{+1280}_{-730}	$2.6^{+1.7}_{-0.4}$	$58.1^{+20.1}_{-16.8}$	(2)
Abell 2199 (W)	14.1	7.8	19.2	4210^{+1990}_{-1090}	$3.2^{+2.1}_{-0.5}$	$88.6^{+26.1}_{-21.0}$	(2)
2A 0335+096 (NW)	10.2	9.4	27.0	3960^{+1210}_{-940}	$6.9^{+5.5}_{-1.2}$	$40.5^{+17.2}_{-15.6}$	(3)
2A 0335+096 (SE)	5.5	7.8	22.9	1200^{+510}_{-430}	$7.1^{+3.5}_{-1.3}$	$11.1^{+7.2}_{-5.8}$	(3)
MKW 3S	25.4	46.4	50.0	201800^{+29700}_{-63300}	$10.0^{+3.7}_{-1.1}$	818^{+213}_{-409}	(2)
Abell 1668 (NE)	13.0	7.4	31.0	3530^{+2540}_{-1620}	$7.4^{+4.9}_{-1.4}$	$21.1^{+14.0}_{-9.6}$	(2)
Abell 1668 (S)	9.9	9.3	34.0	3630^{+2000}_{-1430}	$9.9^{+6.9}_{-2.0}$	$16.6^{+12.0}_{-8.1}$	(2)
Abell 2029 (N)	21.8	4.3	21.4	2170^{+3190}_{-1640}	$3.3^{+1.9}_{-0.7}$	132^{+175}_{-100}	(2)
Abell 2029 (S)	26.0	4.7	22.3	3140^{+4190}_{-2240}	$3.2^{+1.8}_{-0.7}$	197^{+233}_{-140}	(2)
3C 388 (E)	17.3	13.7	23.3	14900^{+7700}_{-5400}	$3.4^{+2.5}_{-0.8}$	103^{+65}_{-44}	(2)
3C 388 (W)	12.8	20.7	21.6	19500^{+8300}_{-7300}	$3.3^{+1.5}_{-0.8}$	171^{+120}_{-91}	(2)
MS 0735.6+7421 (N)	111	112	138	$5770000^{+700000}_{-660000}$	$23.8^{+16.9}_{-3.8}$	6470^{+1770}_{-2980}	(4)
MS 0735.6+7421 (S)	128	115	173	$7450000^{+920000}_{-780000}$	$30.4^{+19.0}_{-4.5}$	5580^{+1310}_{-2030}	(4)

Notes. Columns: (a) cluster name; (b) cavity radius along the jet axis; (c) cavity radius perpendicular to the jet axis; (d) cavity distance from the AGN core; (e) cavity volume; (f) buoyancy timescale; (g) cavity power; (h) reference for radio observations

References. (1) This paper; (2) LoTSS; (3) Ignesti et al. (2022); (4) Biava et al. (2021)

mation and evolution of galaxy clusters, but has also in and of itself been an observational challenge. Although from a physical perspective there is a natural expectation for the radio lobes to paint the same picture as the X-ray cavities, quantifying the amount of mechanical feedback has mainly been performed using X-ray observations. Attempts to enable radio observations to measure the quantity of mechanical feedback have produced significant correlations, but have never made radio observations able to compete with their X-ray counterpart. In this paper, we have described a hybrid method of measuring the quantity of mechanical feedback based on a combination of X-ray and radio observations, and have performed this method on a sample of 14 galaxy clusters for the purpose of verifying whether this new method can be considered to provide reliable results at 144 MHz.

4.6.1 General performance

First of all, we have measured the volume of the radio lobes as observed with LOFAR and compared this volume to the cavity volume estimates derived from X-ray observations. From a physical perspective, there is the expectation that these two volumes should be exactly equal. Therefore, the two measurements must agree within the uncertainties, but that is not always true in our sample. This implies that either the uncertainties are systematically underestimated, or that the simple model that all radio lobes produce clear cavities is invalid. The truth is likely somewhere in the middle. The assumption that the uncertainties on the cavity volume and cavity power are solely determined by projection effects was always known to be oversimplified, but better methods to quantify the uncertainty were lacking. Likewise, the simple 'balloon' model in which the radio lobes and ICM are perfectly mutually exclusive is also due a critical review. In reality, additional structures like backflows can make it difficult to distinguish what constitutes as the radio lobe (see, e.g., Timmerman et al. 2022b). Also, the ICM will mix with the jetted outflows both due to entrainment along the jets as well as due to turbulence within the radio lobes. This underlines the importance of high-quality observations. For future practical purposes, it will be most useful to assume the scatter we observe between our radio-derived cavity measurements and the X-ray cavity measurements ($\sigma = 0.30$ dex) as a systematic uncertainty on these measurements. For direct comparison with literature results, we maintain the projection-derived uncertainties for the remainder of this paper.

Using the volume of the cavities derived based on LOFAR observations in combination with the X-ray-derived ICM pressure, we derive the cavity power of the AGN. In general, this method produces a relatively tight correlation with the purely X-ray-derived estimates, with a scatter in the cavity power measurements of only 0.44 dex. This is highly competitive with previous attempts to derive a correlation between the radio properties and the cavity power in galaxy clusters, which resulted in scatters of at least 0.8 dex based on monochromatic radio powers (Bîrzan et al. 2008; Kokotanekov et al. 2017) and a scatter of 0.65 dex based on bolometric radio luminosities of only the radio lobes (Bîrzan et al. 2008). In addition, there appears to be no significant systematic difference between the

hybrid X-ray–radio method and the purely X-ray-based method. However, it is valuable to explore deeper into the results and investigate exactly how the hybrid X-ray–radio method performs under different circumstances.

In general, the best correlation is seen in systems where both the X-ray cavities are clearly detected and their sizes can be well constrained. If we classify our sample using the figure of merit (FOM) system from Rafferty et al. (2006), where cavities fully surrounded by bright rims score a 1, cavities partially surrounded by bright rims score a 2, and cavities with either a faint rim or no rim score a 3, we can quantify how strong this effect is. We assume the FOMs published by Rafferty et al. (2006) for this, and classify Abell 1668 (FOM=3) and ZwCl 2701 (FOM=2) ourselves using the same criteria, as for these systems we use the cavity measurements from Pasini et al. (2021) and Vagshette et al. (2016), respectively. There is only one system classified to have a FOM of 1 (Perseus), which we discuss in more detail later. Comparing the cavity power measurements of cavities with FOM=2 (N=10) and FOM=3 (N=6), we find that the FOM=2 systems show a scatter of 0.34 dex, while the FOM=3 systems show a scatter of 0.49 dex instead. This suggests that in some instances, using the radio lobes to measure the cavity volume can provide a better estimate of the cavity power than the X-ray cavities.

By comparing the cavity power estimates as a function of redshift between the traditional method and the hybrid method, we confirm that the resulting distributions are in good agreement, allowing the hybrid method to be used to study a sample of galaxy clusters. This is particularly important as this enables the hybrid method to be confidently used at higher redshifts as well, where the X-ray cavities can in general not be detected due to sensitivity limitations. In the event that the hybrid method is applied to clusters at higher redshifts, where the X-ray observations may not be able to aid with the identification of the radio lobes, the uncertainties on the dimensions of the radio lobes may increase, depending on the exact morphology and brightness. However, as the radio lobes are in general clearly identifiable, this is not expected to cause significantly increased uncertainties in general. This also applies to clusters where the central ICM pressure is obtained based on Sunyaev-Zel'dovich measurements instead of X-ray observations.

At higher redshifts, the surface brightness of the radio lobes will naturally decrease, resulting in a soft limit on measurements of the cavity power, also depending on the scale of the lobes. However, clear detection of the lobes in the radio galaxy 4C 43.15 at $z = 2.4$ by Sweijen et al. (2022) and further detections of the radio lobes in the protoclusters 4C 41.17 ($z = 3.8$), B2 0902+34 ($z = 3.4$) and 4C 34.34 ($z = 2.4$) by Cordun et al. (in prep.) provide an encouraging perspective and demonstrate the feasibility of detecting radio lobes with the ILT even at high redshifts.

4.6.2 Performance per system

To better understand how the method performs, it is useful to consider the separate systems in more detail. For three systems (RX J1532.9+3021, MACS J1720.2+3536 and MACS J1423.8+2404), the radio observation did not reveal sufficient detail and structure to be able to derive a radio lobe volume. This suggests that the

hybrid X-ray–radio method is mostly viable for sources brighter than ∼100 mJy at 144 MHz. Such a limit on radio brightness is likely to introduce selection effects, especially toward higher redshifts, so it is important to be aware of this.

Proceeding with the sources which are well detected in our LOFAR observations, one of the most interesting examples is the Perseus cluster. Whereas the cavity power predicted by the X-ray method and the hybrid X-ray–radio method agree very well for the northern lobe, the southern lobe shows a significant difference. In the radio map, the southern lobe appears to consist of two distinct components: a bright compact component directly south of the AGN and a faint extended component toward the southwest of the AGN. Comparing our LOFAR map with deep VLA imaging at 1.5 GHz (Gendron-Marsolais et al. 2021) reveals a notable difference in the spectral index, with the bright compact component featuring an average spectral index of $\alpha = -1.2$ and the faint extended component featuring a spectral index of $\alpha = -1.7$. This suggests that the extended component is much older and likely corresponds to a previous outburst of the AGN. As the Perseus cluster is the lowest-redshift cluster in our sample, the faint component can be reasonably well detected in our radio maps, but this would likely not hold at higher redshifts. In the X-ray map, the two components are difficult to distinguish, leading to the cavity volume being estimated based on the combination of the two components. If the second component cannot be clearly detected using radio observations, this would lead to a significant discrepancy between the resulting cavity power measurements. We note that this situation can occur in any system where an old episode of AGN activity can still be traced through its cavity in the ICM, as the magnetized plasma of the radio lobe will only remain visible at radio wavelengths for a limited period. Synchrotron-emitting cosmic-ray electrons generally experience lifetimes of $\lesssim 10^8$ years (Feretti et al. 2012; Van Weeren et al. 2019), which may cause these to decay within the lifespan of older ICM cavities (see Tables 4.4 and 4.5).

Based on the radio morphology of the jetted outflows of the AGN, we note that our assumption that the radio lobes propagate radially outwards from the center of the cluster is not always strictly true. In the case of Abell 2029, it is particularly clear that the jetted outflows can bend away from their initial direction, but similar structures are also present in Abell 1795 and MS 0735.6+7421. Because of this jet bending, the assumption that the age of a cavity is only a function of the radial distance starts to fail. However, we estimate that this effect is relatively negligible in comparison to the other contributions to the overall uncertainty on the cavity power measurements.

In two instances (Abell 1795 and 2A 0335+096) we observe that the ICM as observed in the X-ray regime features such complex structures that this affects the identification and description of the cavities. Unless the cavities are very clearly present in the image, they are generally identified by subtracting a smooth model of the ICM brightness profile from the image, which causes the cavities to appear as negative regions. However, the presence of additional structure can affect the fitting of a brightness profile and thereby result in unreliable cavity detections. In these instances, relying on the volume of the radio lobes may be preferred over the X-ray cavity volume.

Similarly, there are clusters where even after model subtraction, the cavities are not apparently obvious among the residuals. For example, both the Abell 1668 and Abell 2029 systems have been reported to feature cavities, but only at low significance (Rafferty et al. 2006 and Pasini et al. 2021, respectively). This demonstrates that even in more relaxed clusters, the radio lobes may provide the most accurate estimates of the cavity sizes.

4.6.3 Comparing low- and high-resolution imaging

As two sources in our high-resolution sample (Perseus and Abell 2029) are sufficiently extended to also be studied at an angular resolution of ∼6 arcseconds, we are able to compare the effect of angular resolution on the cavity power estimates. In principle, the expectation is that there should be no dependency on angular resolution assuming that the deconvolved size of the radio lobe is estimated. However, we do observe that the low-resolution maps in general result in a higher cavity power estimate.

In the case of Abell 2029, our high-resolution map reveals a complex structure which is difficult to recover from the low-resolution map. We expect that the lobe volume is overestimated in our low-resolution map as the complex structure is smoothed out. The Perseus cluster is a different case, as both the northern and the southern lobes appear smooth and ellipsoidal in shape. For the sake of consistency and comparison, we have chosen to only consider the bright compact component south of the AGN instead of including the faint extended component toward the southwest. This sustains the discrepancy observed with the X-ray cavities but allows for a more direct comparison between the high-resolution and low-resolution maps. It is uncertain why the low-resolution map indicates a larger lobe volume, but it is likely that a contribution from the diffuse mini halo (Soboleva et al. 1983) blends with the outer edge of the radio lobes. In general, we give preference to high-resolution observations unless the reduced surface brightness sensitivity of such observations results in a poorly constrained radio lobe volume.

4.7 Conclusions

We have described and tested a hybrid method for measuring the cavity power as an estimate of the amount of mechanical feedback injected by AGNs into their environment. This method is based on a combination of X-ray and radio observations, where the X-ray supplies most of the environmental parameters and the radio observations are used to determine the volume of the cavities in the ICM. By testing this method on a sample of 14 clusters and comparing the hybrid method to the traditional X-ray-based method, we find that the radio-derived cavity volumes are in good agreement with the X-ray-derived cavity volumes, although the systematic uncertainties are in general likely to be underestimated. After calculating the cavity powers associated with the observed cavity volumes, we measure a scatter of 0.44 dex on the correlation between the traditional and the hybrid method, and this scatter improves as the cavities are more clearly detected in the

X-ray observations. Thanks to the LOFAR long baselines, the combination of sensitivity for diffuse radio lobes and the angular resolution to tightly constrain the cavity volume is available for the first time, enabling radio-mode feedback to be studied reliably even at high redshifts. As demonstrated by the number of unique ILT observations processed for this paper, the hybrid method can feasibly be used on relatively large samples of clusters.

From further analysis, we note that the radio observations can in general only be used on sufficiently bright sources of at least $\sim$100 mJy, and recommend careful consideration for the presence of old steep-spectrum plasma which may fall below the sensitivity limit even at low frequencies. Likewise, we also see instances where the radio lobes may be considered to provide the most accurate estimate of the cavity volume as the X-ray cavities are not reliably detected. In general, we recommend that the choice of method is made per cluster based on the quality and contents of the available data.

Acknowledgements

We would like to thank the anonymous referee for useful comments. R.T. and R.J.v.W. acknowledge support from the ERC Starting Grant ClusterWeb 804208. A.B. acknowledges support from the VIDI research programme with project number 639.042.729, which is financed by the Netherlands Organisation for Scientific Research (NWO). This paper is based (in part) on data obtained with the International LOFAR Telescope (ILT) under project code LC14_019. LOFAR (Van Haarlem et al. 2013) is the Low Frequency Array designed and constructed by ASTRON. It has observing, data processing, and data storage facilities in several countries, that are owned by various parties (each with their own funding sources), and that are collectively operated by the ILT foundation under a joint scientific policy. The ILT resources have benefitted from the following recent major funding sources: CNRS-INSU, Observatoire de Paris and Université d'Orléans, France; BMBF, MIWF-NRW, MPG, Germany; Science Foundation Ireland (SFI), Department of Business, Enterprise and Innovation (DBEI), Ireland; NWO, The Netherlands; The Science and Technology Facilities Council, UK; Ministry of Science and Higher Education, Poland. The National Radio Astronomy Observatory is a facility of the National Science Foundation operated under cooperative agreement by Associated Universities, Inc. The Jülich LOFAR Long Term Archive and the German LOFAR network are both coordinated and operated by the Jülich Supercomputing Centre (JSC), and computing resources on the supercomputer JUWELS at JSC were provided by the Gauss Centre for Supercomputing e.V. (grant CHTB00) through the John von Neumann Institute for Computing (NIC).

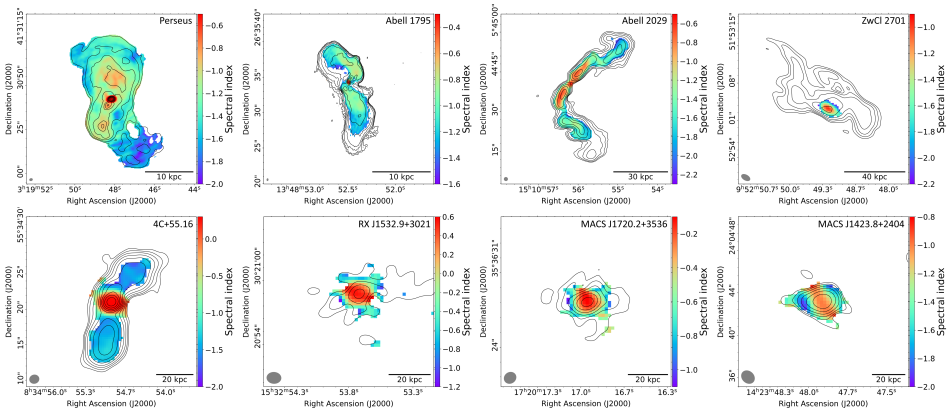

Figure 4.7: Spectral index maps of the high-resolution sample based on LOFAR and VLA observations. The spectral index for all targets is calculated between 144 MHz and 1.5 GHz, except for Abell 1795, for which the spectral index is calculated between 144 MHz and 8 GHz. All spectral index maps are masked below 3σ confidence. The black contours indicate the radio intensity at 144 MHz and are drawn in increments of 2, starting at 5 times the rms noise level. The beam is indicated in gray in the bottom left corner of each panel.

Appendix

4.A Spectal index maps

To produce spectral index maps of our high-resolution sample, we obtained archival VLA observations at 1.5 GHz (Project codes: AA54, AK145, AJ99, AS309, AC243, AL252, AR343, 14A-040) for most of the sources in our high-resolution sample. The 1.5 GHz VLA map of Perseus was obtained courtesy of Gendron-Marsolais et al. (2021), and for Abell 1795 we opted to obtain the 8 GHz observations (Project codes: AG262, AG273). All raw data were processed following the standard VLA data reduction procedure (e.g., Timmerman et al. 2021). Next, for each cluster, we applied the same uv lower limits to both the LOFAR and VLA data and smoothed the resulting images to the same synthesized beam. Finally, we obtain the spectral index maps shown in Figure 4.7.

5

The first high-redshift cavity power measurements of cool-core galaxy clusters with the International LOFAR Telescope

Roland Timmerman, Reinout J. van Weeren, Andrea Botteon, Huub J. A. Röttgering, Leah K. Morabito and Frits Sweijen

Submitted to Astronomy & Astrophysics.

Abstract

Radio-mode feedback associated with the active galactic nuclei (AGN) at the cores of galaxy clusters injects large amount of energy into the intracluster medium (ICM), offsetting radiative losses through X-ray emission. This mechanism prevents the ICM from rapidly cooling down and fueling extreme starburst activity as it accretes onto the central galaxies, and is therefore a key ingredient in the evolution of galaxy clusters. However, the influence and mode of feedback at high redshifts ($z \sim 1$) remains largely unknown. Low-frequency sub-arcsecond resolution radio observations taken with the International LOFAR Telescope have demonstrated their ability to assist X-ray observations with constraining the energy output from the AGNs (or "cavity power") in galaxy clusters, thereby enabling research at higher redshifts than before. In this pilot project, we test this hybrid method on a high redshift ($0.6 < z < 1.3$) sample of 13 galaxy clusters for the first time with the aim of verifying the performance of this method at these redshifts and providing the first estimates of the cavity power associated with the central AGN for a sample of distant clusters. We were able to detect clear radio lobes in three out of thirteen galaxy clusters, and use these detections in combination with ICM pressures obtained from X-ray observations to calculate the corresponding cavity powers of the AGNs. By combining our results with the literature, the current data appear to suggest that the average cavity power peaked at a redshift of $z \sim 0.4$ and slowly decreases toward higher redshifts. However, we require more and tighter constraints on the cavity volume and a better understanding of our observational systematics to confirm any deviation of the cavity power trend from a constant level.

5.1 Introduction

A feedback cycle is created when supermassive black holes (SMBHs) in the cores of (proto-)cluster galaxies accrete cooling gas and accelerate relativistic jets into their environment. This re-energizes the cooling gas, and is therefore understood to play a critical role in the formation and evolution of galaxy clusters (e.g., McNamara & Nulsen 2007; Fabian 2012; Gitti et al. 2012a). However, observational constraints have limited our knowledge about this feedback process mainly to the local Universe, leaving a Gyr-scale blind spot on one of the most influential epochs in which this process took place: the formation and early evolution of our present-day galaxy clusters.

As the hot and diffuse intracluster medium (ICM) permeating a cluster of galaxies cools down through the emission of X-rays, it sinks down toward the gravitational center of the cluster in the form of a "cooling flow" (Fabian 1994). There, it accretes onto the central brightest cluster galaxy (BCG), which typically dominates the core of the cluster, where it is expected to lead to an extremely high star-formation rate. However, as this cooling flow also feeds the central SMBH, it creates an active galactic nucleus (AGN), which releases a significant fraction of the mass-energy of the accreting gas into the cluster environment in the form of radiation ("quasar-mode" feedback) and two relativistic jets ("radio-mode" or mechanical feedback, Croton et al. 2006). This prevents the ICM from rapidly cooling down and suppresses star-formation in the central galaxies.

If the AGN accretes gas at a low fraction of its Eddington rate, it primarily provides radio-mode feedback (e.g., Russell et al. 2013). The two relativistic jets which inflate large radio lobes in the cluster environment, excavate regions within the ICM. This interaction re-energizes the ICM, and enables the energy output of the AGN to be measured (e.g., McNamara et al. 2000; Nulsen et al. 2002; Bîrzan et al. 2004; Rafferty et al. 2006). Based on the internal energy of the radio lobes and the work required to excavate the lobe volume against the external pressure of the ICM, the total energy required to produce the radio lobes can be determined, which in combination with an estimate of the age of the lobes can be used to measure the average energy output of the AGN during its active phase.

Due to the demanding observational requirements of performing these measurements, the high-redshift ($z > 0.6$) regime has largely remained out of reach. The diffuse relativistic plasma of the radio lobes is primarily bright toward low radio frequencies. However, as the angular resolution of a radio interferometer scales with frequency, until recently low-frequency observations only provided a low angular resolution, making it difficult to resolve the structure of the radio lobes. Diverting to higher frequencies, where the angular resolution improves, presents the problem that the old steep-spectrum emission tends to fall below the detection limit of the instrument. Likewise, X-ray observations, which reveal "cavities" in the ICM coincident with the radio lobes, require infeasibly long exposure times for high-redshift clusters to reach the photon count statistics needed to identify and constrain the dimensions of the cavities.

The recent breakthrough in the calibration of LOw Frequency ARray (LOFAR, Van Haarlem et al. 2013) data solves the challenges presented by the strong

Table 5.1: Summary of the sample of galaxy clusters used in this paper. High-resolution LOFAR observations have been processed for the galaxy clusters indicated with boldface. Non-detections are indicated with a horizontal dash. Sources which are located beyond the coverage of the corresponding survey are indicated with ellipsis.

Cluster name	R.A. (J2000)	Dec. (J2000)	z	$c_{\rm SB}$	M_{500} (10^{14} $M_\odot$)	$S_{\rm TGSS}$ (mJy)	$S_{\rm VLASS}$ (mJy)	$S_{\rm LoTSS}$ (mJy)
RCS 1419+5326	14h19m12.1s	53d26m11.6s	0.620	0.185	2.60 (2)	-	-	-
CDGS40	14h50m09.0s	09d04m48.7s	0.644	0.103	1.86 (4)	-	-	...
EGSXG J1417.9+5235	14h17m53.7s	52d34m46.2s	0.683	0.119	0.55 (4)	-	-	-
EGSXG J1420.5+5308	14h20m33.3s	53d08m21.1s	0.734	0.160	1.07 (4)	92	11	81
MS 1137+6625	11h40m22.8s	66d08m14.5s	0.782	0.096	4.70 (4)	-	-	-
RX J1317+2911	13h17m21.8s	29d11m17.0s	0.805	0.123	1.73 (4)	-	-	-
RX J1716+6708	17h16m38.8s	67d08m25.8s	0.813	0.082	5.10 (1)	-	2.5	51
EGSXG J1416.2+5205	14h16m16.7s	52d05m58.2s	0.832	0.120	1.31 (4)	-	2.6	17
RX J1226+3333	12h26m58.2s	33d32m48.0s	0.890	0.083	7.80 (3)	-	1.9	28
CDGS54	10h02m01.0s	02d13m28.6s	0.900	0.093	2.32 (4)	19.2	3.9	...
CL J1415+3612	14h15m11.2s	36d12m04.0s	1.030	0.151	3.44 (4)	-	2.9	7.0
RX J0910+5422	09h10m45.4s	54d22m05.0s	1.106	0.101	0.87 (4)	-	-	2.0
RX J0849+4452	08h28m58.2s	44d51m55.1s	1.261	0.099	2.84 (4)	-	-	-

References. (1) Ettori et al. (2004); (2) Hicks et al. (2008); (3) Mantz et al. (2010); (4) Pascut & Ponman (2015)

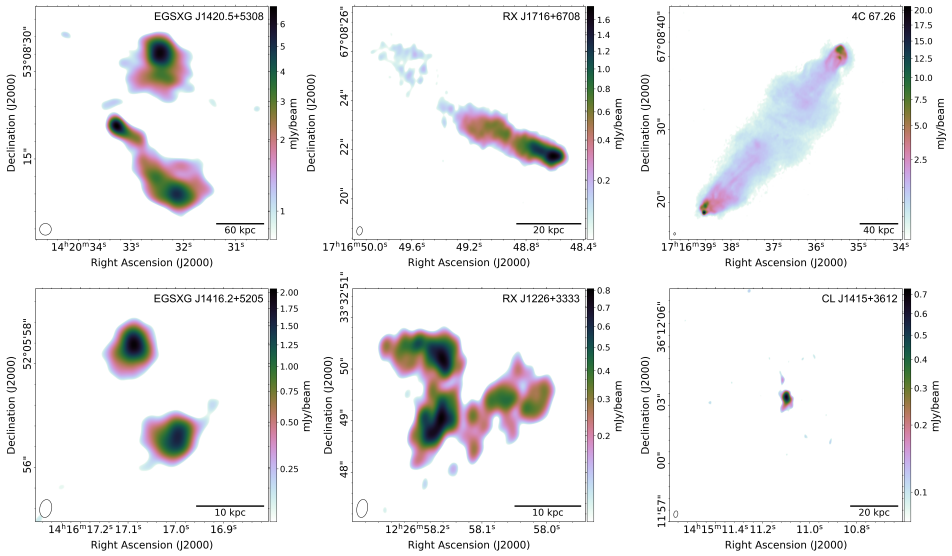

Figure 5.1: High-resolution LOFAR images of all detected BCGs in the galaxy clusters in our sample. The radio source 4C 67.46 was added as this galaxy of RX J1716+6708 is a prominent member of the cluster at radio wavelengths and may be confused with the BCG at low angular resolutions. The color maps range from three times the rms noise level to the peak brightness. The scale bar in the bottom right corner of each panel measures the listed physical length at the redshift of the respective clusters. The size of the beam is indicated by the black ellipse in the bottom left corner of each panel.

ionospheric effects at low frequencies, the heterogeneous dipole arrays and the terabyte-scale data volumes to enable the use of the international baselines (Morabito et al. 2022; Sweijen et al. 2022). Compared to the Dutch part of LOFAR, which offers an angular resolution of $\theta \approx 6$ arcseconds at 144 MHz, the International LOFAR Telescope (ILT) is an order-of-magnitude improvement by achieving an angular resolution of $\theta \approx 0.3$ arcseconds at the same frequency. This provides the combination of angular resolution and sensitivity required to study the radio lobes in detail at high redshifts, opening the observational window for high-redshift measurements of the amount of radio-mode feedback (Timmerman et al. 2022a).

To take advantage of this new observational frontier, we use a sample of high-resolution dedicated observations taken with the ILT to explore the feasibility of accurately measuring the amount of AGN feedback using the hybrid cavity power method at high redshifts ($z > 0.6$). The aim is to reveal the AGN energy output of a limited sample of high-redshift galaxy clusters for the first time.

In this paper, we adopt a ΛCDM cosmology with a Hubble parameter of $H_0 = 70$ km s^{-1} Mpc^{-1}, a matter density parameter of $\Omega_m = 0.3$, and a dark energy density parameter of $\Omega_\Lambda = 0.7$. We define our spectral indices α according to $S_\nu \propto \nu^\alpha$, where S_ν is flux density and ν is frequency. All uncertainties denote the 68.3%=1σ confidence interval.

5.2 Methodology

The gold standard for estimating the amount of energy injected by the central AGN into the cluster environment is computing the *cavity power*. In short, as the radio jets from the AGN slow down within the cluster environment, they expand against the external pressure from the ICM. In X-ray observations, which are primarily sensitive to the hot ICM, this results in surface brightness depressions at the location of the radio lobes, also known as cavities. The total energy associated with this radio lobe is the sum of both the work required to inflate the volume of the radio lobes against the external pressure and the internal energy of the radio lobes. Assuming the radio lobes consist of relativistic gas, the total enthalpy of a radio lobe or X-ray cavity ($E_{\rm cav}$) can be calculated as

$$E_{\rm cav} = 4pV, \tag{5.1}$$

where p is the pressure within the ICM and V is the volume of the radio lobe. Finally, the average power output of the AGN can be obtained by dividing this total enthalpy by the age of the structures. As the radio lobes are less dense than their surrounding ICM, these can be assumed to rise away from the central AGN buoyantly. This gives an age estimate of the radio lobes of

$$t_{\rm buoy} = R\sqrt{\frac{SC}{2gV}}, \tag{5.2}$$

where R is the distance between the AGN and the center of the radio lobe, S is the cross-sectional area of the radio lobe, C is the drag coefficient which by simulations is estimated to be around 0.75 (Churazov et al. 2001), and g is the local gravitational acceleration. Following Bîrzan et al. (2004), we assume that the local acceleration is mainly the result of the mass of the BCG, and therefore we use the approximation of a isothermal sphere, such that

$$g = \frac{2\sigma^2}{R}, \tag{5.3}$$

where σ is the stellar velocity dispersion (Binney & Tremaine 1987). As the stellar velocity dispersion is difficult to estimate at high redshifts based on shallow photometry, but typically does not strongly vary, we adopt an estimate of $\sigma = 289$ km/s, following Bîrzan et al. (2004).

The two key unknowns in this method are the dimensions of the radio lobes or cavities, and the pressure within the ICM. In the hybrid approach demonstrated in Timmerman et al. (2022a), high-resolution low-frequency radio observations are used to determine the dimensions and positions of the radio lobes, and X-ray observations are used to constrain the pressure within the ICM. The advantage of using radio observations to measure the size of the radio lobes rather than X-ray observations to measure the size of the cavities is that cavities are only visible as a surface brightness depression relative to the rest of the ICM. This means that it can take infeasibly long observation times for X-ray telescopes to reach the sensitivity required to detect the cavities. Additionally, cavities tend to be

poorly constrained toward large radii, as the ICM also features a decreasing surface brightness profile. This is largely resolved by the ability of low-frequency radio observations to detect the old electron population of radio lobes, which typically trace the complete volume of the structure relatively well. However, currently the only instrument which has the demonstrated combination of resolution and sensitivity to the radio lobes is the ILT. By relying on radio observations to provide the volume measurements, X-ray observations only need to provide the pressure in the ICM, which requires less sensitivity.

The dimensions of the radio lobes forms the primary cause of uncertainty on the final cavity power estimates. The main uncertainty is the projection angle. To obtain the best estimate for the cavity volume, we use a Monte Carlo method to guess a random projection angle and calculate the corresponding true dimensions of the radio lobe assuming an ellipsoidal shape, the distance to the AGN core and ICM pressure. The best estimates and uncertainties are then taken as the median and 68.3% confidence interval, respectively. Contrary to in Timmerman et al. (2022a), we also include the pressure profile in the Monte Carlo simulation. This was previously not possible as only the ICM pressure at the cavity position was available in literature.

We note that further uncertainties are introduced by inaccuracies in, for instance, the assumption for the pressure profile, the possibility of radio emission extending below the detection limit and the deviation of the radio lobe morphology from an ellipsoid. However, quantifying these uncertainties is not within the scope of this project.

5.3 Sample

The sample analyzed in this pilot project is based on the high-redshift ($z > 0.6$) galaxy cluster samples of Santos et al. (2008), Santos et al. (2010) and Pascut & Ponman (2015). For all 88 clusters in these samples, their dynamical state was estimated based on X-ray observations. In particular, the concentration parameters of the X-ray surface brightness profile ($c_{\rm SB}$), which is estimated using the ICM column density, was measured for each of the clusters. Following Santos et al. (2008), we classify non-cool core clusters as $c_{\rm SB} < 0.075$, weak cool-core clusters as $0.075 <= c_{\rm SB} < 0.155$ and strong cool-core clusters as $0.155 < c_{\rm SB}$. As previous work, which forms the foundation of this project, is primarily focused on cool-core clusters, we disregard non-cool core clusters for high-resolution observations in this pilot project. However, we do intend to explore the non-cool core regime in a follow-up project. Finally, we can only consider galaxy clusters located in the Northern Hemisphere due to the observational constraints of LOFAR. These selection criteria lead to the sample of thirteen galaxy clusters summarized in Table 5.1.

To derive the cavity power associated with the central AGNs of these clusters, high-resolution LOFAR observations have been carried out. As processing such observations is computationally expensive, we only proceeded to analyze galaxy clusters which are sufficiently bright (>5 mJy at 144 MHz) in the

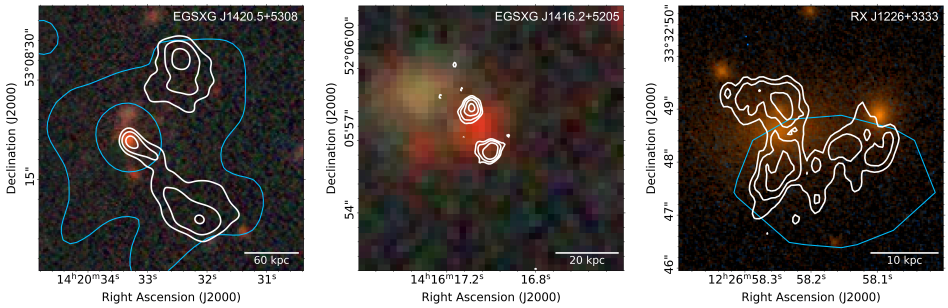

Figure 5.2: Optical images of the three BCGs in our sample for which radio lobes have been detected with LOFAR. The optical images for the two EXSXG clusters were obtained from the DESI Legacy Imaging Survey g, r and z bands (Dey et al. 2019), whereas for RX J1226+3333 the optical image was obtained from Hubble Space Telescope observations with the ACS/WFC detector in F850LP, F625W and F435W filters. The white contours indicate the radio emission at 144 MHz and are drawn at $4\sigma_{\rm rms}$ and increase in factors of 2. The blue contours indicate the 0.5–7 keV X-ray emission as detected by the Chandra X-Ray Observatory. The scale bar in the bottom right corner of each panel measures the listed length at the redshift of the respective cluster.

LOFAR Two-Metre Sky Survey (LoTSS, Shimwell et al. 2017, 2019, 2022) to potentially provide a significant result. Sources outside of the current LoTSS coverage were also included if the flux densities observed in the TIFR Giant Metrewave Radio Telescope Sky Survey (TGSS, Intema et al. 2017) and the Very Large Array Sky Survey (VLASS, Lacy et al. 2020) suggest that they would likely exceed 5 mJy in brightness at 144 MHz. This final subsample consists of EGSXG J1420.5+5308, RX J1716+6708, EGSXG J1416.2+5205, RX J1226+3333, CCDGS54 and CL J1415+3612.

5.4 Observations and data reduction

5.4.1 Radio - LOFAR

The sources selected for high-resolution observations were observed with LOFAR for a duration of 8 hours each in the frequency range between 120 and 168 MHz (Project codes LC15_031 and LC16_015, PI: R. Timmerman). To be able to perform the clock and bandpass calibration, a calibrator source was observed for 10 minutes before and after the target observation. As a first step, the data were reduced using the standard LOFAR calibration Prefactor software package (Van Weeren et al. 2016; Williams et al. 2016; de Gasperin et al. 2019). This step includes flagging radio-frequency interference (RFI) using AOFlagger (Offringa et al. 2013, 2015). Next, a model of the calibrator source was compared to the data to calculate corrections for the delays between the two polarizations per station, the Faraday rotation due to magnetic fields in Earth's ionosphere, the bandpass and the clock offsets between the different LOFAR stations. With these corrections

applied to the target data, RFI was again flagged from these data before these are averaged to a time resolution of 8 seconds per integration and 98 kHz of bandwidth per frequency channel. Finally, the data from the Dutch part of LOFAR were compared to a TGSS sky model to perform the initial phase-only calibration of these visibilities.

Following the standard LOFAR calibration pipelines, we proceeded with the LOFAR-VLBI pipeline developed by Morabito et al. (2022). This pipeline starts by applying the previously derived calibration solutions to all LOFAR stations. Next, LOFAR's core stations were phased up to form a single large virtual station with a narrow field of view, thereby reducing the interference from unrelated nearby radio sources on the target. Then, dispersive phase corrections and residual gain corrections were derived by self-calibrating on a bright and compact source from the Long-Baseline Calibrator Survey (LBCS, Jackson et al. 2016, 2022) near the target. Finally, after all calibration solutions were applied to the target, a final self-calibration routine of total electron content (TEC) and phase fitting using DP3 mode 'tecandphase' was performed on the target source. This accounts for the direction dependence of the previously derived calibration solutions (Van Weeren et al. 2021).

5.4.2 X-rays - Chandra

We queried the Chandra data archive[1] and downloaded the Chandra Advanced CCD Imaging Spectrometer (ACIS) observations of the targets in our sample that show clear radio lobes (Fig. 5.1 and Table 5.2) to obtain X-ray images of the thermal gas emission. We retrieved data for EGSXG J1420.5+5308 (ObsIDs: 5845, 5846, 6214, 6215, 9450, 9451, 9452, 9720, 9721, 9722, 9723, 9724, 9725, 9726, 9793, 9794, 9795, 9796, 9797, 9842, 9843, 9844, 9863, 9866, 9870, 9873, 9876), EGSXG J1416.2+5205 (ObsIDs: 5853, 5854, 6222, 6222, 6366), and RX J1226+3333 (ObsIDs: 932, 3180, 5014). All data were reduced using CIAO v4.12 tools following standard procedures, adopting the CALDB v4.9.0 (see also our previous work, Timmerman et al. 2022a). Multiple ObsIDs for the same target were mosaiced into a single image in the 0.5-7.0 keV band for the subsequent analysis.

5.5 Results

5.5.1 Imaging

To derive the cavity power associated with the AGNs in our high-redshift galaxy cluster sample, we produced high-resolution ($\sim$0.3 arcseconds) images at 144 MHz using the calibrated data sets of all sources in our sample using WSClean (Offringa et al. 2014; Offringa & Smirnov 2017). Of these images, only CDGS54 resulted in a non-detection, suggesting that this source contains mostly emission on angular scales significantly larger than 0.3 arcseconds. The other galaxy clusters are shown in Fig. 5.1. We included the radio source 4C 67.26 in this figure as

[1] `https://cda.harvard.edu/chaser/`

Table 5.2: Properties of the cavities in our sample derived using the hybrid X-ray–radio method.

(a) Cluster name	(b) Redshift	(c) $R_{\rm l}$ (kpc)	(d) $R_{\rm w}$ (kpc)	(e) R (kpc)	(f) V (kpc^3)	(g) p (keV/cm^3)	(h) $t_{\rm buoy}$ (10^7 yr)	(i) $P_{\rm cav}$ (10^{42} erg/s)
EGSXG J1420.5+5308 (N)	0.734	43.3	40.0	105	$3.04^{+0.35}_{-0.21} \times 10^5$	$6.15^{+3.05}_{-3.02} \times 10^{-3}$	$25.5^{+23.1}_{-4.7}$	$42.9^{+27.3}_{-28.4}$
EGSXG J1420.5+5308 (S)	0.734	51.7	35.7	112	$3.03^{+1.14}_{-0.29} \times 10^5$	$5.77^{+2.99}_{-2.96} \times 10^{-3}$	$25.2^{+17.9}_{-4.2}$	$41.1^{+24.0}_{-24.1}$
EGSXG J1416.2+5205 (N)	0.832	3.04	2.66	7.53	$93.8^{+55.5}_{-38.9}$	$1.86^{+1.20}_{-0.75} \times 10^{-2}$	$1.36^{+1.38}_{-0.56}$	$0.49^{+0.64}_{-0.29}$
EGSXG J1416.2+5205 (S)	0.832	2.28	2.55	7.53	$57.9^{+38.4}_{-26.6}$	$1.87^{+1.20}_{-0.75} \times 10^{-2}$	$2.19^{+1.42}_{-0.65}$	$0.28^{+0.40}_{-0.18}$
RX J1226+3333 (N)	0.890	5.47	2.64	6.21	195^{+132}_{-82}	$1.03^{+1.75}_{-0.63}$	$1.06^{+0.49}_{-0.24}$	108^{+233}_{-73}
RX J1226+3333 (S)	0.890	5.32	1.79	6.21	$89.4^{+84.7}_{-50.1}$	$1.03^{+1.75}_{-0.62}$	$1.07^{0.67}_{-0.33}$	$46.7^{+114.6}_{-34.8}$

Notes. Columns: (a) cluster name; (b) cluster redshift; (c) cavity radius along the jet axis; (d) cavity radius perpendicular to the jet axis; (e) central cavity distance from the AGN core; (f) cavity volume; (g) ICM pressure at the projected distance of the radio lobe to the AGN core; (h) buoyancy timescale; (i) cavity power

it was identified to be a member galaxy of RX J1716+6708 (Gioia et al. 1999) and it dominates the region at radio wavelengths.

Our images reveal sets of clear radio lobes in EGSXG J1420.5+5308 and 4C 67.26. Additionally, we detect a further two sets of radio lobes in EGSXG J1416.2+5205 and RX J1226+3333, but it is unclear whether we have revealed the full physical extent of these radio lobes. The radio source 4C 67.26 shows a strong and undisturbed FR II-like morphology, but as this member galaxy is located far outside of the cluster center and therefore not part of the feedback cycle, it will be disregarded from further analysis. Optical overlays of the remaining three sources with detected radio lobes are shown in Fig. 5.2, along with their respective X-ray emission.

The radio structure of EGSXG J1416.2+5205 consists of two equally bright components, which are assumed to be the radio lobes of the BCG, but due to the barely resolved structure, this remains uncertain. The BCG associated with EGSXG J1416.2+5205 is located directly in between the two radio lobes. Similarly, RX J1226+3333 also features uncertain radio lobes. Given that the BCG is detected directly in between the eastern-most structures, these are considered to be two radio lobes located toward the North and South of the BCG, with the western-most emission likely being unrelated. However, due to the low brightness of the radio lobes, it is unclear if the full extent of these structures is detected.

The BCG of RX J1716+6708 shows radio lobes bending toward the East. This aligns with the direction of the distribution of members galaxies (Henry et al. 1997), suggesting that the galaxy cluster may be in the late stage of a merger event, consistent with its relatively low concentration parameter of $c_{\rm SB} = 0.082$. Finally, CL J1415+3612 shows a single compact radio component coincident with the BCG in the core of the cluster.

5.5.2 Analysis

From our radio images, we estimate the volume of the radio lobes we have detected assuming an ellipsoidal shape. We note that we consider our observation of EGSXG J1420.5+5308 to allow a reliable radio lobe volume measurements, and consider these measurements to be tentative for EGSXG J1416.2+5205 and RX J1226+3333.

As our sample is selected to be at high redshifts, the X-ray observations do not contain sufficient photon counts to obtain pressure profiles for the individual clusters. Therefore, we use the average pressure profile of a sample of galaxy clusters at high redshift ($0.6 < z < 1.2$) from McDonald et al. (2014), which is normalized by P_{500} and r_{500}, to estimate the ICM thermal pressure at the distance where we observe the radio lobes in our clusters. For EGSXG J1420.5+5308 and EGSXG J1416.2+5205, we use the M_{500} reported in Table 5.1 to compute the P_{500} expected in the standard self-similar model (e.g., Nagai et al. 2007). For RX 1226+3333, instead the pressure profile of the ICM was determined by Romero et al. (2018) using Sunyaev-Zel'dovich (SZ) observations and therefore we directly adopt the value measured via SZ.

Using the measured volumes of the radio lobes, the ICM pressure estimates

and our assumption for the stellar velocity dispersion of the BCGs, we calculate the final cavity power as the ratio between the cavity enthalpy and the buoyancy timescale. Our measurements for the radio lobe dimensions and local ICM pressures are summarized together with the resulting cavity powers in Table 5.2. We find that EGSXG J1420.5+5308 and RX J1226+3333 contain the most radio-mode feedback of our sample, with cavity powers of around 84.3×10^{42} erg/s and 155×10^{42} erg/s, respectively. Meanwhile, the small radio lobes detected in EGSXG J1416.2+5205 only correspond to a cavity power of around 0.77×10^{42} erg/s in total.

5.6 Discussion

The operation of radio-mode feedback has remained poorly quantified at high redshifts ($z > 0.6$). Although significant progress has been made using X-ray observations (e.g., Hlavacek-Larrondo et al. 2015), the observational requirement to clearly detect cavities in the ICM at high redshifts forms a bottleneck. In Timmerman et al. (2022a), we verified at low redshifts that high-resolution low-frequency radio observations taken with the ILT can be used in conjunction with X-ray observation to measure the output power of the AGN, thereby making these measurements more feasible. In this paper, we have applied this method for the first time on a high-redshift sample of galaxy clusters to test the feasibility on this hybrid method in this regime and obtain the first measurements of the energy injected by the AGN into its cluster environment for these systems.

5.6.1 Radio lobe detections

Of the original high-redshift sample of 13 cool-core galaxy clusters compiled by Santos et al. (2008), Santos et al. (2010) and Pascut & Ponman (2015), 6 had previously been detected at radio wavelengths and were therefore selected for high-resolution imaging. Of these 6 clusters, we detected radio lobes associated with 3 BCGs and one additional cluster member. This corresponds to a 23% detection rate of radio lobes, which is significantly higher than the 4.7% detection rate (2 out of 43) previously achieved using X-ray observations of the SPT-SZ sample within the same redshift range (McDonald et al. 2013; Bleem et al. 2015; Hlavacek-Larrondo et al. 2015; Bocquet et al. 2019). However, we note that two of our systems were not bright enough to confirm whether or not the radio lobes extend below the sensitivity limit of our observations. Therefore, the radio lobe volumes and therefore also the associated cavity powers can conservatively be considered to form lower limits on the true cavity volume and hence power.

In Timmerman et al. (2022a), we stated that radio lobes could be expected to be reliably detected in systems brighter than approximately ~ 100 mJy at 144 MHz. Our clear detection of radio lobes in EGSXG J1420.5+5308 with a total flux density of 81 mJy is consistent with this rough previous estimate. Additionally, our radio lobe detections in EGSXG J1416.2+5205 with 17 mJy and RX J1226+3333 with 28 mJy demonstrate that it is possible to detect compact

radio lobes at lower flux densities. However, a lack of radio lobe detections in RX J1226+3333, CL J1415+3612 and CDGS54 also demonstrate the sensitivity limitation for 8-hour ILT observation, even for relaxed clusters (e.g., $c_{\rm SB} = 0.151$ for CL J1415+3612) and decent flux densities (e.g., 51 mJy for RX J1226+3333).

To probe the range of cavity powers accessible to the angular resolution of ILT observations at high redshifts, assuming the sensitivity of an 8-hour observation, we calculate the approximate smallest radio lobe which the ILT can resolve. This defines the lowest cavity power to which the ILT is sensitive. We assume a radio lobe size similar to the angular size of the synthesized beam of the ILT, a distance between the radio lobe and the AGN of two beams to provide a clear identification as a radio lobe, and a pressure profile corresponding to a low-mass galaxy cluster of 10^{14} $\rm M_{\odot}$. For comparison, we perform the same calculation for the standard 6-arcsecond angular resolution observations of only the Dutch part of the ILT. Both exclusion regions are plotted in Fig. 5.3. This shows that the ILT at high redshifts is sensitive to cavity powers on the order of 10^{42} erg/s or more, which enables it to reach even the low-power AGNs in the cores of high-redshift galaxy clusters.

5.6.2 Pressure profiles

Measuring the pressure profiles on a per-cluster basis is impossible due to the low-count statistics of the available X-ray observations. To obtain the ICM pressure at the position of the radio lobes, we used the average pressure profiles from McDonald et al. (2014) derived for a sample of high-redshift clusters. Although this enabled us to determine the cavity power of the AGNs in our sample using shallower X-ray observations compared to also having to determine the cavity volume, we note that obtaining the ICM pressure is still affected by significant uncertainties. In addition to the intrinsic scatter among pressure profiles, the standard pressure profiles from McDonald et al. (2014) depend on M_{500}, which in turn is typically derived based on scaling relations such as the temperature–mass relation (e.g., Sun et al. 2009). SZ observations can relieve some of this uncertainty by providing directly pressure profiles of the ICM. For this reason, we suggest that the combination of X-ray and high-resolution SZ observations with instruments such as MUSTANG and NIKA should be employed at higher redshifts if possible.

5.6.3 Comparison to previous detections

Cavity powers within our redshift regime have only previously been published by Hlavacek-Larrondo et al. (2015), who used deep X-ray observations of the SPT-SZ sample. They detected clear cavities at $z = 0.6838$ and potential cavities at $z = 0.7019$. Additionally, they report marginally convincing cavities at $z = 1.075$ and $z = 1.2$. This is largely in agreement with our radio lobe detections at $z = 0.734$, $z = 0.823$ and $z = 0.890$, which simultaneously almost double the amount of measurements at $z > 0.6$ and establish a new highest redshift at which the cavity power is constrained using radio observations. To compare our cavity power measurements with the results from Hlavacek-Larrondo et al. (2015), we have

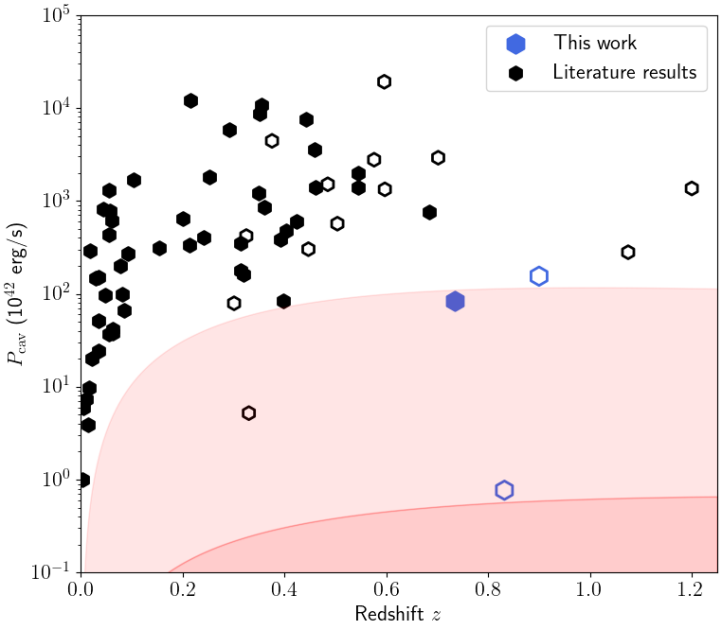

Figure 5.3: Cavity power per galaxy cluster as a function of redshift. The blue data points indicate the three radio lobe systems detected in our sample, and the black data points indicate the cavity power estimates published by Rafferty et al. (2006), Hlavacek-Larrondo et al. (2012), Hlavacek-Larrondo et al. (2015) and Timmerman et al. (2022a). Cavity/radio lobe systems which were indicated to be low significance are indicated with open data points, whereas reliable detections are indicated with solid data points. The light red region indicates the approximate region which is not accessible by 6-arcsecond observations, such as those taken with only the Dutch part of LOFAR. The darker red region indicates the approximate region which is not accessible by 0.3-arcsecond observations, such at those taken with the complete ILT.

plotted these measurements together with additional low-redshift measurements in Fig. 5.3. Our measurements are largely in line with the general trend of cavity power as a function of redshift as probed by Rafferty et al. (2006), Hlavacek-Larrondo et al. (2012) and Hlavacek-Larrondo et al. (2015). The current data, though still consistent with a constant cavity power level, appear to suggest that the average cavity power peaked at a redshift of $z \sim 0.4$ and slowly decreases toward higher redshifts. However, we both require more and tighter constraints on the cavity volume and a better understanding of our observational systematics to confirm any deviation of the cavity power trend from a constant level.

5.6.4 Future projection

As we have demonstrated in Timmerman et al. (2022a) and this pilot project, it is feasible to investigate samples of galaxy clusters with the ILT. For the purpose

of this pilot project, we have only considered cool-core galaxy clusters. However, this simultaneously limited the sample to previously well-studied clusters and excluded a significant fraction of all clusters from this analysis. It would be a logical next step to investigate a wider selection of galaxy clusters at high redshifts. For instance, the catalogs compiled by Wen et al. (2018), Wen & Han (2021) and Wen & Han (2022) provide a valuable sample of optically-selected high-redshift galaxy clusters in the Northern hemisphere, which can be observed by the ILT. Additionally, the recently launched Euclid mission is projected to detect more than 10^5 galaxy clusters up to a redshift of $z = 2$ (Euclid Collaboration 2019). Finally, future SZ surveys in the Northern hemisphere would be critical to ensure that we also investigate the low cluster mass regime at high redshifts.

5.7 Conclusions

In this paper, we have applied the hybrid method of measuring cavity powers (Timmerman et al. 2022a) using combined radio and X-ray observations to a high-redshift ($z > 0.6$) sample of cool-core galaxy clusters. Out of the 13 galaxy clusters within our sample, we were able to detect radio lobes associated with the BCG of three clusters and resolve these using LOFAR's international baselines. Using the pressure profiles by McDonald et al. (2014), we estimated the ICM pressure surrounding the radio lobes. Combined, these measurements provided the first cavity power estimates of three high-redshift galaxy clusters, adding to a very limited sample of these measurements at high redshifts. This demonstrates that the hybrid method of measuring cavity powers is indeed viable at high redshifts using the ILT, which encourages further work in this epoch.

Our cavity power measurements of radio-mode feedback at $z > 0.6$, do fall on the relatively low side compared to the population at lower redshifts. However, not enough measurements are currently present to provide meaningful statistics, which encourages further investigation of larger samples.

Acknowledgements

R.T. and R.J.v.W. acknowledge support from the ERC Starting Grant ClusterWeb 804208. A.B. acknowledges support from the VIDI research programme with project number 639.042.729, which is financed by the Netherlands Organisation for Scientific Research (NWO). L.K.M. is grateful for support from the Medical Research Council [MR/T042842/1]. This work made use of the Dutch national e-infrastructure with the support of the SURF Cooperative using grant no. EINF-1287. This work is co-funded by the EGI-ACE project (Horizon 2020) under Grant number 101017567. This paper is based (in part) on data obtained with the International LOFAR Telescope (ILT) under project codes LC15_031 and LC16_015. LOFAR (Van Haarlem et al. 2013) is the Low Frequency Array designed and constructed by ASTRON. It has observing, data processing, and data storage facilities in several countries, that are owned by various parties (each with their own funding sources), and that are collectively operated by the ILT foundation under a

joint scientific policy. The ILT resources have benefitted from the following recent major funding sources: CNRS-INSU, Observatoire de Paris and Université d'Orléans, France; BMBF, MIWF-NRW, MPG, Germany; Science Foundation Ireland (SFI), Department of Business, Enterprise and Innovation (DBEI), Ireland; NWO, The Netherlands; The Science and Technology Facilities Council, UK; Ministry of Science and Higher Education, Poland. This work made use of the Dutch national e-infrastructure with the support of the SURF Cooperative using grant no. EINF-1287. This project has received support from SURF and EGI-ACE. EGI-ACE receives funding from the European Union's Horizon 2020 research and innovation programme under grant agreement No. 101017567. The Jülich LOFAR Long Term Archive and the German LOFAR network are both coordinated and operated by the Jülich Supercomputing Centre (JSC), and computing resources on the supercomputer JUWELS at JSC were provided by the Gauss Centre for Supercomputing e.V. (grant CHTB00) through the John von Neumann Institute for Computing (NIC). This research has made use of data obtained from the Chandra Data Archive and the Chandra Source Catalog, and software provided by the Chandra X-ray Center (CXC) in the application packages CIAO and Sherpa. This research is based on observations made with the NASA/ESA Hubble Space Telescope obtained from the Space Telescope Science Institute, which is operated by the Association of Universities for Research in Astronomy, Inc., under NASA contract NAS 5–26555. These observations are associated with program 12791. The Legacy Surveys consist of three individual and complementary projects: the Dark Energy Camera Legacy Survey (DECaLS; Proposal ID #2014B-0404; PIs: David Schlegel and Arjun Dey), the Beijing-Arizona Sky Survey (BASS; NOAO Prop. ID #2015A-0801; PIs: Zhou Xu and Xiaohui Fan), and the Mayall z-band Legacy Survey (MzLS; Prop. ID #2016A-0453; PI: Arjun Dey). DECaLS, BASS and MzLS together include data obtained, respectively, at the Blanco telescope, Cerro Tololo Inter-American Observatory, NSF's NOIRLab; the Bok telescope, Steward Observatory, University of Arizona; and the Mayall telescope, Kitt Peak National Observatory, NOIRLab. Pipeline processing and analyses of the data were supported by NOIRLab and the Lawrence Berkeley National Laboratory (LBNL). The Legacy Surveys project is honored to be permitted to conduct astronomical research on Iolkam Du'ag (Kitt Peak), a mountain with particular significance to the Tohono O'odham Nation. NOIRLab is operated by the Association of Universities for Research in Astronomy (AURA) under a cooperative agreement with the National Science Foundation. LBNL is managed by the Regents of the University of California under contract to the U.S. Department of Energy. This project used data obtained with the Dark Energy Camera (DECam), which was constructed by the Dark Energy Survey (DES) collaboration. Funding for the DES Projects has been provided by the U.S. Department of Energy, the U.S. National Science Foundation, the Ministry of Science and Education of Spain, the Science and Technology Facilities Council of the United Kingdom, the Higher Education Funding Council for England, the National Center for Supercomputing Applications at the University of Illinois at Urbana-Champaign, the Kavli Institute of Cosmological Physics at the University of Chicago, Center for Cosmology and Astro-Particle Physics at the Ohio State University, the Mitchell Institute for Fundamental Physics and As-

tronomy at Texas A&M University, Financiadora de Estudos e Projetos, Fundacao Carlos Chagas Filho de Amparo, Financiadora de Estudos e Projetos, Fundacao Carlos Chagas Filho de Amparo a Pesquisa do Estado do Rio de Janeiro, Conselho Nacional de Desenvolvimento Cientifico e Tecnologico and the Ministerio da Ciencia, Tecnologia e Inovacao, the Deutsche Forschungsgemeinschaft and the Collaborating Institutions in the Dark Energy Survey. The Collaborating Institutions are Argonne National Laboratory, the University of California at Santa Cruz, the University of Cambridge, Centro de Investigaciones Energeticas, Medioambientales y Tecnologicas-Madrid, the University of Chicago, University College London, the DES-Brazil Consortium, the University of Edinburgh, the Eidgenossische Technische Hochschule (ETH) Zurich, Fermi National Accelerator Laboratory, the University of Illinois at Urbana-Champaign, the Institut de Ciencies de l'Espai (IEEC/CSIC), the Institut de Fisica d'Altes Energies, Lawrence Berkeley National Laboratory, the Ludwig Maximilians Universitat Munchen and the associated Excellence Cluster Universe, the University of Michigan, NSF's NOIRLab, the University of Nottingham, the Ohio State University, the University of Pennsylvania, the University of Portsmouth, SLAC National Accelerator Laboratory, Stanford University, the University of Sussex, and Texas A&M University. BASS is a key project of the Telescope Access Program (TAP), which has been funded by the National Astronomical Observatories of China, the Chinese Academy of Sciences (the Strategic Priority Research Program "The Emergence of Cosmological Structures" Grant # XDB09000000), and the Special Fund for Astronomy from the Ministry of Finance. The BASS is also supported by the External Cooperation Program of Chinese Academy of Sciences (Grant # 114A11KYSB20160057), and Chinese National Natural Science Foundation (Grant # 12120101003, # 11433005). The Legacy Survey team makes use of data products from the Near-Earth Object Wide-field Infrared Survey Explorer (NEOWISE), which is a project of the Jet Propulsion Laboratory/California Institute of Technology. NEOWISE is funded by the National Aeronautics and Space Administration. The Legacy Surveys imaging of the DESI footprint is supported by the Director, Office of Science, Office of High Energy Physics of the U.S. Department of Energy under Contract No. DE-AC02-05CH1123, by the National Energy Research Scientific Computing Center, a DOE Office of Science User Facility under the same contract; and by the U.S. National Science Foundation, Division of Astronomical Sciences under Contract No. AST-0950945 to NOAO.

Bibliography

Akahori, T., Kitayama, T., Ueda, S., et al. 2020, PASJ, 72, 62

Akritas, M. G. & Bershady, M. A. 1996, ApJ, 470, 706

Albert, J. G., van Weeren, R. J., Intema, H. T., & Röttgering, H. J. A. 2020, A&A, 635, A147

Allen, S. W., Dunn, R. J. H., Fabian, A. C., et al. 2006, MNRAS, 372, 21

Antonuci, R. 1993, ARAA, 31, 473

Arnaud, K. A., Johnstone, R. M., Fabian, A. C., et al. 1987, MNRAS, 227, 241

Ascasibar, Y. & Markevitch, M. 2006, ApJ, 650, 102

Beck, R. & Krause, M. 2005, Astron. Nachr., 326, 414

Biava, N., Brienza, M., Bonafede, A., et al. 2021, A&A, 650, A170

Binney, J. & Tremaine, S. 1987, Galactic dynamics (Princeton University Press)

Bîrzan, L., McNamara, B. R., Nulsen, P. E. J., et al. 2008, ApJ, 686, 859

Bîrzan, L., Rafferty, D. A., & Brüggen, M. 2014, Proceedings of the International Astronomical Union, 10, 251

Bîrzan, L., Rafferty, D. A., Brüggen, M., et al. 2020, MNRAS, 496, 2613

Bîrzan, L., Rafferty, D. A., McNamara, B. R., et al. 2004, ApJ, 607, 800

Blasi, P. & Colafrancesco, S. 1999, Astroparticle Physics, 12, 169

Bleem, L. E., Stalder, B., de Haan, T., et al. 2015, ApJS, 216, 27

Bocquet, S., Dietrich, J. P., Schrabback, T., et al. 2019, ApJ, 878, 55

Böhringer, H., Voges, W., Fabian, A. C., et al. 1993, MNRAS, 264, L25

Bolton, J. G. 1948, Nature, 162, 141

Bonafede, A., Intema, H. T., Brüggen, M., et al. 2014, MNRAS, 444, L44

Branson, N. J. B. A., Elsmore, B., Pooley, G. G., & Ryle, M. 1972, MNRAS, 156, 377

Bravi, L., Gitti, M., & Brunetti, G. 2015, MNRAS, 455, L41

Bridle, A. H. & Perley, R. A. 1984, ARA&A, 22, 319

Brienza, M., Morganti, R., Harwood, J., et al. 2020, A&A, 638, A29

Briggs, D. S. 1995, PhD thesis, New Mexico Institude of Mining and Technology

Brüggen, M., Heinz, S., Roediger, E., et al. 2007, MNRAS, 380, L67

Brüggen, M. & Kaiser, C. R. 2002, Nat, 418, 301

Brunetti, G., Blasi, P., Reimer, O., et al. 2012, MNRAS, 426, 956

Brunetti, G. & Jones, T. W. 2014, International Journal of Modern Physics D, 23, 1430007

Brunetti, G., Zimmer, S., & Zandanel, F. 2017, MNRAS, 472, 1506

Burns, J. O., Schwendeman, E., & White, R. A. 1983, ApJ, 271, 575

Böhringer, H., Burwitz, V., Zhang, Y. Y., et al. 2005, ApJ, 633, 148

Callingham, J. R., Ekers, R. D., Gaensler, B. M., et al. 2017, ApJ, 836, 174

Cappellari, M. 2002, MNRAS, 333, 400

Carilli, C. L., Perley, R. A., & Harris, D. E. 1994, MNRAS, 270, 173

Carilli, C. L. & Taylor, G. B. 2002, ARA&A, 40, 319

Cavagnolo, K. W., McNamara, B. R., Nulsen, P. E. J., et al. 2010, ApJ, 720, 1066

Chiu, I., Mohr, J. J., McDonald, M., et al. 2018, MNRAS, 478, 3072

Churazov, E., Brüggen, M., Kaiser, M., et al. 2001, ApJ, 554, 261

Churazov, E., Forman, W., Jones, C., & Böhringer, H. 2003, ApJ, 590, 225

Ciotti, L., Ostriker, J. P., & Proga, D. 2010, ApJ, 717, 708

Clarke, T. E., Blanton, E. L., & Sarazin, C. L. 2004, ApJ, 616, 178

Cohen, A. S., Clarke, T. E., Feretti, L., & Kassim, N. E. 2005, ApJ, 620, L5

Comerford, J. M. & Natarajan, P. 2007, MNRAS, 379, 190

Cotton, W. D. 2008, PASP, 120, 439

Covone, G., Adami, C., Durret, F., et al. 2006, A&A, 460, 381

Crain, R. A., Schaye, J., Bower, R. G., et al. 2015, MNRAS, 450, 1937

Croston, J. H. & Hardcastle, M. J. 2014, MNRAS, 438, 3310

Croton, D. J., Springel, V., White, S. D. M., et al. 2006, MNRAS, 365, 11

Dale, J. E. 2015, NAR, 68, 1

de Gasperin, F., Dijkema, T. J., Drabent, A., et al. 2019, A&A, 622, A5

del P. Lagos, C., Cora, S. A., & Padilla, N. D. 2008, MNRAS, 388, 587

Dey, A., Schlegel, D. J., Lang, D., et al. 2019, AJ, 157, 168

Doria, A., Gitti, M., Ettori, S., et al. 2012, ApJ, 753, 47

Dreher, J. & Feigelson, E. 1984, Nature, 308, 43

Dunn, R. J. H. & Fabian, A. C. 2004, MNRAS, 355, 862

Edge, A. C., Stewart, G. C., & Fabian, A. C. 1992, MNRAS, 258, 177

Ehlert, S., Allen, S. W., von der Linden, A., et al. 2011, MNRAS, 411, 1641

Enßlin, T. A. 2003, A&A, 399, 409

Enßlin, T. A. & Gopal-Krishna. 2001, A&A, 366, 26

Ettori, S., Tozzi, P., Borgani, S., & Rosati, P. 2004, A&A, 417, 13

Euclid Collaboration. 2019, A&A, 627, A23

Fabian, A. C. 1994, ARA&A, 32, 277

Fabian, A. C. 1999, PNAS, 96, 4749

Fabian, A. C. 2012, ARA&A, 50, 455

Fabian, A. C., Nulsen, P. E. J., & Canizares, C. R. 1982, MNRAS, 201, 933

Fabian, A. C., Sanders, J. S., Ettori, S., et al. 2000, MNRAS, 318, L65

Fabian, A. C., Sanders, J. S., Ettori, S., et al. 2001, MNRAS, 321, L33

Fabian, A. C., Sanders, J. S., Taylor, G. B., et al. 2006, MNRAS, 366, 417

Fanaroff, B. L. & Riley, J. M. 1974, MNRAS, 167, 31P

Feretti, L., Fusco-Femiano, R., Giovannini, G., & Govoni, F. 2001, A&A, 373, 106

Feretti, L., Giovannini, G., Govoni, F., & Murgia, M. 2012, A&AR, 20, 54

Font, A. S., McCarthy, I. G., Poole-Mckenzie, R., et al. 2020, MNRAS, 498, 1765

Forman, W., Kellogg, E., Hursky, H., et al. 1972, ApJ, 178, 309

Fujita, Y., Kohri, K., Yamazaki, R., & Kino, M. 2007, ApJL, 663, L61

Gendron-Marsolais, M. L., Hlavacek-Larrondo, J., van Weeren, R. J., et al. 2017, MNRAS, 469, 3872

Gendron-Marsolais, M. L., Hlavacek-Larrondo, J., van Weeren, R. J., et al. 2020, MNRAS, 499, 5791

Gendron-Marsolais, M. L., Hull, C. L. H., Perley, R., et al. 2021, ApJ, 911, 56

Giacintucci, S., Markevitch, M., Cassano, R., et al. 2019, ApJ, 880, 70

Giacintucci, S., Venturi, T., Brunetti, G., et al. 2005, A&A, 440, 867

Gioia, I. M., Henry, J. P., Mullis, C. R., et al. 1999, AJ, 117, 2608

Gitti, M., Brighenti, F., & McNamara, B. R. 2012a, Advances in Astronomy, 2012, 950641

Gitti, M., Brighenti, F., & McNamara, B. R. 2012b, Advances in Astronomy, 2012, 950641

Gitti, M., Brunetti, G., Feretti, L., & Setti, G. 2004, A&A, 417, 1

Gitti, M., Brunetti, G., & Setti, G. 2002, A&A, 386, 456

Gitti, M., McNamara, B. R., Nulsen, P. E. J., & Wise, M. W. 2007, ApJ, 660, 1118

Gitti, M., O'Sullivan, E., Giacintucci, S., et al. 2010, ApJ, 714, 758

Gitti, M. & Schindler, S. 2004, A&A, 427, L9

Gizani, N. A. B., Cohen, A., & Kassim, N. E. 2005, MNRAS, 358, 1061

Gizani, N. A. B., Garrett, M. A., & Leahy, J. P. 2002, PASA, 19, 69

Gizani, N. A. B. & Leahy, J. P. 1999, NAR, 43, 639

Gizani, N. A. B. & Leahy, J. P. 2003, MNRAS, 342, 399

Gizani, N. A. B. & Leahy, J. P. 2004, MNRAS, 350, 865

Godfrey, L. E. H. & Shabala, S. S. 2013, ApJ, 767, 12

Govoni, F., Enßlin, T. A., Feretti, L., & Giovannini, G. 2001, A&A, 369, 441

Govoni, F. & Feretti, L. 2004, Int. J. Mod. Phys. D, 13, 1549

Greenstein, J. L. 1962, ApJ, 135, 679

Gull, S. F. & Northover, K. J. E. 1973, Nat, 244, 80

Gursky, H., Kellogg, E., Murray, S., et al. 1971, ApJ, 167, L81

Hardcastle, M. J. & Krause, M. G. H. 2013, MNRAS, 430, 174

Hardcastle, M. J. & Krause, M. G. H. 2014, MNRAS, 443, 1482

Häring, N. & Rix, H.-W. 2004, ApJL, 604, L89

Harwood, J. J., Hardcastle, M. J., & Croston, J. H. 2015, MNRAS, 454, 3403

Harwood, J. J., Hardcastle, M. J., Croston, J. H., & Goodger, J. L. 2013, MNRAS, 435, 3353

Henry, J. P., Gioia, I. M., Mullis, C. R., et al. 1997, AJ, 114, 1293

Hicks, A. K., Ellingson, E., Bautz, M., & other. 2008, ApJ, 680, 1022

Hlavacek-Larrondo, J., Allen, S. W., Taylor, G. B., & other. 2013, ApJ, 777, 163

Hlavacek-Larrondo, J., Fabian, A. C., Edge, A. C., et al. 2012, MNRAS, 421, 1360

Hlavacek-Larrondo, J., Fabian, A. C., Sanders, J. S., & Taylor, G. B. 2011, MNRAS, 415, 3520

Hlavacek-Larrondo, J., McDonald, M., Benson, B. A., et al. 2014, ApJ, 805, 35

Hlavacek-Larrondo, J., McDonald, M., Benson, B. A., et al. 2015, ApJ, 805, 35

Hoang, D. N., Shimwell, T. W., van Weeren, R. J., et al. 2019, A&A, 622, A20

Ignesti, A., Brunetti, G., Gitti, M., & Giacintucci, S. 2020, A&A, 640, A37

Ignesti, A., Brunetti, G., Shimwell, T., et al. 2022, A&A, 659, A20

Intema, H. T., Jagannathan, P., Mooley, K. P., & Frail, D. A. 2017, A&A, 598, A78

Intema, H. T., van der Tol, S., Cotton, W. D., et al. 2009, A&A, 501, 1185

Jackson, N., Badole, S., Morgan, J., et al. 2022, A&A, 658, A2

Jackson, N., Tagore, A., Deller, A., et al. 2016, A&A, 2016, A86

Jaffe, W. & Perola, G. C. 1974, A&A, 31, 223

Jaffe, W. J. & Perola, G. C. 1973, A&A, 26, 423

Johnstone, R. M., Allen, S. W., Fabian, A. C., & Sanders, J. S. 2002, MNRAS, 336, 299

Jubelgas, M., Springel, V., Enßlin, T., & Pfrommer, C. 2007, A&A, 481, 33

Kaastra, J. S., Ferrigno, C., Tamura, T., et al. 2001, A&A, 365, L99

Kataoka, J. & Stawarz, Ł. 2005, ApJ, 622, 797

Kellerman, K. I., Pauliny-Toth, I. I. K., & Williams, P. J. S. 1969, ApJ, 157, 1

Kellerman, K. I., Sramek, R., Schmidt, M., et al. 1989, AJ, 98, 1195

Khachikian, E. Y. & Weedman, D. W. 1974, ApJ, 192, 581

Kokotanekov, G., Wise, M., Heald, G. H., et al. 2017, A&A, 605, A48

Kopylova, F. G. & Kopylov, A. I. 2017, Astropysical Bulletin, 72, 363

Kormendy, J. & Gebhardt, K. 2001, 20th Texas Symp. Relativistic Astrophys., AIP Conf. Proc., Vol. 586 (AIP), 363

Kraft, R. P., Azcona, J., Forman, W. R., et al. 2006, ApJ, 639, 753

Lacy, M., Baum, S. A., Chandler, C. J., et al. 2020, PASP, 132, 035001

Lane, W. M., Cohen, A. S., Kassim, N. E., & Lazio, T. J. W. 2005, in Astronomical Society of the Pacific Conference Series, Vol. 345, From Clark Lake to the Long Wavelength Array: Bill Erickson's Radio Science, 203

Lanz, L., Jones, C., Forman, W. R., et al. 2010, ApJ, 721, 1702

Leccardi, A. & Molendi, S. 2008, A&A, 486, 359

Li, Y., Bryan, G. L., Ruszkowski, M., et al. 2015, ApJ, 811, 73

Limousin, M., Ebeling, H., Ma, C. J., et al. 2010, MNRAS, 405, 777

Łokas, E. L., Wojtak, R., Gottlöber, S., et al. 2006, MNRAS, 367, 1463

Mackay, C. D. 1969, MNRAS, 145, 31

Main, R. A., McNamara, B. R., Nulsen, P. E. J., et al. 2016, MNRAS, 464, 4360

Mantz, A., Allen, S. W., Ebeling, H., et al. 2010, MNRAS, 406, 1773

Mantz, A. B., Allen, S. W., & Morris, R. G. 2016, MNRAS, 462, 681

Markevitch, M., Sarazin, C. L., & Vikhlinin, A. 1999, ApJ, 521, 526

Markevitch, M. & Vikhlinin, A. 2007, Phys. Rep., 443, 1

Markevitch, M., Vikhlinin, A., & Forman, W. R. 2003, in Astronomical Society of the Pacific Conference Series, Vol. 301, Matter and Energy in Clusters of Galaxies, 37

Mason, A., Morrison, P., & Sadun, A. C. 1988, Nature, 333, 640

Mathews, W. G. & Guo, F. 2011, ApJ, 738, 155

Matteo, T. D., Springel, V., & Hernquist, L. 2005, Nat, 433, 7026

Mauch, T., Murphy, T., Buttery, H. J., et al. 2003, MNRAS, 342, 1117

Mazzotta, P., Edge, A. C., & Markevitch, M. 2003, ApJ, 596, 190

Mazzotta, P. & Giacintucci, S. 2008, ApJL, 675, L9

Mazzotta, P., Kaastra, J. S., & Paerels, F. B. 2002, ApJ, 567, L37

McDonald, M., Baybliss, M., Benson, B. A., et al. 2012, Nat, 488, 349

McDonald, M., Benson, B. A., Vikhlinin, A., et al. 2013, ApJ, 774, 23

McDonald, M., Benson, B. A., Vikhlinin, A., et al. 2014, ApJ, 794, 67

McDonald, M., Gaspari, M., McNamara, B. R., & Tremblay, G. R. 2018, ApJ, 858, 45

McDonald, M., McNamara, B. R., van Weeren, R. J., et al. 2015, ApJ, 811, 111

McDonald, M., McNamara, B. R., Voit, G. M., et al. 2019, ApJ, 885, 63

McMullin, J. P., Waters, B., Schiebel, D., Young, W., & Golap, G. 2007, in CASA Architecture and Applications, Vol. 376, 127

McNamara, B. R., Kazemzadeh, F., Rafferty, D. A., et al. 2009, ApJ, 698, 594

McNamara, B. R. & Nulsen, P. E. J. 2007, ARA&A, 45, 117

McNamara, B. R. & Nulsen, P. E. J. 2012, New J. Phys., 14, 055023

McNamara, B. R., Nulsen, P. E. J., Wise, M. W., et al. 2005, Nat, 433, 45

McNamara, B. R. & O'Connell, R. W. 1989, AJ, 98, 2018

McNamara, B. R., Wise, M., Nulsen, P. E. J., et al. 2000, ApJ, 534, L135

Meier, D. L., Sadun, A. C., & Lind, K. R. 1991, ApJ, 379, 141

Menci, N., Fontana, A., Giallongo, E., et al. 2006, ApJ, 647, 753

Merritt, D. & Farrarese, L. 2001, MNRAS, 320, L30

Mevius, M., van der Tol, S., Pandey, V. N., et al. 2016, Rad. Sci., 51, 927

Morabito, L., Jackson, N., Mooney, S., et al. 2022, A&A, 658, A1

Morrison, P. & Sadun, A. 1996, MNRAS, 278, 265

Nagai, D., Kravtsov, A. V., & Vikhlinin, A. 2007, ApJ, 668, 1

Netzer, H. 2015, ARAA, 53, 365

Nulsen, P. E. J., David, L. P., McNamara, B. R., et al. 2002, ApJ, 568, 163

O'Dea, C. P., Baum, S. A., Tremblay, G. R., et al. 2013, ApJ, 771, 38

Offringa, A. R., de Bruyn, A. G., Biehl, M., et al. 2010, MNRAS, 405, 155

Offringa, A. R., de Bruyn, A. G., Zaroubi, S., et al. 2013, A&A, 549, A11

Offringa, A. R., McKinley, B., Hurley-Walker, N., et al. 2014, MNRAS, 444, 606

Offringa, A. R. & Smirnov, O. 2017, MNRAS, 471, 301

Offringa, A. R., Wayth, R. B., Hurley-Walker, N., et al. 2015, PASA, 32, e008

O'Sullivan, E., Giacintucci, S., David, L. P., et al. 2011, ApJ, 735, 11

Overzier, R. A. 2016, A&ARv, 24, 14

Page, M. J., Symeonidis, M., Vieira, J. D., et al. 2012, Nat, 485, 213

Parker, E. A. & Kenderdine, S. 1967, The Observatory, 87, 124

Pascut, A. & Ponman, T. J. 2015, MNRAS, 447, 3723

Pasini, T., Gitti, M., Brighenti, F., et al. 2019, ApJ, 885, 111

Pasini, T., Gitti, M., Brighenti, F., et al. 2021, ApJ, 911, 66

Pedlar, A., Ghataure, H. S., Davies, R. D., et al. 1990, MNRAS, 246, 477

Peebles, P. J. E. & Yu, J. T. 1970, ApJ, 162, 815

Peng, E.-H., Andersson, K., Bautz, M. W., & Garmire, G. P. 2009, ApJ, 701, 1283

Perley, R. A. & Butler, B. J. 2013, ApJS, 204, 19

Perley, R. A. & Butler, B. J. 2017, ApJS, 230, 7

Peterson, J. R. & Fabian, A. C. 2006, Phys. Rep., 427, 1

Peterson, J. R., Kahn, S. M., Paerels, F. B. S., et al. 2003, ApJ, 590, 207

Pfrommer, C. & Enßlin, T. A. 2004, A&A, 413, 17

Pinzke, A. & Pfrommer, C. 2010, MNRAS, 409, 449

Pinzke, A., Pfrommer, C., & Bergström, L. 2011, Phys. Rev. D, 84, 123509

Planck Collaboration. 2020, A&A, 641, A6

Prasad, D., Sharma, P., & Babul, A. 2015, ApJ, 811, 108

Press, W. H. & Schechter, P. 1974, ApJ, 187, 425

Rafferty, D. A., Bîrzan, L., Nulsen, P. E. J., et al. 2013, MNRAS, 428, 58

Rafferty, D. A., McNamara, B. R., Nulsen, P. E. J., & Wise, M. W. 2006, ApJ, 652, 216

Raja, R., Rahaman, M., Datta, A., et al. 2020, ApJ, 889, 128

Rasia, E., Borgani, S., Murante, G., et al. 2015, ApJL, 813, L17

Reiprich, T. H. & Böhringer, H. 2002, ApJ, 567, 716

Richard-Laferrière, A., Hlavacek-Larrondo, J., Nemmen, R. S., et al. 2020, MNRAS, 499, 2934

Roger, R. S., Costain, C. H., & Bridle, A. H. 1973, AJ, 78, 1030

Romero, C., McWilliam, M., Macías-Pérez, J.-F., et al. 2018, A&A, 612, A39

Russell, H. R., McDonald, M., McNamara, B. R., et al. 2017, ApJ, 836, 130

Russell, H. R., McNamara, B. R., Edge, A. C., et al. 2013, MNRAS, 432, 530

Sadun, A. C. & Morrison, P. 2002, AJ, 123, 2312

Sanders, J. S., Fabian, A. C., & Taylor, G. B. 2009, MNRAS, 396, 1449

Santos, J. S., Rosati, P., Tozzi, P., et al. 2008, A&A, 483, 35

Santos, J. S., Rosati, P., Tozzi, P., et al. 2010, A&A, 521, A64

Savini, F., Bonafede, A., Brüggen, M., et al. 2018, MNRAS, 478, 2234

Savini, F., Bonafede, A., Brüggen, M., et al. 2019, A&A, 622, A24

Saxton, C. J., Bicknell, G. V., & Sutherland, R. S. 2002, ApJ, 579, 176

Scaife, A. M. M. & Heald, G. H. 2012, MNRAS, 423, L30

Schaye, J., Crain, R. A., Bower, R. G., et al. 2015, MNRAS, 446, 521

Scheuer, P. A. G. & Williams, P. J. S. 1968, ARA&A, 6, 321

Schlickeiser, R. 2002, Cosmic Ray Astrophysics (Springer)

Seth, R., O'Sullivan, E., Sebastian, B., et al. 2022, MNRAS, 513, 3273

Shimwell, T. W., Hardcastle, M. J., Tasse, C., et al. 2022, A&A, 659, A1

Shimwell, T. W., Röttgering, H. J. A., Best, P. N., et al. 2017, A&A, 598, A104

Shimwell, T. W., Tasse, C., Hardcastle, M. J., et al. 2019, A&A, 622, A1

Shulevski, A., Morganti, R., & Barthel, P. D. 2015, A&A, 583, A89

Sijacki, D., Springel, V., Matteo, T. D., & Hernquist, L. 2007, MNRAS, 380, 877

Simionescu, A., Allen, S. W., Mantz, A., et al. 2011, Science, 331, 1576

Soboleva, N. S., Temirova, A. V., Timofeeva, G. M., & Aliakberov, K. D. 1983, SvAL, 9, 305

Sotomayor-Beltran, C., Sobey, C., Hessels, J. W. T., et al. 2013, A&A, 552, A58

Sun, M., Voit, G. M., Donahue, M., et al. 2009, ApJ, 693, 1142

Sunyaev, R. A. & Zeldovich, Y. B. 1970, A&SS, 7, 3

Sweijen, F., Morabito, L. K., Harwood, J., et al. 2022, A&A, 658, A3

Takey, A., Schwope, A., & Lamer, G. 2011, A&A, 534, A120

Taylor, G. B., Barton, E. J., & Ge, J. 1994, AJ, 107, 1942

Timmerman, R., van Weeren, R. J., Botteon, A., et al. 2022a, A&A, 668, A65

Timmerman, R., van Weeren, R. J., Callingham, J. R., et al. 2022b, A&A, 658, A5

Timmerman, R., van Weeren, R. J., McDonald, M., et al. 2021, A&A, 646, A38

Ueda, S., Hayashida, K., Anabuki, N., et al. 2013, ApJ, 778, 33

Urry, M. C. & Padovani, P. 1995, PASP, 107, 803

Vagshette, N. D., Naik, S., Patil, M. K., & Sonkamble, S. S. 2017, MNRAS, 466, 2054

Vagshette, N. D., Naik, S. S. S. . S., & Patil, M. K. 2016, MNRAS, 461, 1885

van Breugel, W., Heckman, T., & Miley, G. 1984, ApJ, 276, 79

van Diepen, G., Dijkema, T. J., & Offringa, A. 2018, ASCL, ascl:1804.003

van Haarlem, M. P., Wise, M. W., Gunst, A. W., et al. 2013, A&A, 556, A2

Vantyghem, A. N., McNamara, B. R., & Russell, H. R. 2014, MNRAS, 442, 3192

van Weeren, R. J., de Gasperin, G., Akamatsu, H., et al. 2019, Space Sci. Rev., 215, 16

van Weeren, R. J., Intema, H. T., Lal, D. V., et al. 2014, ApJL, 786, L17

van Weeren, R. J., Shimwell, T. W., Botteon, A., et al. 2021, A&A, 651, A115

van Weeren, R. J., Williams, W. L., Hardcastle, M. J., et al. 2016, ApJS, 223, 2

Vogelsberger, M., Genel, S., Springel, V., et al. 2014, Nat, 509, 177

Voigt, L. M. & Fabian, A. C. 2004, MNRAS, 347, 1130

Voigt, L. M. & Fabian, A. C. 2006, MNRAS, 368, 518

Völk, H. J., Aharonian, F. A., & Breitschwerdt, D. 1996, Space Sci. Rev., 75, 297

Weisskopf, M. C., Tananbaum, H. D., Speybroeck, L. P. V., & O'Dell, S. L. 2000, in Society of Photo-Optical Instrumentation Engineers (SPIE) Conference Series, Vol. 4012, X-Ray Optics, Instruments, and Missions III, 2

Wen, Z. L. & Han, J. L. 2021, MNRAS, 500, 1003

Wen, Z. L. & Han, J. L. 2022, MNRAS, 513, 3946

Wen, Z. L., Han, J. L., & Yang, F. 2018, MNRAS, 475, 343

Werner, N., Zhuravleva, I., Canning, R. E. A., et al. 2016, MNRAS, 460, 2752

Williams, W. L., van Weeren, R. J., Röttgering, H. J. A., et al. 2016, MNRAS, 460, 2385

Williamson, R., Benson, B. A., High, F. W., et al. 2011, ApJ, 738, 139

Wise, M. W., McNamara, B. R., & Nulsen, P. E. J. 2007, ApJ, 659, 1153

Wu, L.-H., Wu, Q.-W., Feng, J.-C., et al. 2020, Res. Astron. Astrophys., 20, 122

Xie, C., van Weeren, R. J., Lovisari, L., et al. 2020, A&A, 636, A3

Xu, W., Readhead, A. C. S., Pearson, T. J., et al. 1995, ApJS, 99, 297

Yu, H., Tozzi, P., van Weeren, R. J., et al. 2018, ApJ, 853, 100

ZuHone, J. A., Brunetti, G., Giacintucci, S., & Markevitch, M. 2015, ApJ, 801, 146

ZuHone, J. A., Markevitch, M., & Brunetti, G. 2011a, Mem. Soc. Astron. Ital., 82, 632

ZuHone, J. A., Markevitch, M., Brunetti, G., & Giacintucci, S. 2013, ApJ, 762, 78

Zuhone, J. A., Markevitch, M., & Johnson, R. E. 2010, ApJ, 717, 908

ZuHone, J. A., Markevitch, M., & Lee, D. 2011b, ApJ, 743, 16

English summary

Those who stare at a clear night sky will be able to admire a few bright stars. The idea that stars are objects like the Sun, but then very far away, was suggested some two thousand years ago by the Greek philosopher Anaxagoras. However, it cost humanity a long time (and some their life) before this idea was generally accepted. This realization forms one of the first moments in which our horizon was broadened and we saw that the Universe was larger than our solar system. We were able to map the distribution of stars thanks to the development of telescopes. This taught us that our Sun is part of a larger collection of stars: the Milky Way. Only in 1918 did the work of Harlow Shapley using variable stars reveal the true scale of our Milky Way, as well as the position of our solar system within the Milky Way. Then, the next big question arose: is the Milky Way all there is in the Universe? In the Great Debate, Harlow argued that the spiral-shaped nebulae that had recently been observed were located at the edges of the Milky Way. Meanwhile, Heber Curtis saw these nebulae as independent galaxies. The conclusive proof was delivered by Edwin Hubble, who using variable stars was able to demonstrate that the distance to the Andromeda nebula was much larger than the scale of our Milky Way: approximately a million lightyears from the Earth. Suddenly it was clear that our Universe was much bigger than just the Milky Way.

A second fundamental discovery was that our Universe is not only much larger than previously thought, but also that it is dynamic. Edwin Hubble's most famous scientific result is the discovery of a correlation between the distance to a distant galaxy and the speed with which this object recedes from us. This confirmed the suspicion of the Belgian priest Georges Lemaître that the Universe could be expanding. This provided humanity with the first insight into the past of our Universe. If everything moves away from each other, then these objects would have been closer together in the past. Even more so, if you project all motions back in time, you will find that all galaxies come together at the same point in time: approximately 13.7 billion years ago. This is the foundation of the current cosmological model of the Big Bang.

Thanks to modern instruments, we can look even deeper into the Universe and carefully study the objects we see. Currently, the number of galaxies is estimated to be in the hundreds of billions. The limited speed of light is very valuable to research into the history of our Universe. In a vacuum, light travels a distance of 299,792,458 meters per second. This high, but limited, speed causes us to see everything at great distances with a significant time delay. Our Moon is just over a second away, the Sun at around 8 minutes, the planet Neptune is at

approximately 4 hours, and the Voyager 1 probe at the time of writing at almost a day. The nearest star (Proxima Centauri) is at a distance of over 4 lightyears and the diameter of our galaxy is approximately 100,000 lightyears. Thanks to the enormous distances in our Universe, we can see what the Universe looked like in the past by observing very distant objects. With modern telescopes, we can see and study galaxies billions of lightyears away, and therefore also look billions of lightyears into the past. With sub-millimeter observations we have even mapped the edge of our observable Universe: the afterglow of the Big Bang.

Thanks to deep observations and detailed simulations, we currently know that our Universe began as an extremely hot and dense medium. In the beginning, this medium was too hot for the formation of most particles we are made of. As the Universe expanded, the temperature also decreased, and the first protons, neutrons, electrons, nuclei, and atoms formed. After a long time, the temperature decreased enough for this matter to clump together through gravity. This led to the formation of the first stars, galaxies, and even galaxy clusters. These galaxy clusters are currently the most massive objects we find in our Universe. They do not only contain hundreds to thousands of galaxies but also a hot gas named the intracluster medium. As this gas cools down, it accretes onto the galaxies in the cluster and initiates the formation of new stars.

In addition to the formation of stars, the intracluster medium feeds something else: the supermassive black holes in the core of galaxies. In particular, in the central galaxies, we often find a black hole with a mass of a billion times the mass of our Sun. While devouring this gas from their environment, they release a large amount of energy. This happens in two different ways. First, the surrounding gas is generally heated so much that it produces intense radiation. Secondly, a part of this heated gas is channeled by magnetic fields into two jets which escape the gravitational pull of the black hole with almost the speed of light along the rotation axis of the black hole. This process causes a feedback cycle that reheats the intracluster medium and slows down the cooling of this gas.

To study this process, different types of observations are used. First of all, there are optical observations. These allow us to map distant galaxies and study both the existing stellar population and the formation of new stars. Because the atmosphere is largely transparent to optical light, many observations are performed from the ground. Although, for the best image quality, optical telescopes are commonly placed on top of high mountains, or even in space like the Hubble Space Telescope. In addition to optical observations, we also use X-ray observations. Because the intracluster medium has an extremely high temperature, it is primarily visible with X-ray observations. Because our atmosphere is not transparent for X-ray photons, we can only perform such observations using satellites like Chandra and XMM-Newton.

Finally, we commonly use radio observations such as those taken with the European LOw Frequency ARray (LOFAR) or the American Very Large Array. Contrary to optical and X-ray observations, where a single telescope can produce a detailed image, the radio observations used in this thesis were taken using interferometry. The angular resolution of a telescope is proportional to the ratio between the wavelength of the light that is being observed and the size of the

telescope. For radio wavelengths, which are very long, you would also need a very big telescope. Because this is technically near impossible, we employ a trick. By placing different radio antennas at a distance from each other, we can simulate a single telescope the size of the distance between these antennas. This makes it possible to build a virtual telescope with a size of a few thousand kilometers, which provides a high angular resolution.

Many questions remain about how the Universe as it is today came to be. How did galaxies form? What is the influence of the feedback process between black holes and the intracluster medium on the formation of new stars, and how did all of this work not just now, but also in the distant past? In this dissertation we study the feedback process in galaxy clusters, primarily using new high-resolution radio observations at low frequencies. With this, we intend to obtain a better view of what precisely happens near the black hole, how the intracluster medium is heated, and how this all relates to the formation of stars in the cluster.

In Chapter 2, we study the feedback process and the diffuse radio emission (also known as a "mini halo") in the Phoenix cluster using radio observations taken with the Very Large Array at frequencies between 1 and 12 GHz. Previous observations demonstrated that the intracluster medium in this cluster cools rapidly without being inhibited by the black hole at the center. We find that the mini halo was most likely formed due to turbulence in the intracluster medium after the merging of galaxy clusters in the past. In addition, we observe that the black hole undergoes varying periods of activity instead of being active at a constant level and that this black hole is likely underweight for a cluster of such a mass.

In Chapter 3, we focus on the famous radio source Hercules A. By combining Very Large Array observations with LOFAR observations, we can study the spectrum of this radio source over a much wider range than before. This offers insight into the electron population in the radio lobes of Hercules A. We find that the bright ring structures that were previously detected feature an increasingly steep spectrum as the distance to the central black hole increases. This measurement supports the hypothesis that these rings were not formed by shock waves but rather by inner lobes forming within the larger radio lobe. This also immediately provides insight into the time scale between outbursts of the central black hole.

In Chapter 4, we take LOFAR observations of a sample of 14 galaxy clusters. Using these observations, we test a method to measure the amount of energy being emitted by the environment of the black hole. This method requires that our low-frequency observations are sensitive enough to detect the complete radio lobes. By comparing the measured volume of the radio lobes with the volume of the imprint of these radio lobes in the intracluster medium, we can confirm that this method is indeed reliable.

In Chapter 5, we apply this method for the first time on a sample of distant galaxy clusters using LOFAR observations. Thanks to LOFAR's sensitivity and high angular resolution, we are able to measure the amount of energy injected by the black hole into its environment for the first time at such distances. This demonstrates that this method can also realistically be employed to measure the impact of the feedback process between the central black hole and the intracluster medium in the early Universe.

Nederlandse samenvatting

Wie 's nachts naar een heldere hemel staart zal een aantal heldere sterren kunnen bewonderen. Het idee dat sterren objecten zijn net als de Zon, maar dan heel ver weg, is zo'n ruime twee duizend jaar geleden al geopperd door de Griekse filosoof Anaxagoras. Het kostte de mensheid echter nog een lange tijd (en sommigen hun leven) voordat dit idee algemeen werd geaccepteerd. Deze realisatie vormt een van de eerste momenten waarop onze horizon werd verbreed en we inzagen dat het Universum groter was dan ons eigen zonnestelsel. Dankzij de ontwikkeling van telescopen kon de distributie van sterren voor het eerst in kaart worden gebracht. Dit leerde ons dat onze Zon deel is van een grotere collectie sterren: het Melkwegstelsel. Pas in 1918 gaf het werk van Harlow Shapley met variabele sterren voor het eerst een correct beeld van het formaat van ons Melkwegstelsel, evenals de positie van ons zonnestelsel in de Melkweg. Toen kwam echter de volgende grote vraag: is ons Melkwegstelsel het volledige Universum? In het Grote Debat stelde Harlow Shapley dat de spiraalvormige nevels die reeds waren waargenomen aan de randen van ons eigen Melkwegstelsel lagen, terwijl Heber Curtis deze nevels als andere Melkwegstelsels zag. Het doorslaggevende bewijs werd aangeleverd door Edwin Hubble, die aan de hand van variabele sterren in de Andromedanevel kon aantonen dat de afstand tot deze nevel veel groter was dan het formaat van ons Melkwegstelsel: zo'n miljoen lichtjaren vanaf de Aarde. Plotseling was duidelijk dat ons Universum veel groter is dan slechts de Melkweg.

Een tweede fundamentele ontdekking was dat ons Universum niet alleen veel groter is dan voorheen gedacht, maar dat deze ook dynamisch is. Edwin Hubble's meest beroemde wetenschappelijke resultaat is de vondst van een verband tussen de afstand naar een ver sterrenstelsel en de snelheid waarmee dit object van ons af beweegt. Dit bevestigde het vermoeden van de Belgische priester Georges Lemaître dat het Universum aan het uitdijen zou kunnen zijn. Hiermee had de mensheid een eerste inzicht gekregen in de geschiedenis van ons Universum. Als alles van elkaar af beweegt dan stonden al deze objecten dus vroeger dichter bij elkaar. Sterker nog, als je alle bewegingen terug in tijd projecteert vind je dat alle sterrenstelsels op hetzelfde moment in de geschiedenis bij elkaar komen: zo'n 13.7 miljard jaar in het verleden. Dit is het fundament voor het huidige cosmologische model van de Oerknal.

Dankzij moderne instrumenten kunnen we nog veel dieper in het Universum kijken en objecten die we zien veel nauwkeuriger bestuderen. Tegenwoordig wordt het aantal sterrenstelsels in de honderden miljarden geschat. Erg waardevol voor onderzoek naar de geschiedenis van ons Universum is de beperkte snelheid van

licht. In een vacuum legt licht een afstand af van 299.792.458 meter per seconde. Deze hoge, maar beperkte, snelheid zorgt ervoor dat we vrijwel alles op grote afstanden observeren met een significante tijdsvertraging. Onze Maan staat op een ruime seconde afstand, de Zon op zo'n 8 minuten, de planeet Neptunus op ongeveer 4 uur, en de Voyager 1 sonde op het moment van schrijven bijna een dag. De dichtstbijzijndste ster (Proxima Centauri) staat op een ruime 4 lichtjaren afstand en de diameter van onze Melkweg is ongeveer 100.000 lichtjaren. Dankzij de enorme afstanden in het Universum kunnen we dus door naar verre objecten te kijken zien hoe het Universum er in het verleden uitzag. Met moderne telescopen kunnen we sterrenstelsels zien en bestuderen op miljarden lichtjaren afstand, en dus ook een blik miljarden jaren terug in de tijd werpen. Met sub-millimeter observaties hebben we zelfs de grens van ons observeerbare Universum in kaart gebracht: de nagloed van de Oerknal.

Dankzij diepe observaties en gedetailleerde simulaties weten we momenteel dat ons Universum begon als een extreem heet en dicht medium. In het begin was dit medium nog te heet voor de formatie van de meeste deeltjes waar wij uit bestaan, maar naarmate het Universum uitdijde daalde ook de temperatuur en vormden de eerste protonen, neutronen, elektronen, nuclei en atomen. Na lange tijd daalde de temperatuur genoeg om deze materie te laten samenklonteren door de zwaartekracht. Hierdoor vormden de eerste sterren, sterrenstelsels en zelfs clusters van sterrenstelsels. Deze clusters van sterrenstelsels zijn tegenwoordig de zwaarste objecten die we in ons Universum vinden. Ze bevatten niet alleen honderden tot duizenden sterrenstelsels, maar ook een heet gas genaamd het intracluster medium. Naarmate dit hete gas afkoelt slaat het neer op de sterrenstensels in de cluster en initieert het de formatie van nieuwe sterren.

Naast de formatie van sterren voedt het intracluster medium nog iets: de superzware zwarte gaten in de kern van sterrenstelsels. Voornamelijk in de centrale sterrenstelsels vinden we vaak een zwart gat met een massa rond een miljard keer zwaarder dan onze Zon. Bij het opslokken van het gas uit hun omgeving komt veel energie vrij. Dit gebeurt op twee verschillende manieren. Ten eerste wordt het omringende gas vaak zoveel verhit dat het intense straling produceert. Ten tweede wordt een deel van dit verhitte gas door het magnetische veld in twee straalstromen gebundeld die langs de rotatie-as van het zwarte gat met bijna de snelheid van het licht ontsnappen aan de aantrekkingskracht van het zwarte gat. Dit proces zorgt voor een terugkoppelingsproces (ook wel "feedback" genoemd) die het intracluster medium weer verhit en dus de afkoeling van dit gas afremt.

Om dit proces in detail te bestuderen wordt gebruik gemaakt van verschillende soorten observaties. Allereest zijn er optische observaties. Hiermee kunnen we goed verre sterrenstelsels in kaart brengen en zowel de bestaande populatie sterren bestuderen als de formatie van nieuwe sterren detecteren. Omdat de atmosfeer grotendeels transparant is voor optisch licht worden ook veel observaties vanaf de grond gedaan. Echter, voor het beste beeld worden optische telescopen vaak wel boven op hoge bergen geplaatst, of zelfs alsnog in de ruimte, zoals de Hubble Ruimtetelescoop. Naast optische observaties worden ook röntgen observaties gebruikt. Omdat het intracluster medium een extreem hoge temperatuur heeft is het voornamelijk zichtbaar met röntgen observaties. Onze atmosfeer is niet

transparant voor röntgen fotonen, waardoor we alleen aan de hand van satellieten zoals Chandra en XMM-newton dit soort observaties kunnen nemen.

Ten slotte maken we veel gebruik van radio observaties zoals die van de Europese LOw Frequency ARray (LOFAR) of de Amerikaanse Very Large Array. In tegenstelling tot optische en röntgen observaties, waarbij een enkele telescoop een gedetailleerde afbeelding kan maken, zijn de radio observaties in dit proefschrift genomen met behulp van interferometrie. Het oplossend vermogen van een telescoop is namelijk proportioneel aan de verhouding tussen de golflengte van het licht dat wordt waargenomen en de grootte van de telescoop. Voor radio golflengtes, die heel lang zijn, heb je dus ook een heel grote telescoop nodig. Omdat dit vaak technisch vrijwel onmogelijk is wordt gebruik gemaakt van een truc. Door verschillende radio antennes op een afstand van elkaar te zetten kan een enkele telescoop gesimuleerd worden ter grootte van de afstand tussen de antennes. Hierdoor is het mogelijk om een virtuele telescoop te bouwen met een formaat van enkele duizenden kilometers, en dus ook een zeer goed oplossend vermogen te krijgen.

Er zijn nog veel open vragen over hoe het Universum zoals het er nu uit ziet tot stand is gekomen. Hoe vormden sterrenstelsels? Wat is de invloed van het terugkoppelingsproces tussen zwarte gaten en het intracluster medium op de formatie van nieuwe sterren, en hoe werkte dit alles niet alleen nu, maar ook in het verre verleden? In dit proefschrift onderzoeken we het terugkoppelingsproces in clusters van sterrenstelsels, met name door middel van nieuwe hoge-resolutie radio observaties op lage frequenties. Hiermee willen we een beter beeld krijgen van wat er precies gebeurt dicht bij het zwarte gat, hoe het intracluster medium wordt verhit en hoe dit alles invloed heeft op de sterrenstelsels in de cluster.

In Hoofdstuk 2 bestuderen we het terugkoppelingsproces en de diffuse radio emissie (ook wel “mini halo” genoemd) in de Phoenix cluster door middel van radio observaties genomen met de Very Large Array op frequenties tussen 1 en 12 GHz. Eerdere observaties hebben aangetoond dat het intracluster medium in deze cluster erg snel afkoelt zonder dat het wordt afgeremd door het zwarte gat in het centrum. Onze vinding is dat de mini halo waarschijnlijk ontstaan is door turbulentie in het intracluster medium als gevolg van een samensmelting van clusters in het verleden. Daarnaast observeren we dat het zwarte gat variërende periodes van activiteit heeft in plaats van dat deze constant actief is, en dat de massa van dit zwarte gat waarschijnlijk aan de lichte kant is voor de cluster.

In Hoofdstuk 3 focussen we ons op de bekende radio bron Hercules A. Door Very Large Array observaties te combineren met LOFAR observaties kunnen we het spectrum van deze radio bron bestuderen over een veel breder bereik dan voorheen. Dit biedt inzicht in de populatie aan elektronen in de radio lobben van Hercules A. We vinden dat de heldere ring structuren die eerder zijn gevonden een steeds stijler spectrum hebben naarmate de afstand tot het centrale zwarte gat toeneemt. Deze meting ondersteunt de hypothese dat deze ringen niet zijn gevormd door schokgolven maar door kleine lobben die ontstaan binnen de grote radio lob. Dit biedt ook onmiddelijk inzicht in de tijdsschaal tussen uitbarstingen van het centrale zwarte gat.

In Hoofdstuk 4 nemen we LOFAR observaties van een steekproef van 14 clusters. Aan de hand van deze observaties testen we een methode om de hoeveelheid

energie die wordt uitgestoten door de omgeving van het zwarte gat te meten. Deze methode vereist dat onze lage-frequentie observaties gevoelig genoeg zijn om de volledige radio lobben te detecteren. Door het gemeten volume van de radio lobben te vergelijken met het volume van de afdruk van de radio lobben in het intracluster medium bevestigen we dat deze methode inderdaad betrouwbaar is.

In Hoofdstuk 5 passen we deze methode voor het eerst toe op een aantal verre clusters van sterrenstelsels met behulp van LOFAR waarnemingen. Dankzij LOFAR's gevoeligheid en hoog oplossend vermogen zijn we voor het eerst in staat om op dergelijke afstanden met behulp van radio waarnemingen de hoeveelheid energie die door het zwarte gat in de omgeving wordt geïnjecteerd te bepalen. Hiermee tonen we aan dat deze methode ook realistisch gebruikt kan worden om in het vroege Universum te meten wat de impact is van terugkoppeling tussen het centrale zwarte gat en het intracluster medium.

Publications

First author

1. *The first high-redshift cavity power measurements of cool-core galaxy clusters with the International LOFAR Telescope*
   R. Timmerman, R. J. van Weeren, A. Botteon, H. J. A. Röttgering, L. K. Morabito and F. Sweijen
   Submitted to Astronomy & Astrophysics.

2. *Measuring cavity powers of active galactic nuclei in clusters using a hybrid X-ray-radio method*
   R. Timmerman, R. J. van Weeren, A. Botteon, H. J. A. Röttgering, B. R. McNamara, F. Sweijen, L. Bîrzan and L. K. Morabito
   Astronomy & Astrophysics, 2022, 668, A65

3. *Origin of the ring structures in Hercules A*
   R. Timmerman, R. J. van Weeren, J. R. Callingham, W. D. Cotton, R. Perley, L. K. Morabito, N. A. B. Gizani, A. H. Bridle, C. P. O'Dea, S. A. Baum, G. R. Tremblay, P. Kharb, N. E. Kassim, H. J. A. Röttgering, A. Botteon, F. Sweijen, C. Tasse, M. Brüggen, J. Moldon, T. Shimwell and G. Brunetti
   Astronomy & Astrophysics, 2022, 658, A5

4. *Very Large Array observations of the mini-halo and AGN feedback in the Phoenix cluster*
   R. Timmerman, R. J. van Weeren, M. McDonald, A. Ignesti, B. R. McNamara, J. Hlavacek-Larrondo and H. J. A. Röttgering
   Astronomy & Astrophysics, 2021, 646, A38

Contributing author

1. *A novel radio imaging method for physical spectral index modelling*
   E. Ceccotti, A. R. Offringa, L. V. E. Koopmans, **R. Timmerman**, S. A. Brackenhoff, B. K. Gehlot, F. G. Mertens, S. Munshi, V. N. Pandey, R. J. van Weeren, S. Yatawatta and S. Zaroubi
   Monthly Notices of the Royal Astronomical Society, 2023, 525, 3, 3946

2. *A 'MeerKAT-meets-LOFAR' study of Abell 1413: a moderately disturbed non-cool-core cluster hosting a ∼500 kpc 'mini'-halo*

C. J. Riseley, N. Biava, G. Lusetti, A. Bonafede, E. Bonnassieux, A. Botteon, F. Loi, G. Brunetti, R. Cassano, E. Osinga, K. Rajpurohit, H. J. A. Röttgering, T. Shimwell, **R. Timmerman**, R. J. van Weeren
Monthly Notices of the Royal Astronomical Society, 2023, 524, 4, 6052

3. *VLBI imaging of high-redshift galaxies and protoclusters at low radio frequencies with the International LOFAR Telescope*
C. M. Cordun, **R. Timmerman**, G. K. Miley, R. J. van Weeren, F. Sweijen, L. K. Morabito and H. J. A. Röttgering
Astronomy & Astrophysics, 2023, 676, A29

4. *V-LoTSS: The circularly polarised LOFAR Two-metre Sky Survey*
J. R. Callingham, T. W. Shimwell, H. K. Vedantham, C. G. Bassa, S. P. O'Sullivan, T. W. H. Yiu, S. Bloot, P. N. Best, M. J. Hardcastle, M. Haverkorn, R. D. Kavanagh, L. Lamy, B. J. S. Pope, H. J. A. Röttgering, D. J. Schwarz, C. Tasse, R. J. van Weeren, G. J. White, P. Zarka, D. J. Bomans, A. Bonafede, M. Bonato, A. Botteon, M. Brüggen, K. T. Chyży, A. Drabent, K. L. Emig, A. J. Gloudemans, G. Gürkan, M. Hajduk, D. N. Hoang, M. Hoeft, M. Iacobelli, M. Kadler, M. Kunert-Bajraszewska, B. Mingo, L. K. Morabito, D. G. Nair, M. Pérez-Torres, T. P. Ray, C. J. Riseley, A. Rowlinson, S. Shulevski, F. Sweijen, **R. Timmerman**, M. Vaccari and J. Zheng
Astronomy & Astrophysics, 2023, 670, A124

5. *The LOFAR Two-metre Sky Survey – V. Second data release*
T. W. Shimwell, M. J. Hardcastle, C. Tasse, P. N. Best, H. J. A. Röttgering, W. L. Williams, A. Botteon, A. Drabent, A. Mechev, A. Shulevski, R. J. van Weeren, L. Bester, M. Brüggen, G. Brunetti, J. R. Callingham, K. T. Chyży, J. E. Conway, T. J. Dijkema, K. Duncan, F. de Gasperin, C. L. Hale, M. Haverkorn, B. Hugo, N. Jackson, M. Mevius, G. K. Miley, L. K. Morabito, R. Morganti, A. Offringa, J. B. R. Oonk, D. Rafferty, J. Sabater, D. J. B. Smith, D. J. Schwarz, O. Smirnov, S. P. O'Sullivan, H. Vedantham, G. J. White, J. G. Albert, L. Alegre, B. Asabere, D. J. Bacon, A. Bonafede, E. Bonnassieux, M. Brienza, M. Bilicki, M. Bonato, G. Calistro Rivera, R. Cassano, R. Cochrane, J. H. Croston, V. Cuciti, D. Dallacasa, A. Danezi, R. J. Dettmar, G. Di Gennaro, H. W. Edler, T. A. Enßlin, K. L. Emig, T. M. O. Franzen, C. García-Vergara, Y. G. Grange, G. Gürkan, M. Hajduk, G. Heald, V. Heesen, D. N. Hoang, M. Hoeft, C. Horellou, M. Iacobelli, M. Jamrozy, V. Jelić, R. Kondapally, P. Kukreti, M. Kunert-Bajraszewska, M. Magliocchetti, V. Mahatma, K. Małek, S. Mandal, F. Massaro, Z. Meyer-Zhao, B. Mingo, R. I. J. Mostert, D. G. Nair, S. J. Nakoneczny, B. Nikiel-Wroczyński, E. Orrú, U. Pajdosz-Śmierciak, T. Pasini, I. Prandoni, H. E. van Piggelen, K. Rajpurohit, E. Retana-Montenegro, C. J. Riseley, A. Rowlinson, A. Saxena, C. Schrijvers, F. Sweijen, T. M. Siewert, **R. Timmerman**, M. Vaccari, J. Vink, J. L. West, A. Wołowska, X. Zhang and J. Zheng
Astronomy & Astrophysics, 2022, 659, A1

6. *LoTSS Jellyfish Galaxies III. The first identification of jellyfish galaxies in the Perseus cluster*

I. D. Roberts, R. J. van Weeren, **R. Timmerman**, A. Botteon, M. Gendron-Marsolais, A. Ignesti and H. J. A. Röttgering
Astronomy & Astrophysics, 2022, 658, A44

7. *A MeerKAT-meets-LOFAR Study of MS 1455.0+2232: A 590 kiloparsec 'Mini'-Halo in a Sloshing Cool-Core Cluster*
C. J. Riseley, K. Rajpurohit, F. Loi, A. Botteon, **R. Timmerman**, N. Biava, A. Bonafede, E. Bonnassieux, G. Brunetti, T. Enßlin, G. Di Gennaro, A. Ignesti, T. Shimwell, C. Stuardi, T. Vernstrom and R. J. van Weeren
Monthly Notices of the Royal Astronomical Society, 2022, 512, 3, 4210

Curriculum Vitae

I was born on August 6, 1996, in the city of Meppel in the Netherlands. Despite initial efforts from my father during my toddlerhood to guide me into a career as a carpenter, like most of my family, it quickly became clear that my career prospects lay elsewhere. However, I did not see myself pursuing a career in science during the majority of my childhood, even though science was something I had a keen interest in. During my childhood, one of my main interests was in computers, which I could imagine myself doing as a career whenever I failed to avoid thinking about my future. At the age of 12, I started my VWO at the Greydanus College in Meppel and later Zwolle. During this time, I thoroughly enjoyed following physics, chemistry, mathematics and computer science classes. I made friends with a few amazing people, whom I am still in contact with to this day, and found it incredibly helpful to have friends who were as passionate as I was in these topics. When the time came at the end of my VWO to find a university programme, I initially looked into going to Utrecht to pursue either computer science or game development together with a friend. However, I was also attracted to the physics and astronomy programme in Utrecht, and attended a few information days. To my disappointment, I discovered that the astronomy component was practically non-existent, which made me realize for the first time that I actually would be very interested in pursuing astronomy. Ironically, it was this lack of astronomy in Utrecht which revitalized the interest in astronomy I have had since I was a child. I subsequently attended a few information days at the Kapteyn Astronomical Institute in Groningen and was immediately hooked. I finished my VWO and enthusiastically moved to Groningen to join the BSc Sterrenkunde programme.

During my bachelor's, I passionately followed physics, mathematics and astronomy courses. Again, I made new friends who were equally invested in learning about the nature of our Universe, and together we attended classes, made homework and prepared for exams. I still consider these friends to be my best friends, and will always appreciate the support they've given me during my bachelor's. In my third year, I followed the radio astronomy course by Dr. John McKean, and fell in love with this area of astronomy. After having successfully broken my cum laude streak with a 6 for the radio astronomy exam, I approached John for a BSc project. John offered me an exciting project on a distant lensed quasar, which required me to process 80 hours of 22 GHz Very Large Array data divided over 42 separate observations. To give me the best training possible, he told me to download the data from the archive without the flags applied by the observatory, so I would have to manually go through the observations to spot erroneous data.

Thanks to extra help from Cristiana Spingola and Hannah Stacey, I reduced and imaged all 80 hours of data, and my love for radio interferometry was awakened. I also first tasted what it was like to do research, and also fell in love with this practical aspect of science. I remember being disappointed to discover it was Friday afternoon, meaning I had to wait till Monday before I got to work on my project again. Unlike during courses, when all the information was presented to you during organized lectures, research requires that you fight for knowledge and insight using your curiosity, persistence and attention to detail. It felt amazing to be curious again on a daily basis and look into the Universe to discover its secrets. After my BSc project, I continued with a master's programme at the Kapteyn Astronomical Institute in Groningen and did not hesitate to approach John again for a project. This time, we would be working on a distant lensed quasar using High Sensitivity Array (HSA) observations, which include the VLBA, VLA, Effelsberg, Arecibo and the Greenbank Telescope (GBT). Unfortunately, Arecibo was offline due to hurricane damage, robbing me of my only opportunity to work with this telescope before old age took it from us. Additionally, the Effelsberg data was lost and the VLA was phased up in A-configuration instead of D-configuration, making it rather useless for HSA purposes. Fortunately, I was still able to obtain my first VLBI experience, reducing and imaging the VLBA and GBT observations in AIPS. Again, I loved every moment of this observational radio astronomy project, which reinforced my desire to pursue a PhD in this direction.

After obtaining my MSc degree cum laude in 2019, I was fortunate enough to be able to continue my academic career with my #1 choice: the LOFAR-VLBI project on radio-mode feedback in clusters at Leiden Observatory under the supervision of Reinout van Weeren. The following four years became some of the best years of my life. I've been able to enjoy the company of some amazing people in the LOFAR group, the observatory and on my trips abroad. I've been able to visit the USA during the 7th VLA Data Reduction School. I attended the LOFAR KSP Meeting in Turin at the end of 2019 before COVID shut everything down, and I've more than compensated for the following lockdown with an observation trip to La Palma to assist with observations for Ian Roberts, LOFAR Family meetings in Cologne and Olsztyn, the IAU General Assembly in South Korea, the SPARCS meeting in South Africa, the VLBI anniversary in Bologna for an invited talk, and LOFAR Long Baseline Busy Weeks in Durham and Paris. During my PhD, I have gained extensive experience with the calibration of LOFAR-VLBI observations, and look forward towards a bright future of radio astronomy where we can make these observations more accessible to the general community. Additionally, the SKA and ngVLA are approaching rapidly, offering a lot to be excited for.

Following my PhD, I will proceed with a postdoc at Durham University in the United Kingdom, where I will be working with Dr. Leah Morabito. In Durham, I will continue in the same research direction, studying radio-mode feedback in galaxy clusters with LOFAR-VLBI observations, but then shifting my focus more towards the high-redshift regime where I started my academic career.

Acknowledgements

When I started my PhD in Leiden, I could not have imagined what a beautiful time was ahead of me. Even despite the COVID-19 pandemic, I have enjoyed some of the most amazing years I could have asked for. I am extremely grateful to all my friends, colleagues, and everyone else for this unforgettable experience.

I want to start with my supervisor, Reinout. You told me one should never thank their supervisor because they are simply doing the job they're supposed to do, but you did so much more than that. Not only were you the most knowledgeable, helpful, patient, and supportive supervisor, but you are also one of the nicest, humblest, and friendliest people I know. You will always be a role model to me and so many others. You have guided me smoothly through my PhD, helped me develop myself into an independent researcher and prepared me for the next exciting steps in my career.

Huub, you have been a great second supervisor for me. You have always been supportive, while also never failing to seize an opportunity to challenge my research. You have made me a better researcher, and I will frequently ask myself "what would Huub say?" in my future career. I have really enjoyed working with you.

To my friends of the LOFAR group, I cannot thank you enough. You have made the Leiden Observatory feel like home from the first day. We have traveled the world together and made memories I will cherish for the rest of my life. Erik and Anniek, you were like a brother and sister to me these past four years, and I have counted myself incredibly lucky many times that our paths crossed. I hope we will remain friends for a long time. Frits, my mentor, thank you for helping me understand even the most subtle details of low-frequency radio interferometry with LOFAR. Maria, thank you for your endless enthusiasm and for getting me involved in fascinating new projects. Jurjen, thank you for all the amazing help and for all the dances. Christian, thank you for dealing with the lowest frequencies so the rest of us don't have to. Joe, thank you for always being supportive and for all your wisdom. Andrea, thank you for all the help with the X-ray observations. Gabriella, thank you for taking the time to talk to me during my interviews and convincing me I should do a PhD with Reinout. I'm still planning to visit Hamburg one day... Finally, of course also a warm thank you to Sarah, Tim, Wendy, George, Martijn, Rafaël, Ian, HaoYang, Jit, Tong, Sai, Joshua, Xuechen, Raymond, and Kim.

To my collaborators of the LOFAR Surveys team, thank you for being such amazing colleagues. It has been a delight to work with you and learn from you. A

special thank you goes to the Long Baseline Working Group: Leah, Neal, Shruti, Emmanuel, Marco, Etienne, Alexander, Emmy, Gulay, Marcin, Martin, Pranav, Vijay, Shane, James, Jonny, Hrishikesh, Cyril, Matthijs, Deepika and Alexandra. Naturally, I am also very grateful to all the other members of the collaboration for all the support, amazing discussions, and experiences at our many scientific meetings: Alessandro, Annalisa, Aurora, Bernard, Bohan, Carole, Catherine, Corey, Dan, David, Duy, Francesco, Gianfranco, Giulia, Harish, Hiroki, Javier, Ken, Lara, Laura, Luca, Marco, Marco, Marco, Marcus, Marina, Marisa, Matthias, Nadia, Nika, Philip, Rohit, Thomas, Tiziana, Tom, and Volker.

To my dear friends of the Leiden Observatory, thank you for being such lovely people! You are a big part of the reason why I've enjoyed the past four years as much as I did. First of all, thank you to my office mates: Andrej, Kirsty, Marta, Josh, Mathilde, Leindert and Matus. You have always been amazing company. Also a big thank you to the Gnarrllllyy committee for organizing the unforgettable PhSki trip: Juicing Joey "the Iceman" Braspenning, Roi "the Shredder" Kugel, Cool Chris "the PUNisher" van Buchem and Aperol Spritz Amy (first of her name) "loco loca" Louca. I could not have wished for a better first winter sports experience! Next, a very warm thanks for all the other lovely people who were always welcoming and helped make the observatory the warm place it is, including but not limited to Alessia, Andrew, Anna, Bas, Brigitte, Chloe, Ciaran, Dario, Dilovan, Dora, Elia, Elina, Evgenii, Fedde, Folkert, Fraser, Gijs, Helgi, Hiddo, Ivana, Jeger, Jelle, Jeroen, Lammim, Lucie, Lukasz, Luna, Lýdia, Maaike, Maite, Mantas, Margot, Marina, Markus, Martijn, Martje, Morgan, Natasha, Niccolò, Olivier, Orestis, Osmar, Patrick, Paul, Piyush, Pooneh, Rico, Rob, Roi, Ruslan, Samira, Sanjana, Shun-Sheng, Sid, Sill, Silvia, Stella, Stijn, Thijs, Thomas, Timo, Turgay, Verónica, Victorine, Willeke, William, Xiaoyuan, Yanling, Yapeng, Zephyr, Zhenlin and Zorry. Naturally, a special thank you also goes to the support staff of the observatory, who have always been friendly and helpful: Alexandra, Alina, Bram, Châtelaine, David, Eric, Erik, Evelijn, Hafize, Huib, Jacqueline, Liesbeth, Marjan, Monica, Nancy, Nuray, Robin, Somayeh, and Susanne. Finally, I want to thank the left coffee machine in the Kaiser Lounge, you always made the best (free) coffee. Finally finally, I want to thank the Big Dipper for blessing us with wonderful borrels.

To all the lovely people I met during my trips, thank you for making these trips some of my best memories! I hope I'll have the chance to meet many of you again. Thanks for making my trip to Socorro an absolute blast, Andrew, Annaliese, Anton, Cosima, Francesca, Gerrit, Kenzie, Tatiana, and Virginia. Thanks for joining me on my trip to Bologna and for being such lovely company that week, Célestin, Florian, Florian, and Jonas. Thanks for joining the Leiden gang on our trip to South Africa, Jonah and Shilpa. You made it an even better experience than I could have ever dreamed of.

To all my friends outside of my world of academia, thank you for being my support and providing me with a lot of "life" for my work-life balance. I first want to thank my dear friends, the Step Musketeers: Kevin and Reinier. I am super happy we stayed in touch so often despite going our separate ways in life after our master's in Groningen. You have been an incredible support. Next, I want

to thank the rest of the Kangoeroes: Hans, Gijsbert, Suzan, Marcel, and Daniël. You are the best Walibi-gang anyone could ask for. A special thank you goes to my medeowner: Bas. I have always admired your positive influence on everyone around you. Never stop being you. Naturally, I also want to thank the members of the Grote Oef: Bart, Bram, Calvin, Gerben, Hans, Lars, Maarten, Michael, and Timon. Who knows how I would have made it through the pandemic without you all. Also a big thank you to Bradley, Leander, Lisa, Martijn, and Richard for all the good times we've shared together. Almost finally, a special thank you to three lovely people who have made Leiden always a warm place for me: Tom, Tjissa, and Josefine. Finally, a big thank you to Rick for the incredible cover illustration.

The last thank yous go to two very special people to me: my parents. You have always supported me, from my first day till now. You have always been a loving home to me, and you mean the world to me. I would not have been here in life without your infinite support.